DOUBLE-SLIT PHOTOMETRIC MEASUREMENT
OF
VELOCITY PROFILES FOR BLOOD
IN
MICROVESSELS AND CAPILLARY TUBES

Thesis by

Mary Baker

In Partial Fulfillment of the Requirements
for the Degree of
Doctor of Philosophy

California Institute of Technology
Pasadena, California

1972

(Submitted March 27, 1972)

ACKNOWLEDGMENTS

Dr. J. H. Wayland provided guidance at every stage of my graduate work. He has been a very helpful source of information and ideas on courses, relevant literature, experimental techniques and equipment. I would like to thank him for his patience and consideration through numerous experimental difficulties.

Drs. G. R. Cokelet, H. J. Meiselman and F. M. M. Morel provided many valuable discussions and suggestions for which I am very grateful. Discussions with Dr. Morel, in particular, greatly facilitated the preparation of the thesis.

Mr. M. Dale Elmore contributed valuable assistance in every stage of the processing of electrical signals. Mr. Paul Knust-Graichen's talents provided the solution to countless experimental bottlenecks. I continue to be amazed at the high level of competence and very willing attitude of both Paul and Dale.

The United States Public Health Service provided financial support for this investigation through research grant HE 08977 and training grant T01 ES00004.

ABSTRACT

The extreme blunting of velocity profiles for human blood, reported from double-slit photometric measurements, has been shown to be an artifact of the measuring technique. The velocities measured are actually an average of velocities throughout the tube. An equation developed to model this averaging predicts profiles which agree with experimental results. This model explains the increase in blunting with decreasing tube diameter previously reported even if the true profiles remain parabolic.

A trial and error method was chosen to extract information about the actual velocity distributions from double-slit measurements. Trial profiles were calculated using a τ versus $\dot{\gamma}$ relationship derived from bulk rheological measurements. The data of Barbee for τ_w versus $\overline{U}$ and for tube relative hematocrit were used. When these trial profiles were averaged with the model for double-slit averaging, they were consistent with double-slit measurements. Neither the calculated nor measured profiles gave any evidence of substantial blunting except for $\overline{U} < 2 \text{ sec}^{-1}$ where yield stress becomes important.

Although the continuum approach was used to calculate trial profiles, limitations in the continuum representation were evident from hematocrit considerations. No hematocrit distribution could be found that resulted in calculated profiles which produced both the correct volume flow rate and correct outflow hematocrit.

A simple correction procedure is described for calculating volume flow rates from double-slit centerline velocity measurements.

TABLE OF CONTENTS

LIST OF SYMBOLS

D	Tube diameter
E	Exponent for hematocrit distribution, Equation 15
H	Hematocrit (volume fraction of red cells)
H_d	Hematocrit of blood discharged from tube
H_f	Hematocrit of blood in feed reservoir
H_r	Tube relative hematocrit, H_t/H_f
H_t	Hematocrit of blood inside capillary tube
H^*	Centerline hematocrit
L	Length of a tube
ΔP	Pressure drop
$\dot{Q}$	Volume flow rate
$\dot{Q}_m$	Volume flow rate determined from integration of a measured velocity profile
$\dot{Q}_p$	Known volume flow rate produced by the syringe pump
R	Tube radius
RBC	Red blood cells
$\overline{U}$	Reduced average velocity, $\overline{V}/D$
$\overline{V}$	Average velocity in tube, $\dot{Q}_p/\pi R^2$
V_{cl}	Centerline velocity
V_{max}	Maximum velocity for parabolic flow
$v_{ave}(x)$	Double-slit averaged velocity
$v(r)$	Velocity in direction of tube axis as a function of radius
w	Width over which velocities are averaged

x	Distance of photosensor from tube axis
$\dot{\gamma}$	Shear rate
$\dot{\gamma}_w$	Shear rate at tube wall
δ	Plasma layer thickness
μ	Newtonian viscosity coefficient
μ_p	Plasma viscosity
μm	Micron
τ	Shear stress
τ_w	Shear stress at tube wall
τ_y	Yield stress

LIST OF FIGURES

I. INTRODUCTION

Much of the attention of circulatory physiologists is directed toward observation and monitoring of beds of microscopic blood vessels. The functioning of an entire organ can sometimes be revealed by such observations. It is in these microvessels that the primary function of the circulatory system takes place. This is where the nutrients are delivered to the tissue cells and their waste products are removed. In order to study these exchange processes it is often necessary to measure flow rates and velocity distributions. The radial distributions of velocities in tube flow are also of interest in the study of the rheological properties of blood. This thesis deals with the development, use and results of one method of making velocity measurements on the magnified and projected image of blood flowing in capillary tubes or microvessels.

II. BACKGROUND INFORMATION

Discussions of the biological and chemical properties of blood are presented in the references(8, 16, 57). The rheological properties are discussed in references(12, 20, 42, 54, 57). Only a short summary of those facts about blood and the microcirculation that are particularly relevant to this thesis is presented here.

Microcirculation

A microcirculatory bed may contain vessels varying in diameter from 500 μm of the first arteriole or venule branching from an artery or vein down to the 5-15 μm of the capillaries. The organization of these vessels varies greatly with the particular tissue of which it is a part. The blood velocities range from zero up to 5mm/sec for a venule, 10mm/sec for an arteriole and 1mm/sec for a capillary. Typical Reynolds numbers, with respect to tube diameter, may range from .1 to .007. The flow of blood through these vessels is regulated to meet the varying needs of the tissue and at the same time maintain the efficiency of the circulatory system as a whole. As a bed of vessels is observed, the pattern of flow constantly changes. At one moment blood flows through one part and a few minutes later that part is shut off and the blood flows through another part. In some capillaries flow even reverses. The observation and understanding of these patterns and modes of regulation are the objectives of the type of studies which make use of the velocity measurement method of this thesis.

A sample microcirculatory bed is shown in Figure 1. This photograph shows the organization of a group of microvessels in a section of cat mesentery. The diagram in Figure 2 describes the vessels shown in the photograph.

Blood

The blood passing through these microcirculatory beds consists of red cells, white cells and platelets suspended in a clear, straw colored liquid called plasma. The red cells are by far the most abundant particle. The volume percentage of red cells is referred to as hematocrit and is normally 42% for females and 47% for males. Under disease conditions the hematocrit may be as low as 10%, or as high as 75%. Other particles in blood represent less than 1% of blood volume.

Red cells in an unstressed state, shown in Figure 3, maintain the shape of a biconcave disc with maximum diameter of about 8 μm and thickness of about 2 μm. They are thus larger than many of the microvessels but, because of their extreme flexibility, they pass through these tiny vessels with ease. Their behavior appears similar to that of a fluid-filled sack. The interior of the cells is filled with a hemoglobin solution which is responsible for transporting oxygen. When placed in a solution of sufficiently lower salt concentration than that of plasma, the cells will swell and eventually break, spilling their contents and leaving only the membrane. This process of losing the hemoglobin is called hemolysis. The empty membrane, under carefully controlled conditions, can regain its biconcave shape and is then referred

Figure 1 Mesenteric Microvessels of a Cat

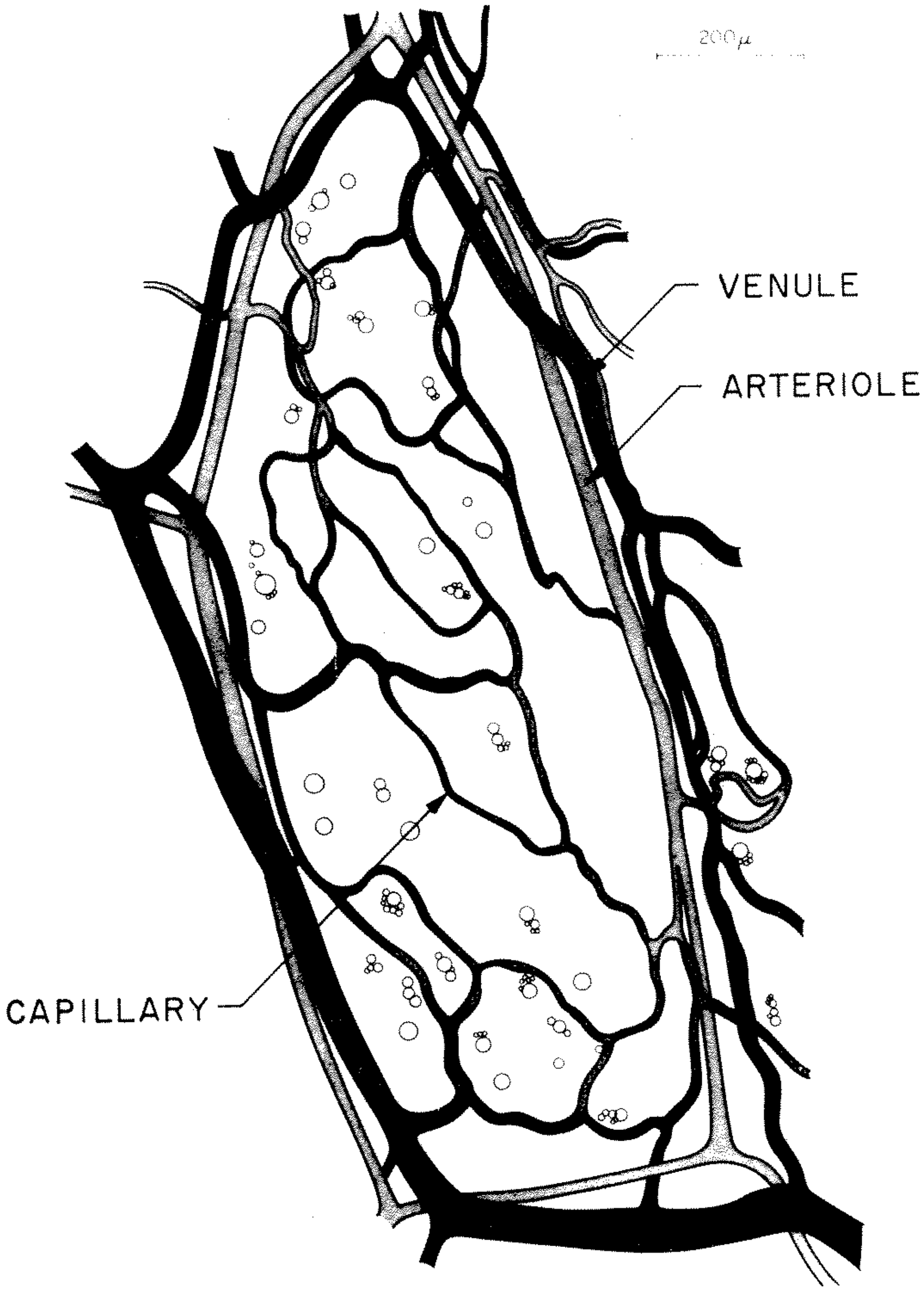

Figure 2 Diagram Describing Figure 1.

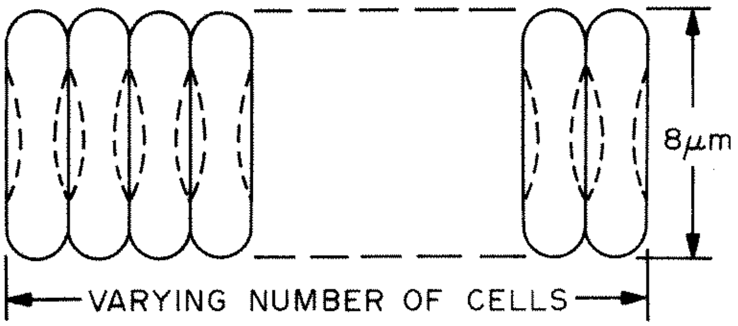

RED CELL AGGREGATE (ROULEAUX)

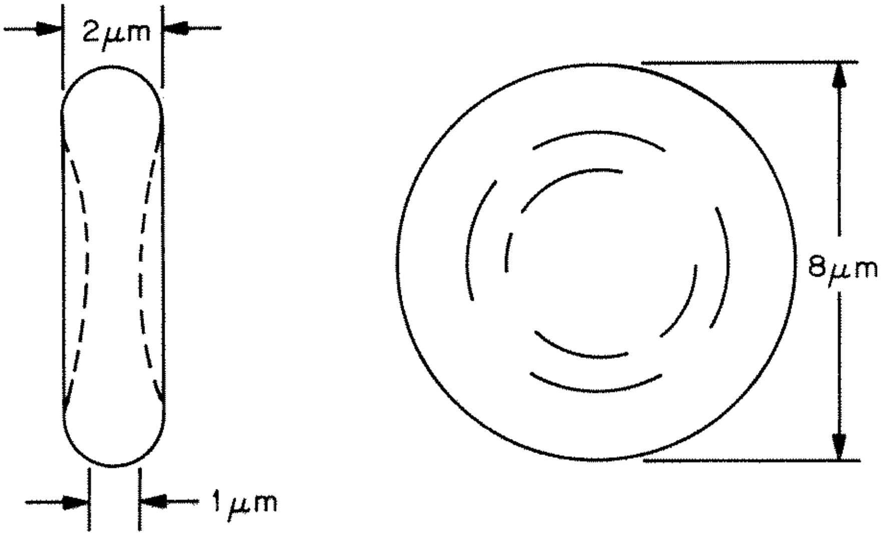

THE HUMAN RED CELL

Figure 3

to as a red cell ghost. The specific gravity of red cells is slightly higher than that of plasma. This allows the cells to be easily separated from the plasma by centrifugation; however, it makes stirring necessary to maintain uniform concentration in a reservoir of blood.

The concentration and distribution of white cells can vary widely and rapidly even in healthy persons. They are so flexible that they can squeeze in and out through the vessel walls. Their life span can be as short as 4 hours. Because of these complications and because white cells and platelets have concentrations very low compared to the red cells, they are usually removed in making rheological measurements on blood. Suspensions of red cells in plasma have been shown to be rheologically similar to whole blood.

Plasma is an aqueous solution of salts, urea, sugar, cholesterol, and proteins with a pH of 7.46 and an osmolarity of about 300 mosm. Rheologically, the important component of plasma is fibrinogen, a protein molecule about 500Å in length, with two spherical ends and a spherical center each about 65Å in diameter.

Normally, coagulation of blood occurs within several minutes after it is removed from the body. The red cells become irreversibly clumped together in an irregular pattern. In order to use the blood for rheological measurements, it is necessary to prevent this process. The naturally occurring anticoagulant, heparin, or a standard ACD solution (citric acid, dextrose, sodium citrate) is added for this purpose. Only a few measurements of rheological properties of blood have been accomplished without the use of anticoagulants (Frasher, Wayland and

Meiselman(25) and Meiselman(40)). These investigations found no effects of the anticoagulants on the rheological properties of blood; however, because of the limited range of shear rates used, they did not completely eliminate the possibility of an effect.

A separate occurrence of red cell aggregation is the reversible orderly process of rouleaux formation. As soon as blood is stationary or flowing at a slow enough rate, the red cells aggregate with flat faces together into orderly stacks called rouleaux shown in Figure 3. As soon as the flow rate is increased the aggregates break up again into individual cells. Rouleaux formation occurs in normal healthy blood and has a definite effect on its rheological properties.

Rheological Properties of Blood

Blood is a shear-thinning fluid which exhibits a yield stress. This behavior is thought to be due to the deformability of the suspended cells and to the cellular aggregation which occurs at low flow rate but disappears as flow rate increases. If the plasma protein fibrinogen is removed, or if the red cells are suspended in saline, the aggregates do not form and the suspension does not exhibit a yield stress; however, red cells in saline still show shear-thinning behavior. Plasma alone is a Newtonian fluid within the limits of accuracy of present rheological instruments. No normal stress differences or history dependent flow properties have been observed for blood, red cell suspensions, or plasma.

Using a Couette viscometer, Cokelet(16, 18) has shown that a rheological model developed by Casson(14) correlates shear stress versus rate of strain data in the low shear rate range near 1 sec^{-1} and below. The Casson equation is the following:

$$\tau^{1/2} = s\dot{\gamma}^{1/2} + \tau_y^{1/2} \tag{1}$$

τ = shear stress

τ_y = yield stress

$\dot{\gamma}$ = shear rate of strain

s = constant.

This equation predicts a straight line of slope s and intercept $\tau_y^{1/2}$ for a plot of $\tau^{1/2}$ versus $\dot{\gamma}^{1/2}$. A square root plot of Cokelet's data is shown in Figure 4; the variation of s with hematocrit is also shown. The value of yield stress has been confirmed in a capillary viscometer (Benis(5)). This value varies greatly between different blood samples but for a given sample varies as the cube of the hematocrit above some critical hematocrit. This relationship is given by the following expression:

$$\tau_y = a(H-H_c)^3 \tag{2}$$

a = constant for a given sample of blood

H = hematocrit

H_c = critical hematocrit below which $\tau_y = 0$.

The variability of yield stress between different blood samples is demonstrated by Cokelet in the plot of his data in Figure 5.

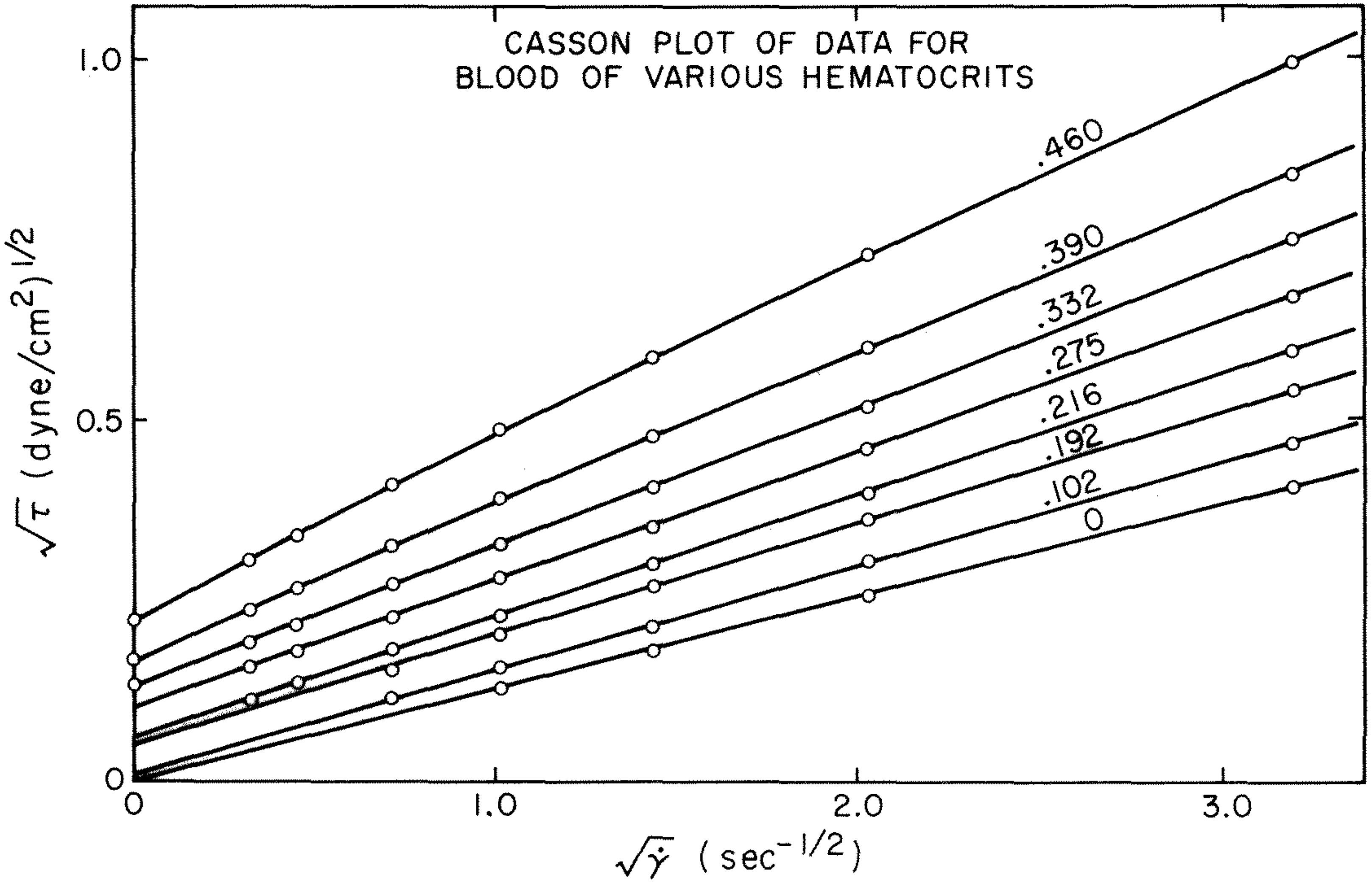

Figure 4 Casson Plot from Cokelet[(20)].

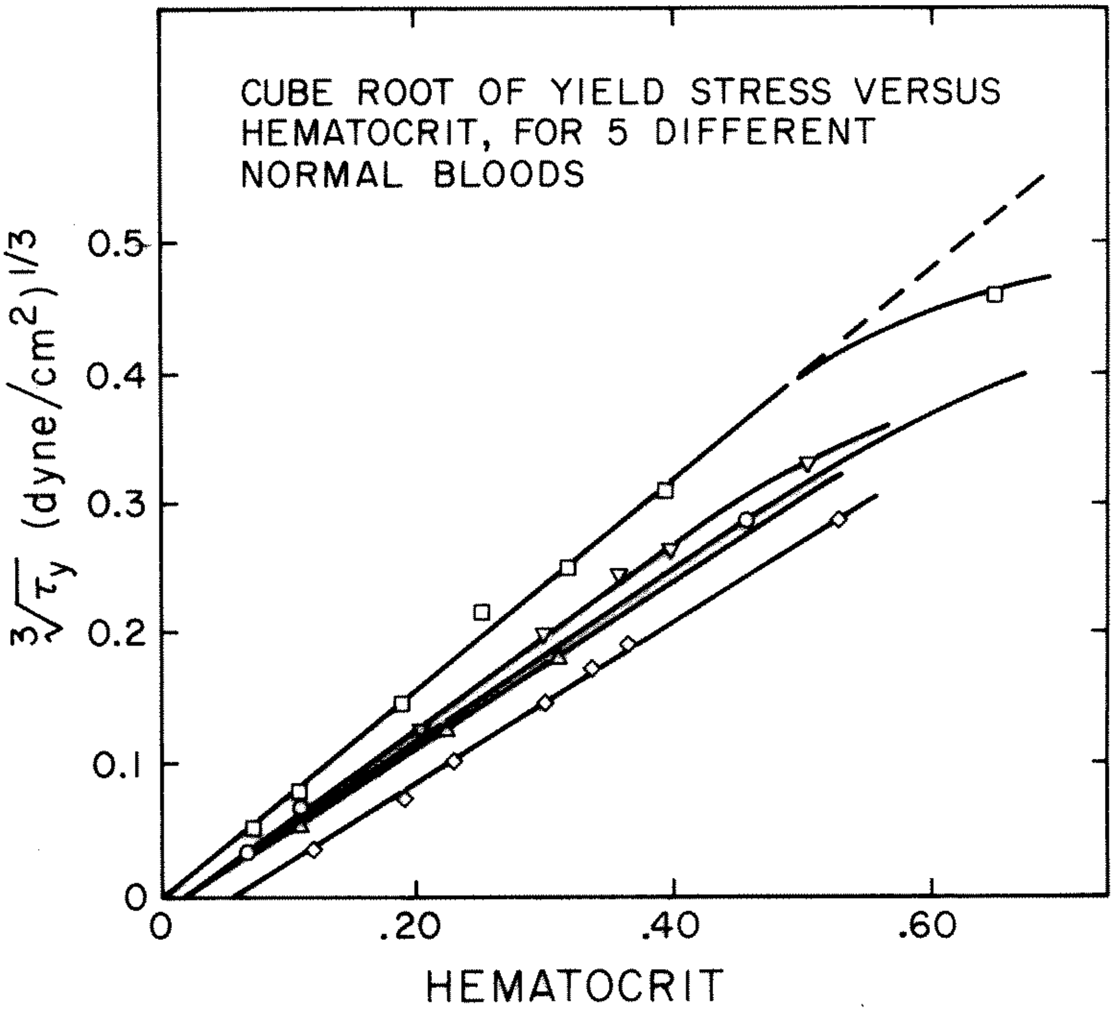

Figure 5 Yield Stress Versus Hematocrit from Cokelet(20).

The behavior of blood at higher shear rates is shown by the data of Brooks, Goodwin and Seaman plotted by Cokelet(20) in a Casson plot in Figure 6. It can be seen that blood behaves as a Newtonian fluid (i.e., has a constant slope on the Casson plot with zero extrapolated intercept) for hematocrits low enough and shear rates high enough as indicated by the data to the right and below the dotted line in this figure.

Interpretation of Rheological Data

The type of flow observed in the work of this thesis is steady flow through a tube. For this reason the usual methods of obtaining rheological data from tube flow are described here.

The easiest measurements made on a tube are the pressure drop per unit length along the tube, $\Delta P/L$, and the volume flow rate through the tube, $\dot{Q}$. Plots of $\dot{Q}$ versus $\Delta P/L$ indicate behavior of fluids in a given tube, but such plots are dependent on the tube dimensions. In order to compare data from a tube viscometer with those of other viscometers, relationships between the measurements of $\dot{Q}$ and $\Delta P/L$ and the shear stress and rate of shear strain are needed.

The shear stress at any tube radius, $\tau(r)$, can be easily obtained from the pressure drop.

$$\tau(r) = \frac{\Delta P}{2L}\, r \tag{3}$$

τ_w will be used for the wall shear stress, $\tau(R)$.

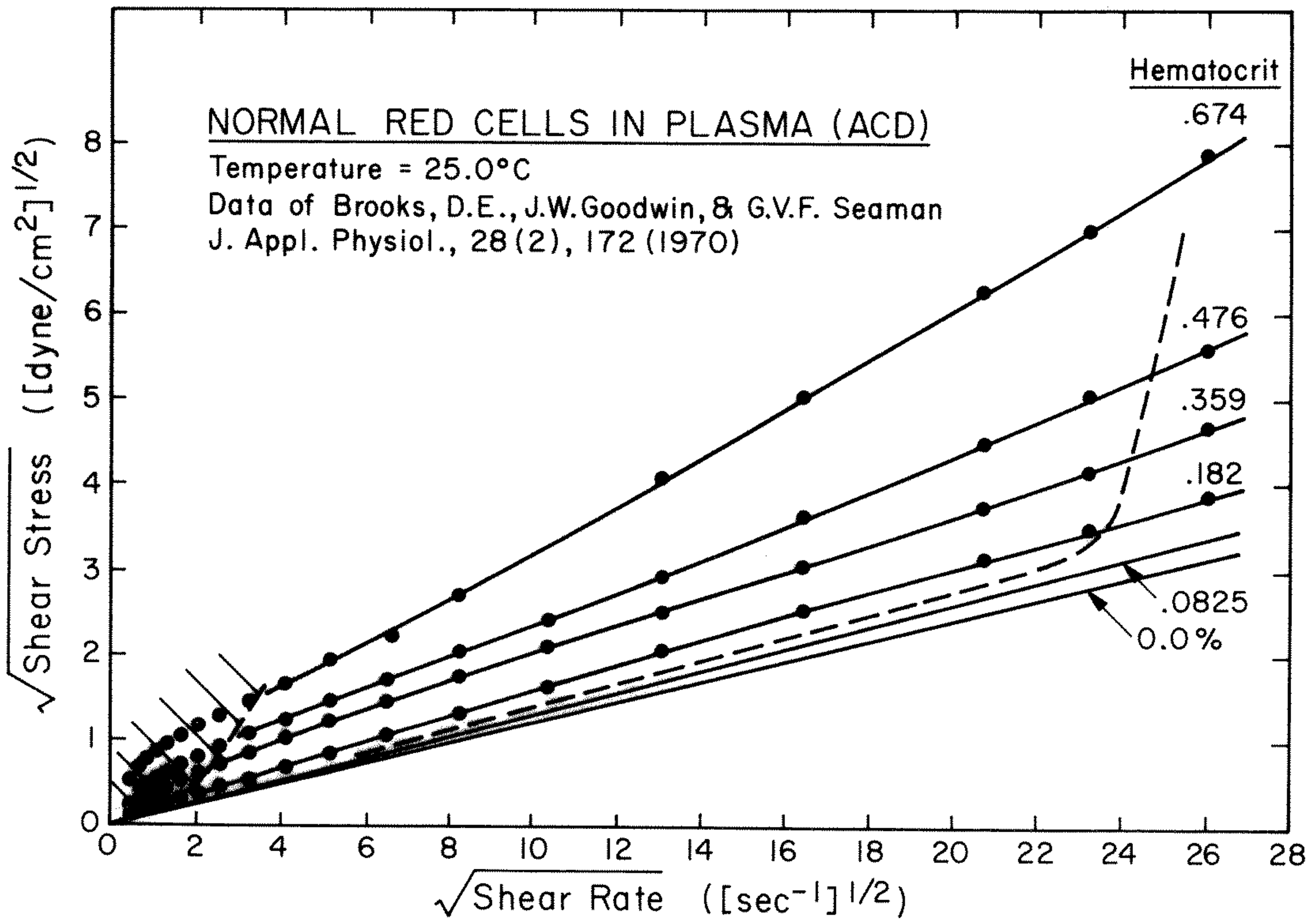

Figure 6 $\tau^{1/2}$ Versus $\dot{\gamma}^{1/2}$ Plot from Cokelet(20) Using Data of Brooks Et Al.

In order to obtain a measure of the shear rate of strain, $\dot{\gamma}$, it is necessary to make the assumption that $\dot{\gamma}$ is a function of τ only. For this assumption to be valid, the properties of the experimental fluid must not change with the radius of the tube. For blood, the essence of this assumption is that the red cell concentration doesn't vary across the tube and that the red cells can be considered small in comparison with the tube diameter, that is, that blood can be considered a homogeneous continuum for a given situation. This limitation must be kept in mind when the equations for $\dot{\gamma}$ to be derived now are used.

Using the relationship

$$-\frac{dv(r)}{dr} = \dot{\gamma}(r) \tag{4}$$

where $v(r)$ = velocity of flow in the direction of the tube axis at any radius r, the integral expression of volume flow rate through the tube,

$$\dot{Q} = \int_0^R 2\pi r \int_R^r - \dot{\gamma}(r) dr\, dr$$

can be integrated by parts using the no slip condition at the tube wall to obtain the following expression.

$$\dot{Q} = \pi \int_0^R r^2 \dot{\gamma}(r)\, dr \tag{5}$$

Using the assumption that $\dot{\gamma} = f(\tau)$, that was just discussed, and making a change of variables from r to τ, using $\tau = \Delta P r/2L$, gives

$$\frac{\dot{Q}}{R^3} = \frac{\pi}{\tau_w^3} \int_0^{\tau_w} \tau^2 \dot{\gamma}(\tau) d\tau \qquad (6)$$

Then differentiating with respect to τ_w results in an expression for $\dot{\gamma}(\tau_w) = \dot{\gamma}_w$

$$\dot{\gamma}_w = \frac{\tau_w}{\pi R^3} \left[\frac{\partial \dot{Q}}{\partial \tau_w} + \frac{3}{\tau_w} \dot{Q} \right] \qquad (7)$$

or

$$\dot{\gamma}_w = \frac{\dot{Q}}{\pi R^3} \left[\frac{\partial \ell n \, \dot{Q}}{\partial \ell n \Delta P} + 3 \right] \qquad (8)$$

This derivation due to Rabinowitsch(46) gives us two additional ways to handle the $\dot{Q}$ versus $\Delta P/L$ data of tube flow. Having constructed plots of $\ell n\dot{Q}$ versus $\ell n\Delta P$ and using equations (3) and (8), values for shear stress and corresponding values of shear rate of strain can be obtained. (For $\tau = \mu\dot{\gamma}$ where μ is a constant, the fluid is a Newtonian fluid with viscosity $= \mu = \frac{\pi \Delta P R^4}{8\dot{Q}L}$ and $\dot{\gamma}_w = \frac{4\dot{Q}}{\pi R^3}$). In addition from equation (6), it can be seen that $\dot{Q}/R^3$ is a function of $\tau_w = \frac{\Delta P R}{2L}$ only. Therefore plots of $\dot{Q}/R^3$ versus τ_w should be independent of tube dimensions; that is, these plots should coincide for any tube. It is well known that for any tube size above about 300 μm in diameter, these plots do coincide. For this reason rheological data are often presented as τ_w versus $\overline{U}$ plots where $\overline{U} = \frac{\dot{Q}}{2\pi R^3}$ is the average tube velocity divided by the tube diameter. In this way the effects of such variables as hematocrit, temperature, and plasma protein content on the flow properties of blood can be studied.

Using an 811 μm diameter tube, Barbee(1) measured the relationships between τ_w, $\overline{U}$ and feed hematocrit, H_f, for human blood. He also developed the following empirical equation to describe his results:

$$\tau_w = 8\mu_p \overline{U} \exp(4.2H_f/\overline{U}^c) \tag{9}$$

μ_p = plasma viscosity at the experimental temperature.

The values of c vary slightly with $\overline{U}$ but are given in the table below.

$.4 \leq \overline{U} < 1.0$	$c = 0.16$
$1.0 \leq \overline{U} < 3.0$	$c = .14$
$3.0 \leq \overline{U} < 17.0$	$c = .15$
$17.0 \leq \overline{U} < 30.0$	$c = .14$
$30.0 \leq \overline{U} < 50.0$	$c = .13$
$50.0 \leq \overline{U} < 100.0$	$c = .12$

Equation (9) describes well the relationships found between τ_w, $\overline{U}$, and H_f as shown in Figure 7.

Plots of τ_w versus $\overline{U}$ can be used further to study the assumption that red cells are uniformly distributed and that the ratio of red cell diameter to tube diameter is small enough for the suspension to be treated as a continuum, that is, that $\dot{\gamma} = f(\tau$, only). For tube sizes in which these plots begin to depend on tube diameter, the above assumptions are invalid.

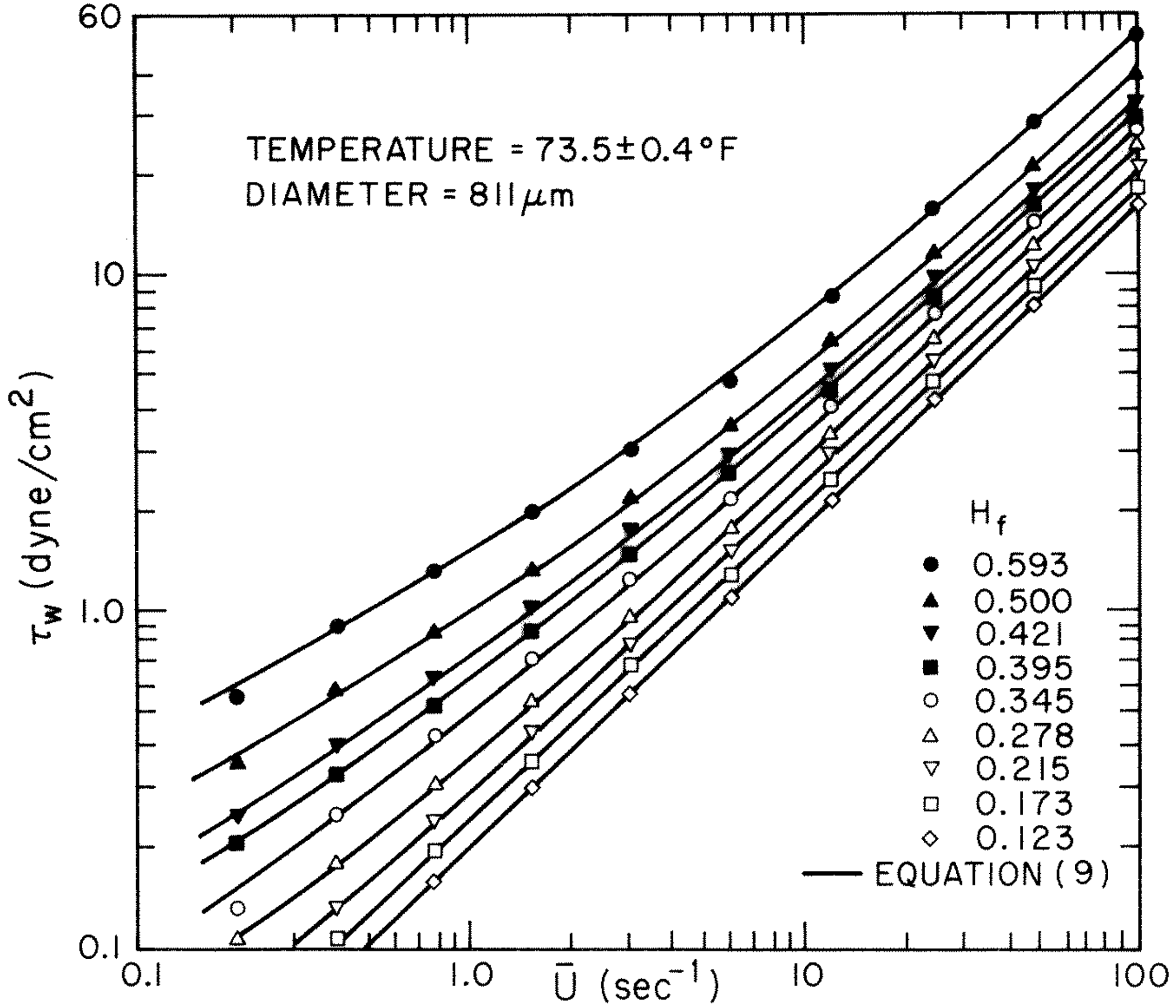

Figure 7 τ_w Versus $\overline{U}$ Data of Barbee$^{(1)}$.

Continuum Model Validity

The classical work of Fåhraeus and Lindqvist(22) showed that for blood, τ_w is lower for a given $\overline{U}$ when tube diameter is decreased from 500 μm to 40 μm. This behavior is called the Fåhraeus-Lindqvist effect and was thought to be evidence for invalidity of the continuum model for tubes of diameters in this range. However, Fåhraeus(21) also showed that blood flow from a reservoir into a small tube results in a tube hematocrit which is lower than the reservoir hematocrit. That this decreased hematocrit might explain the Fåhraeus-Lindqvist effect without contradiction of the continuum idea was suggested by Cokelet(17).

Barbee and Cokelet studied these effects in great detail in tubes of diameter from 221 μm to 29 μm(2). They found that the ratio of tube hematocrit to feed hematocrit (tube relative hematocrit, H_r) is greatly dependent on the tube diameter and the feed reservoir hematocrit for tube diameters in this range. This dependence is shown in Figure 8. They also demonstrated that H_r is independent of blood flow rate, the protein content of the suspending medium, the stirring rate and therefore the state of aggregation of red cells in the reservoir, and the entrance conditions for the tube. Another of their results that is especially significant is their measurement of the outflow hematocrit, H_d, which is the percentage of red cells in the blood collected at the downstream end of the tube. For tubes down to 59 μm in diameter, the outflow hematocrit was found to be equal to feed hematocrit and therefore greater than the tube hematocrit. From these results, Barbee

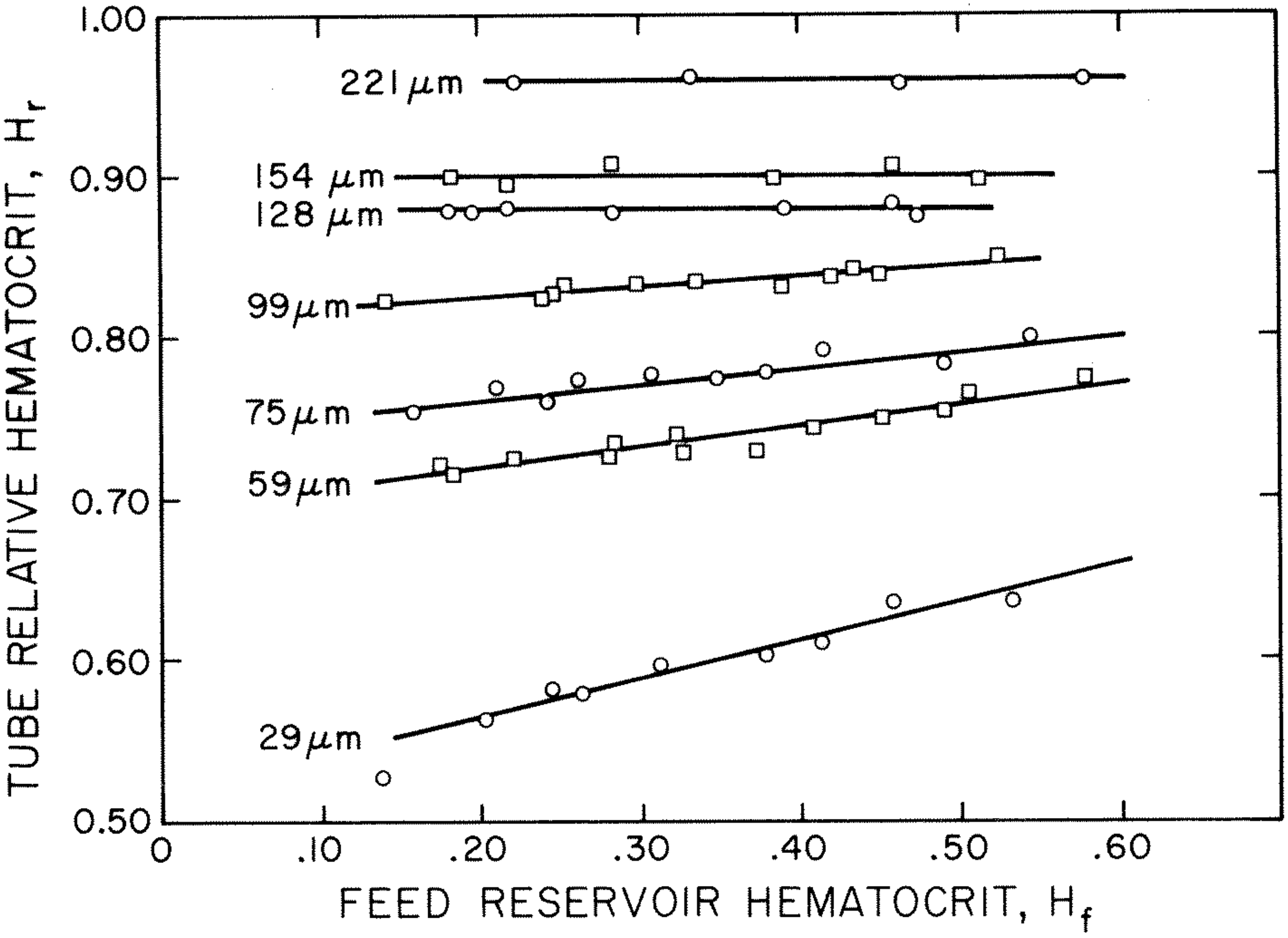

Figure 8 Tube Relative Hematocrit Variation with H_f and Tube Diameter (Cokelet)[20]

and Cokelet concluded that the red cell distribution within a tube varies with tube radius. In order for the outflow hematocrit to be greater than the tube hematocrit, the red cell average velocity must be greater than the fluid average velocity in the tube. This implies the red cells are distributed with a higher concentration in the regions of higher velocity.

In light of this evidence for non-uniform hematocrit in tubes of diameter of 221μm and below, the following additional results of Barbee and Cokelet$^{(3)}$ are surprising. They were able to predict the τ_w, $\overline{U}$, hematocrit relations for blood in tubes as small as 29μm in diameter from the data in large tubes just by taking into account the actual tube hematocrit. The equation (9) which describes the flow behavior of blood in tubes large enough so that $H_r = 1$ also describes the behavior in a 29μm tube if $H_t = H_r H_f$ is substituted for H_f. Figure 9 shows these results. The discrepancy between the line marked 811μm diameter, $H_f = .559$, and the data points from 29μm tube at the same H_f demonstrates the effect noticed by Fåhraeus and Lindqvist. The solid lines, drawn from equation (9) using the actual tube hematocrit for 29μm tube, coincide with the data points measured in a 29μm tube.

This unique relation for τ_w, $\overline{U}$, H is unexpected for the same tubes in which the hematocrit measurements indicate that concentration distribution is a function of tube diameter. The useful limits of the continuum techniques in predicting blood flow behavior have not yet been clearly defined. This discussion of the continuum model limits

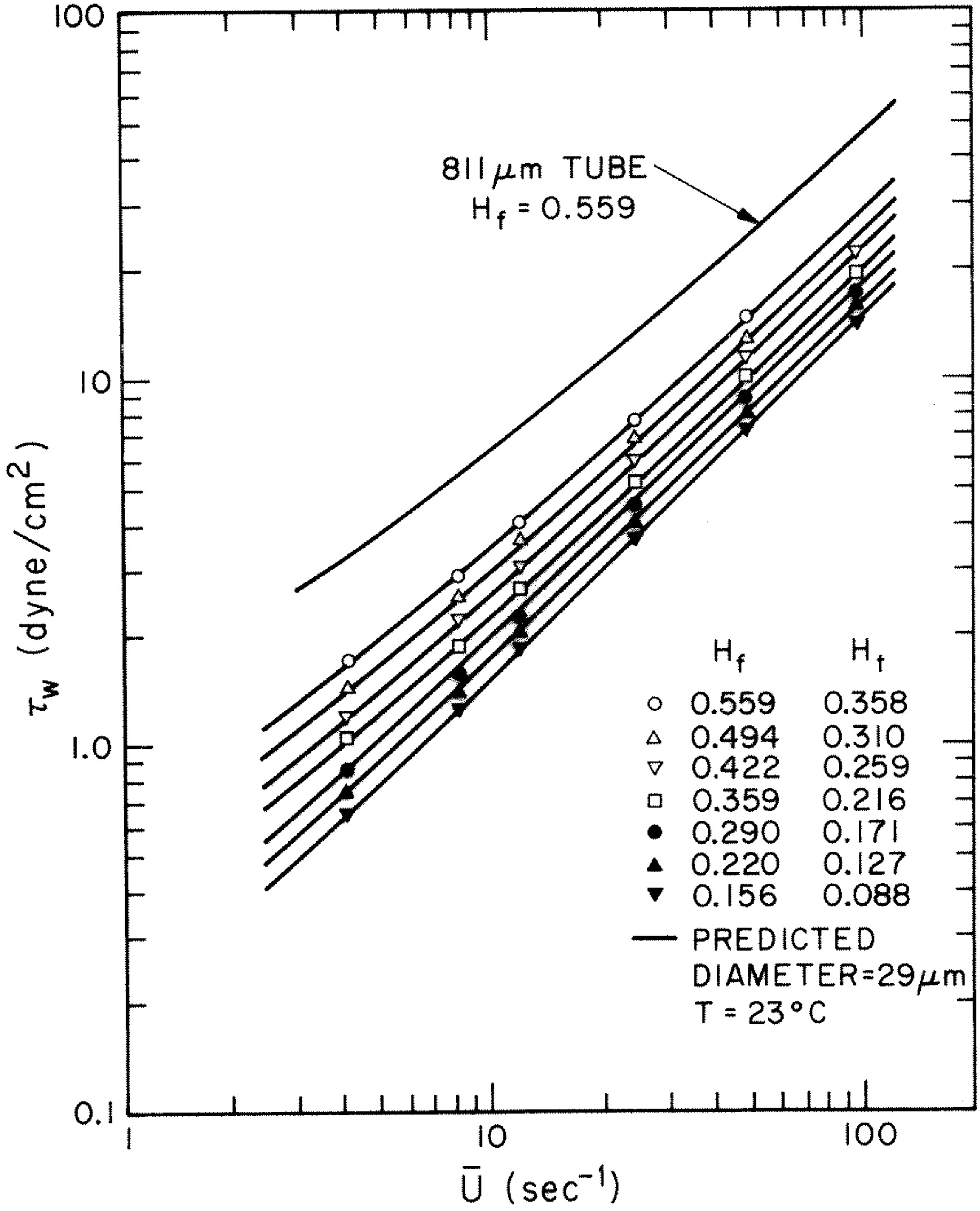

Figure 9 Prediction of τ_w Versus $\overline{U}$ Behavior for 29μm Diameter Tube Using Data Obtained in 811μm Diameter Tube (Cokelet)[20].

will be continued later when the Barbee-Cokelet data is used to interpret velocity profile measurements.

III. MEASUREMENT OF BLOOD FLOW IN MICROVESSELS

If a method of measuring blood velocities is to be useful in monitoring events in a bed of microvessels it must be able to measure flow rates on the order of 10^{-7}cc/sec in vessels too small to see. It must do so quickly enough to record the pattern of flow before the conditions change. Any type of sampling or probing can easily cause disturbances larger than the original flows to be measured. Several methods for making measurements on the microscope image of the vessels using the red cells in suspension as tracers have been proposed. A review of these methods can be found in Wayland(55). An additional discussion of some velocity profile methods is presented in Appendix A. Those investigations which have used methods or produced results particularly relevant to the results of this thesis are described here.

High Speed Motion Pictures

High speed motion pictures provide the most straightforward method of measuring microscopic flows. The movements of individual cells are followed from frame to frame and the distance moved, divided by the time between frames, gives the measure of velocity. This method is limited to those hematocrits, flow rate, and tube diameter combinations for which individual cells can be followed in successive frames. For normal hematocrits (.45-.50) it is very difficult to distinguish cells even in tubes as small as 40μm diameter. The flow rate limitations are largely determined by the camera used but at 500fr./sec (highest available speed in a pin registered camera) it is difficult to measure flow rates high enough to break up the red cell aggregates throughout the tube. Perhaps the most serious limitation of this method is the tedious and time consuming frame-by-frame analysis.

In spite of these difficulties the use of motion pictures has yielded velocity profiles for blood. Bugliarello and Hayden(10), Bugliarello, Kapur and Hsiao(11), and Bugliarello and Sevilla(13) measured velocity profiles in this way from tubes of 40 μm, 70 μm, and 83 μm inside diameter with feed reservoir hematocrits up to .40 for the smaller tubes. They used a camera capable of shutter speeds up to 3000fr./sec with continuously moving film. Although the film was always accelerating or decelerating throughout the measurements, the instantaneous speed was determined by the length of streaks on the film produced by timing lights. From their published velocity profiles, the trends in the profile shapes with changes in tube size, hematocrit, and $\overline{U}$ are not clear. According to these investigators, the profiles are blunt but tend toward Newtonian flow behavior (parabolic shape) at larger diameters, faster flow rates and lower hematocrits. Many of their profiles are in fact parabolic within limits of experimental error. These profile shapes will be analyzed in more detail later when they are compared with the results of this thesis work.

Double-Slit Photometric Method

A much less tedious method for measuring red cell velocities in capillaries was developed by Wayland and Johnson(52, 53). They focused the image of the flowing blood on a screen penetrated by two slits each connected to a photomultiplier. The direction of flow was aligned with the slits such that a red cell would pass both slits in succession and therefore cause successive modulations in the output of each of the photomultipliers. Determination of the time delay between the similar events in the two signals gave a measure of the velocity of the red cells. This method of measurement of red cell velocities is referred to as the "double-slit photometric method".

Three methods of measuring the time delay between the two signals were demonstrated. The most straightforward way involves spreading out the data as much as possible on paper using a pen recorder, choosing events which appear identical on each of the two records and measuring the distance and thereby time delay between corresponding events. Another method uses computer crosscorrelation. The photomultiplier signals are recorded on analog tape and then digitized. A series of crosscorrelations are carried out between the two signals with one signal shifted varying amounts of time with respect to the other. That time shift which gives the maximum correlation corresponds to the actual delay between signals. In addition, an on-line analog method of measuring the velocity was proposed. This method electrically selects similar peaks, measures the time delay between them, and sends a signal proportional to the reciprocal of the time difference to a pen recorder.

The double-slit method was originally developed only for capillaries (vessels large enough for only one or two cells to fit across the tube diameter). However, Gaehtgens, Meiselman and Wayland(27) evaluated the extension of the method to tubes 25μm to 130μm inside diameter. In making this evaluation, three possible limitations were considered. One was the focal depth of the optical system; it is desirable to measure velocities from a depth shallow with respect to the tube diameter so that velocity profiles can be obtained. A second limitation was the amount of contrast between the flowing particle and its environment; when many cells are present across the tube diameter there may not be sufficient contrast for a single cell to make a sharp modulation in photomultiplier output. The third limitation was major rotational or lateral motion of the particles; a cell which rotates or moves laterally between slits will make a different shaped modulation in the two photomultiplier signals making correlation difficult.

The first limitation was dismissed when the microscope objective used was shown to give a depth of field of less than 3μm. The second limitation was felt to be the major one but was also dismissed when preliminary experiments showed the light sensing equipment to be so sensitive that differences in light transmission between the dark edge of a red cell membrane and its hemoglobin interior were resolved. The third limitation was evaluated by comparing the output of two photomultipliers. The great similarity of the two signals indicated that the spacing of the two slits is sufficiently small to make rotation or lateral movement of cells between slits improbable. From these results, it was concluded that the double-slit method is applicable to blood velocity measurements in tubes or vessels up to 130μm and possibly higher.

Using this method to measure red cell velocities at different radial positions across the tube, Gaehtgens, Meiselman and Wayland(29) found the measured profiles considerably blunted in comparison to a Newtonian profile. Flow rates, $\dot{Q}_{exp}$, were calculated by integrating the experimental profiles. These were compared with the flow rate, $\dot{Q}_{par}$, for a parabolic velocity distribution with the same centerline velocity. The obtained ratio $\dot{Q}_{exp}/\dot{Q}_{par}$ ranged between 1.69 (25μm diam. tube) and 1.001 (127μm diam. tube) and was found to increase with decreasing tube diameter. A simultaneous volume flow rate measurement independent of the velocity measurements was not carried out. The effect of hematocrit on the shape of the particle velocity profiles was reported as rather slight although a large range of hematocrits was not investigated.

With velocity profiles available and an on-line analysis method under development, the double-slit photometric method showed promise of becoming an excellent tool for monitoring events in the microcirculation of a living animal. The velocity profile information allows flow rate determination from a single velocity. The on-line analysis is a great improvement in convenience in comparison to frame by frame motion picture analysis. In addition, the ranges of flow rate, hematocrit, and tube diameter that can be handled are greater for the double-slit method than for any other method available.

Gaehtgens, Meiselman and Wayland(28, 30) have used the double-slit method on living vessels. Information about flow patterns and local regulatory phenomena was obtained from studies on the mesenteric microvessels of cats. In addition, Gaehtgens(31) demonstrated pulsatile blood flow velocities in both arterioles and venules and thereby upset the commonly held view that the pulsations of arterial flow are completely damped out as blood flows through the network of the capillary bed.

Intaglietta, Tompkins and Richardson(37) have developed an on-line system for measurement of red cell velocities in living animals based on the double-slit photometric method. They measured velocities in the living cat omentum and found pulsatile components in both venules and arterioles. Their system enabled them to determine the phase shift between the pulses of flow found in these microvessels and pulses of the main arteries.

Frequency Analysis of Single Photometric Signal

The red cell modulations in the signal from a photomultiplier can be used in another way to measure the red cell velocities. Wiederhielm(58) has shown, through spectral analysis of this signal, that the upper limit of the frequency spectrum is linearly related to the red cell velocities. He has measured blood flow rates in glass capillaries and living vessels through frequency analysis of a photomultiplier signal.

The potential and several limitations of this method are discussed in a later section where results obtained in this laboratory through the use of this method are compared with results from the double-slit method.

IV. EXPERIMENTAL APPARATUS AND PROCEDURE

Description of Experimental Arrangement

The experimental equipment used for this thesis work included apparatus for double-slit photometric measurements and pressure drop volume flow rate measurements on glass and plastic capillary tubes. A sketch of this equipment is shown in Figure 10. (The numbers in the text refer to locations on this drawing).

The capillary tube (1) is mounted vertically to prevent asymmetries due to settling of the red cells. Most capillaries used were hand-drawn glass coated with Siliclad and supported by a frame made of glass slides and glass standard taper joints. (Details of the construction and calibration of several types of glass and plastic capillary tubes are described in Appendix B).

At each end of the capillary is a blood reservoir (2) made of lucite. The seal between capillaries and chambers is by glass standard taper. Each chamber contains a thermistor and an Endevco model 8503 pressure transducer (3). A small bar magnet (4), held in the center of each chamber by a pin is used to keep the red cells from settling. Air driven magnetic wheels (not shown) fixed outside the chambers keep the bar magnets continuously rotating.

Blood is pushed through the capillary tube by a Harvard Apparatus Co. syringe pump (5). Since this pump has been calibrated, the volume flow rates are known. The pump is connected by teflon tubing to the bottom chamber. Oscillatory flow can be developed by connecting a

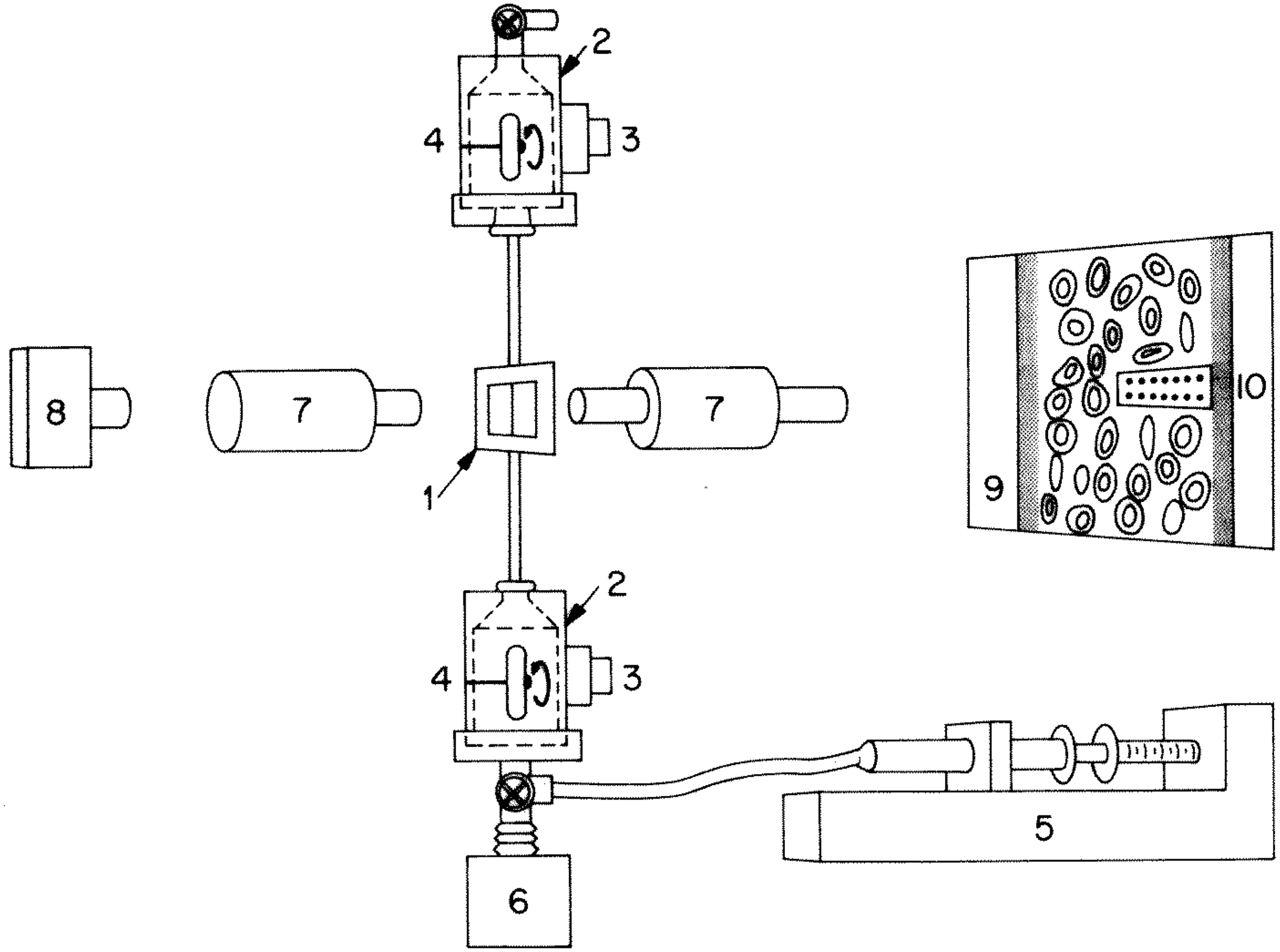

Figure 10 Double-Slit Photometric Velocity Profile Apparatus.

small bellows pump (6) in place of the syringe pump. The bellows pump is a vibration generator connected to the chamber through the bellows and driven by a function generator.

The entire assembly of chambers, gages, and capillary tube is mounted on a modified Sears universal vice which allows the capillary to be moved in and out of the field of the microscope (7) which is mounted separately with optic axis horizontal. Initially, a UMK 50x/0.60 objective (used dry with equivalent magnification and aperture of 32x/.40) with either a 10x or 15x eyepiece was used. Illumination for double-slit measurement is provided by a 100 watt mercury arc lamp (8). For motion pictures, a Chadwick-Helmuth Strobex xenon flash lamp synchronized with camera shutter was substituted for the mercury arc.

The image of the flowing blood is projected on a screen (9) penetrated by a 2x7 array of phototransistors (10) arranged in pairs such that the two members of each pair define a line parallel to the direction of flow. Usually, the seven pairs span half the tube image. (The phototransistors replace the photomultipliers mentioned in the description of the Wayland and Johnson experiments.) For some experiments a Milliken pin-registered motion picture camera capable of 500fr./sec was positioned in place of the screen.

The signals from the phototransistors, which are proportional to the light intensity of the image, are amplified and displayed on an oscilloscope and transmitted either to an analog tape recorder for later analysis or directly to a special analog analyzer built in this laboratory by Dale Elmore. When this analyzer is used, a signal proportional to red cell velocity is recorded on paper by a Sanborn recorder, along with the difference in pressure between the two chambers and the temperature reading.

The functioning of the Elmore analyzer, which is similar in principle to the analog analyzer proposed by Wayland and Johnson, can be observed on the oscilloscope simultaneously with the phototransistor signals. When the upstream signal exceeds a certain voltage, the analyzer differentiates both signals. As the upstream signal derivative passes through zero indicating a peak in the signal, the analyzer initiates a pulse. This pulse is terminated by a zero crossing of the downstream derivative signal. The width of the pulse is proportional to the time delay between signals. This pulse is displayed on the oscilloscope adjacent to the phototransistor signals as shown in Figure 11. This simultaneous display allows adjustment in the signals and a means of checking that the analyzer is actually finding similar peaks. The time delay is divided by an analog divider and transmitted to the recorder as a velocity.

Velocity measurements are continually taken and averaged into the existing reading. The calibration of the analyzer is carried out by measuring a known delay between two function generator signals.

This analog analysis method was used for all the results to be presented. Some of the same data were processed by digital computer crosscorrelation and by hand measurement of distance between similar events as discussed in the description of the work of Wayland and

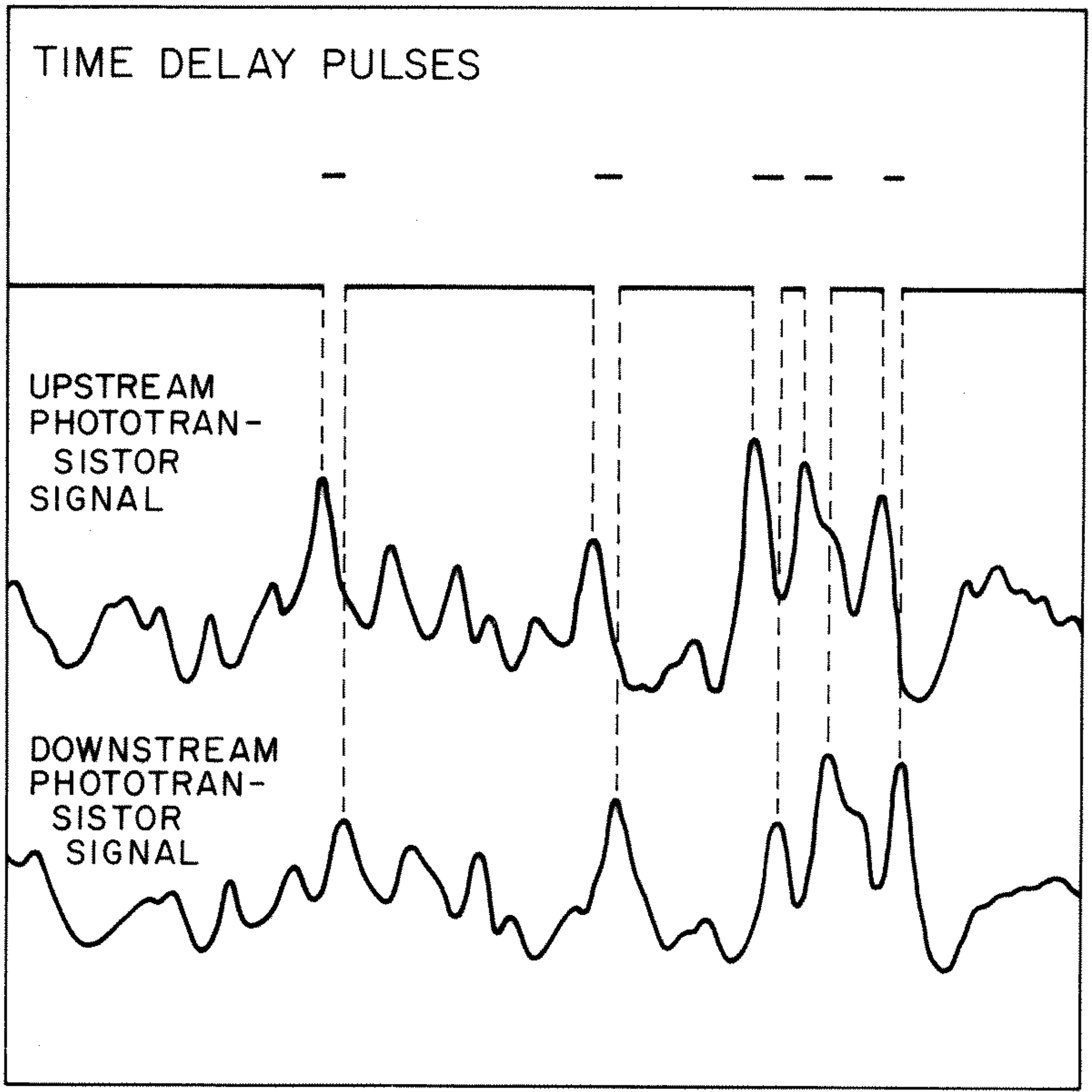

Figure 11 Oscilloscope Display of Operation of Elmore Analyzer.

Johnson; the results from all three methods were consistent.

Procedure

All blood samples were human blood obtained from a commercial blood bank. The anticoagulant in these samples is standard ACD solution. The actual fluids used were red cells suspended in plasma prepared in the following manner:

1) The sample was centrifuged at 3000g for 10 minutes resulting in separation of red cells and plasma.
2) The plasma layer was removed and saved.
3) The buffy coat, which is a layer of white cells and platelets between the red cells and plasma, was removed.
4) A quantity of red cells sufficient to give the desired hematocrit was resuspended in plasma.
5) Final suspension was filtered through 14μm neoprene filter to remove any particle clumps or debris that might clog experimental tube.

For steady flow measurements these samples were introduced into the bottom chamber only. The syringe, teflon tubing and upper chamber were filled with buffered isotonic (the same osmolarity and pH as blood) saline solution.

The experimental capillary tubes were rinsed thoroughly with isotonic saline and then inserted into the filled chambers. The position of the assembly was then adjusted so that the image of flowing blood was displayed on the phototransistor array or camera shutter.

Magnification was adjusted by motion of the screen or camera until the tube just spanned a distance twice the phototransistor array width or once the film width. Focal position at the diametral plane was judged according to recognition of patterns predicted by analysis of the optical distortions. (Appendix C is a discussion of the optical distortions produced by refraction of light at the inside and outside wall of the tube).

Once the image was focused and positioned on the phototransistor array the syringe pump was turned on, the analog analyzer was calibrated, and the phototransistor signals were adjusted. When the differential pressure trace indicated steady pressure or the desired pressure, readings of velocity were started or transmission of phototransistor signals to the tape recorder was begun. The oscilloscope display of signals and time delay pulses was continually observed to assure the analog analyzer was functioning and that the two signals were nearly superposable.

After a set of velocity readings were taken the blood was removed from the chamber in order to remeasure the hematocrit and check the condition of the red cells by microscopic observation of the cell shapes.

Velocity readings were obtained at the location of each of the seven phototransistor pairs. The velocity profiles were constructed by plotting these values at radial positions obtained through the optical correction calculations of Appendix C.

V. MEASURED PROFILES AND THEIR INTERPRETATION

Objectives of a Further Study of the Double-Slit Method

This thesis is a further investigation of the double-slit photometric method and the velocity profiles of blood in steady flow through a microscopic tube. The reason this study was begun was the intention of using the double-slit method in an investigation of blood in pulsatile flow at amplitudes for which blood in steady flow shows behavior which is far from Newtonian. The apparatus just described was designed and built to measure pressure drop, $\Delta P(t)$ and flow rate, $\dot{Q}(t)$, for blood being pulsed at various frequencies and to compare these results with steady flow data. The double-slit apparatus was included as a means of instantaneous volume flow rate measurement at very low amplitudes of flow. Most volume flow rate measurement methods for microscopic tubes are limited at low flow rates in unsteady flow because of the compressibility of blood in the chambers due to trapped air. Integration of the velocity profiles obtained through the double-slit method seemed an excellent way of measuring the volume of fluid actually flowing through the tube at any instant of time. In order to extend with confidence the use of the double-slit method to a volume flow rate measurement method, it was necessary to determine how accurately the integrated velocity profile measured the known flow rate. In addition, if a comparison with steady flow results was to be made, it was desirable to determine the profile shapes in steady flow for the particular tube size to be used. (The previous profile measurements of

Gaehtgens(29) showed that profiles were very dependent on tube size). These two determinations were the first goals of this investigation of the double-slit method.

Typical Profiles

Velocity profiles were taken in steady flow with known flow rate produced by the syringe pump. Typical profiles are shown in Figures 12-18. The velocities are expressed as $v(r)/\overline{V}$ where $\overline{V}$ is the average velocity in the tube. Also given on each of these figures is a parabola of the correct volume flow rate (solid line) and the ratio, $(\dot{Q}_m/\dot{Q}_p)_1$ of volume flow rate obtained by integration of the profile, $\dot{Q}_m$, to the volume flow rate known from the pump $\dot{Q}_p$. $(\overline{V}=\dot{Q}_p/\pi R^2)$

The values of $\dot{Q}_m$ are on the average 6% below the $\dot{Q}_p$. Many causes of error, such as unsteadiness of flow or uncertainties in magnification, could account for an occasional 6% discrepancy in these values, however, the reason $\dot{Q}_m$ was generally low was not clear. The possibility of leaks was considered but eliminated by collecting the flow at the downstream end and finding it within 1/2% of the pump flow rate. That the red cell velocity is actually lower than the local plasma velocity is another possibility but is considered unlikely.

There are also several other surprising features of the profile shapes in Figures 12-18: 1) all profiles are far different from the parabolic profile of a Newtonian fluid even at low hematocrit, and high $\overline{U}$; 2) there is no trend in shape changes with hematocrit or with $\overline{U}$, and, 3) velocity points taken very near the wall don't seem to approach the zero velocity expected from the no slip condition at the tube wall. This

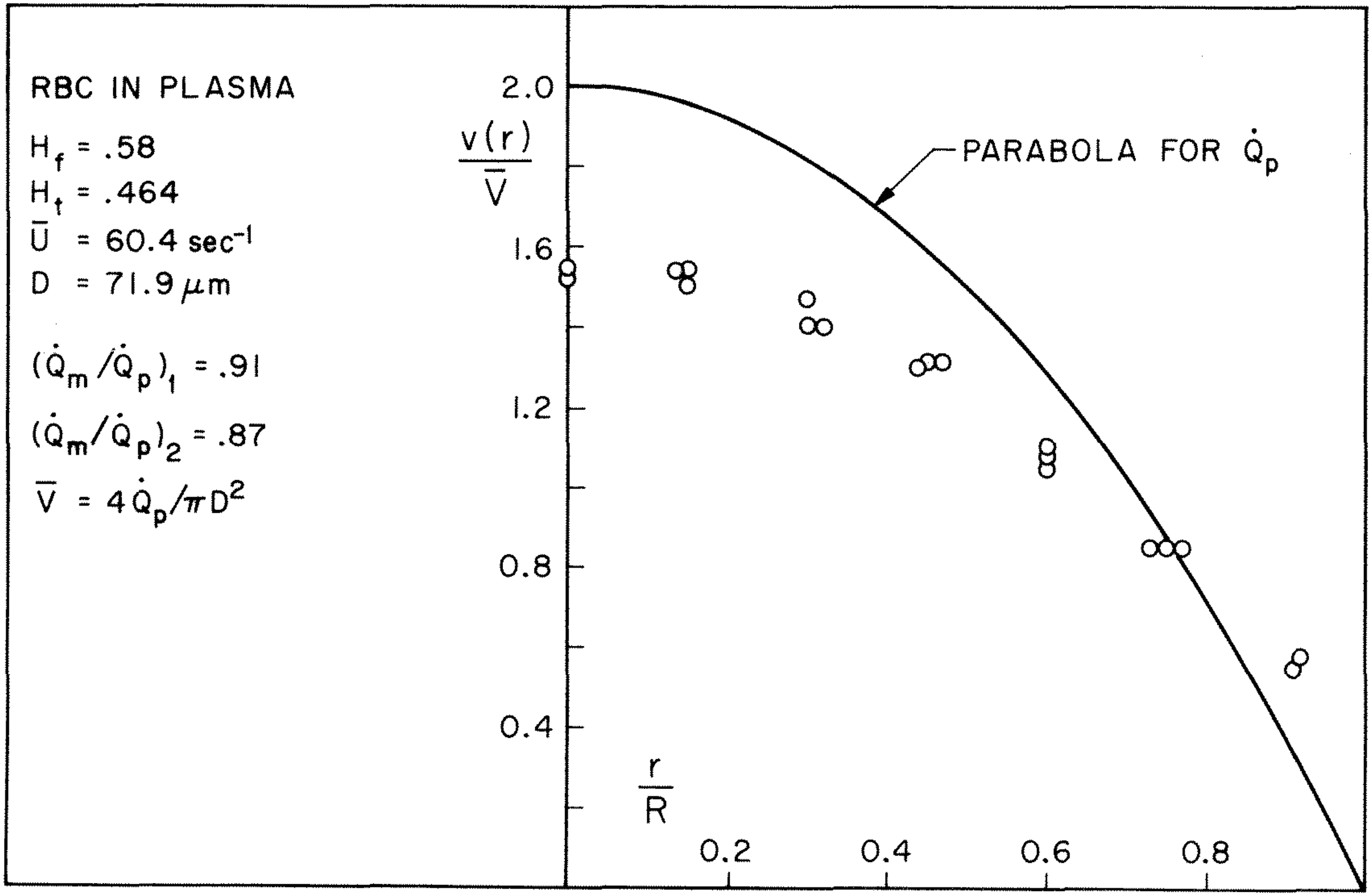

Figure 12 Double-Slit Velocity Profile.

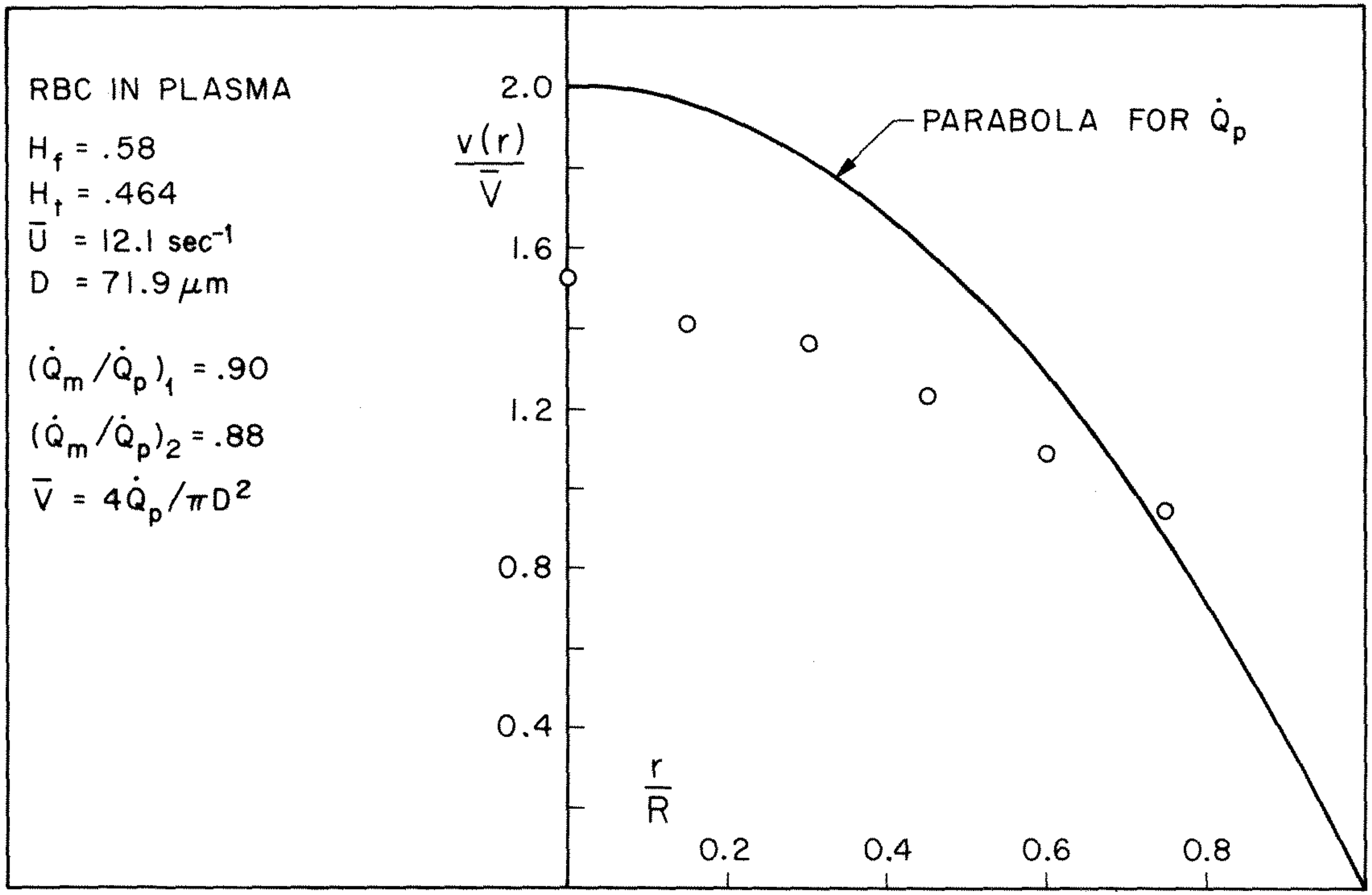

Figure 13 Double-Slit Velocity Profile.

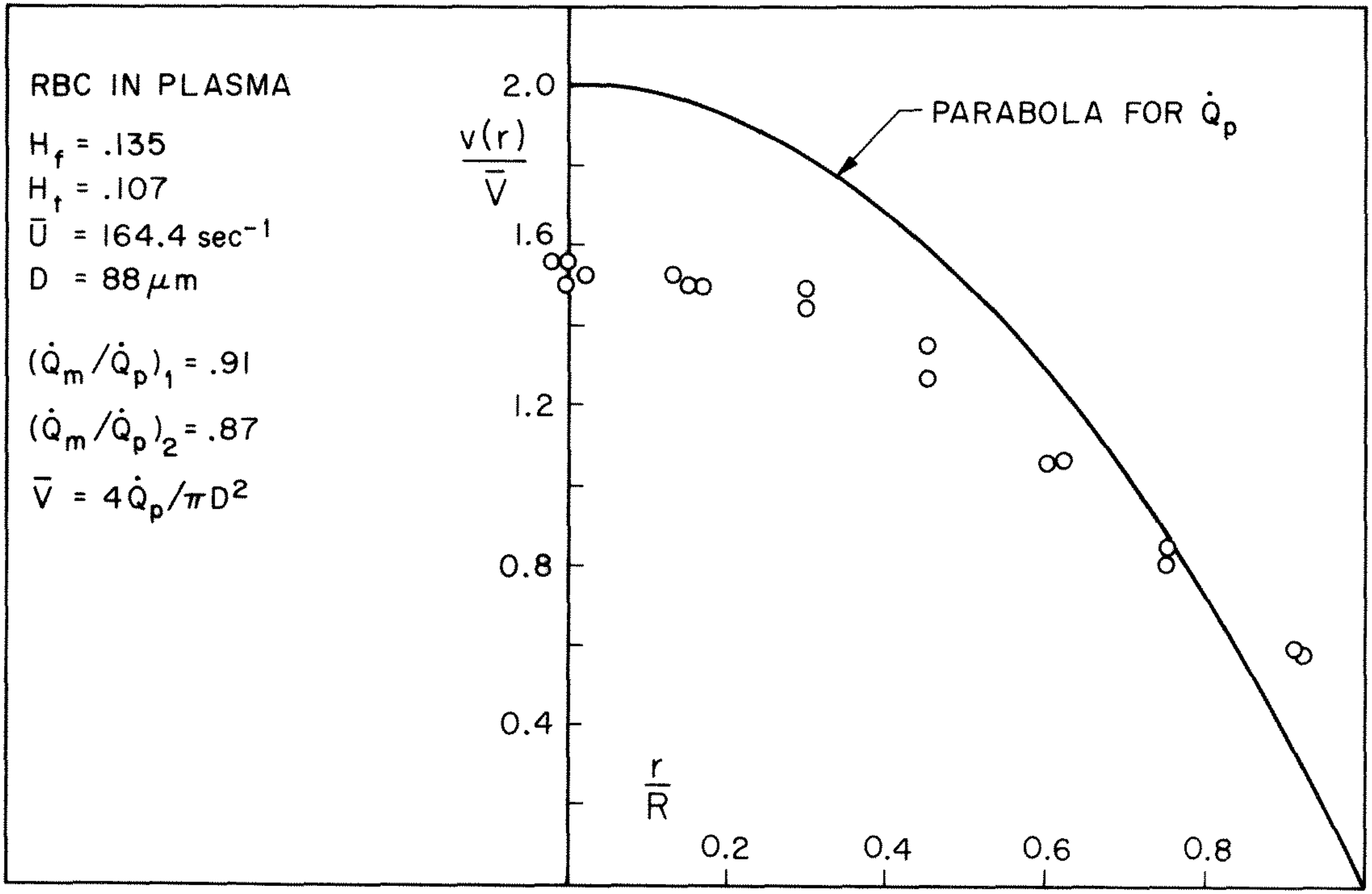

Figure 14 Double-Slit Velocity Profile.

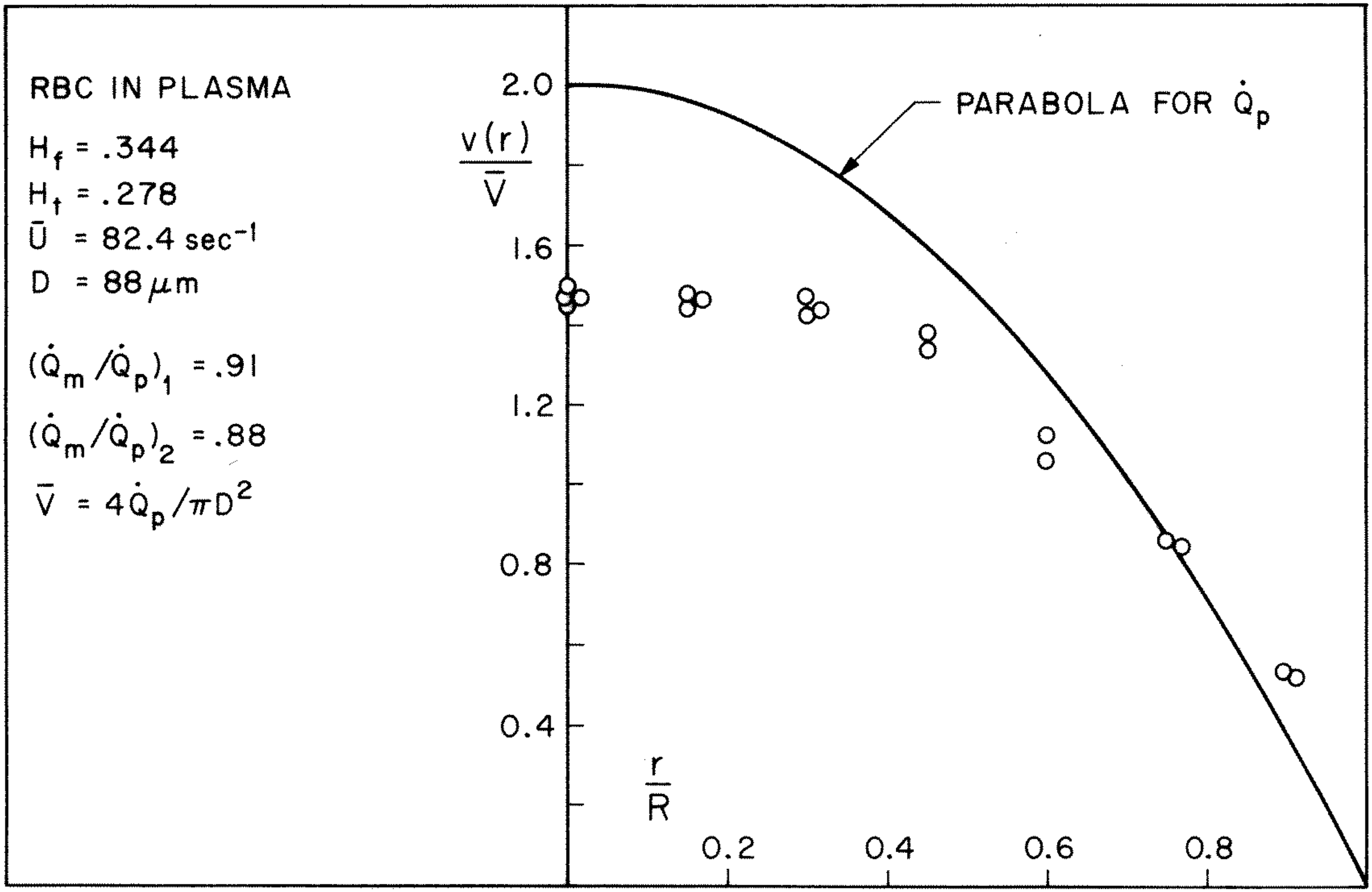

Figure 15 Double-Slit Velocity Profile.

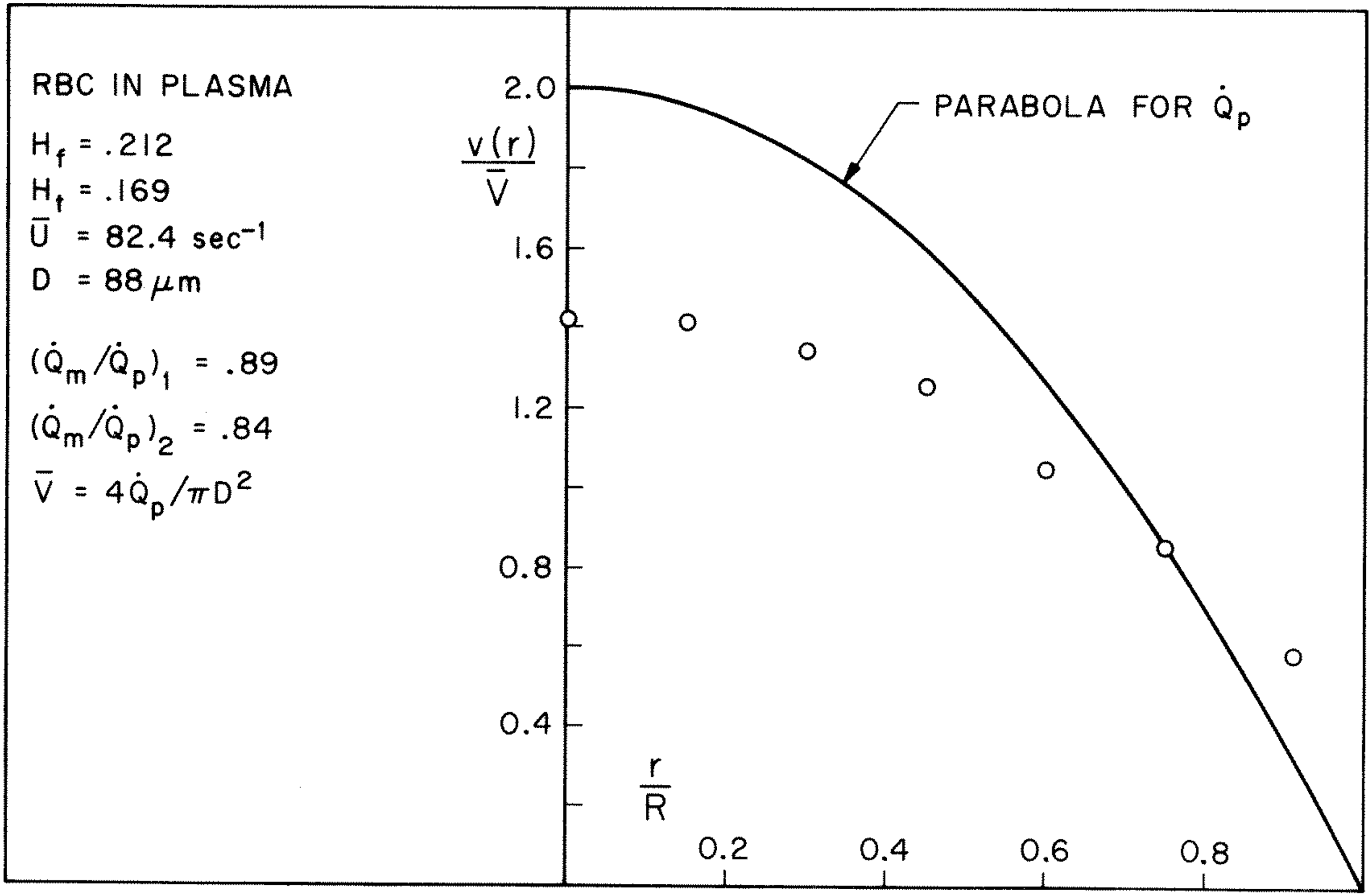

Figure 16 Double-Slit Velocity Profile.

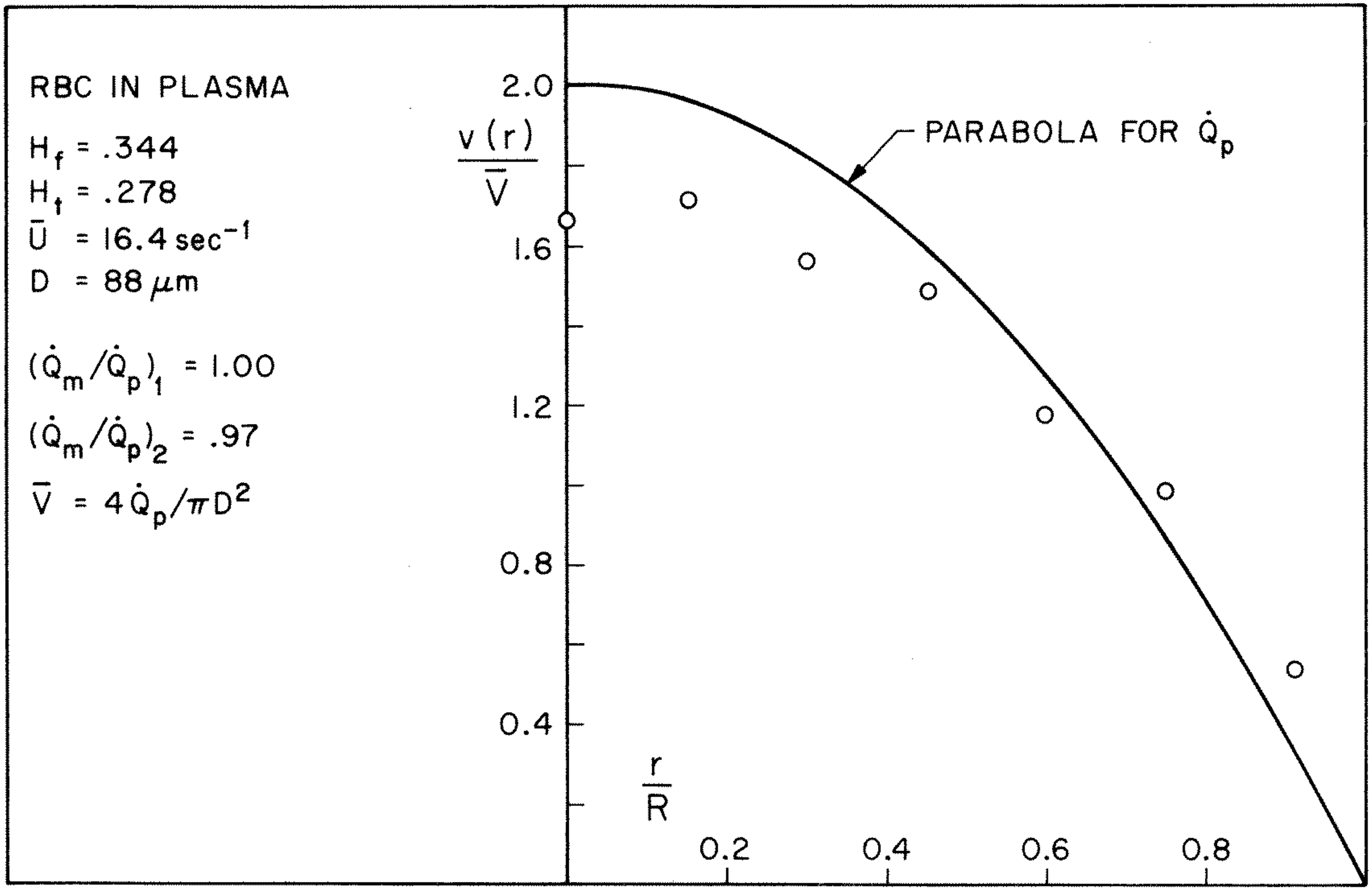

Figure 17 Double-Slit Velocity Profile.

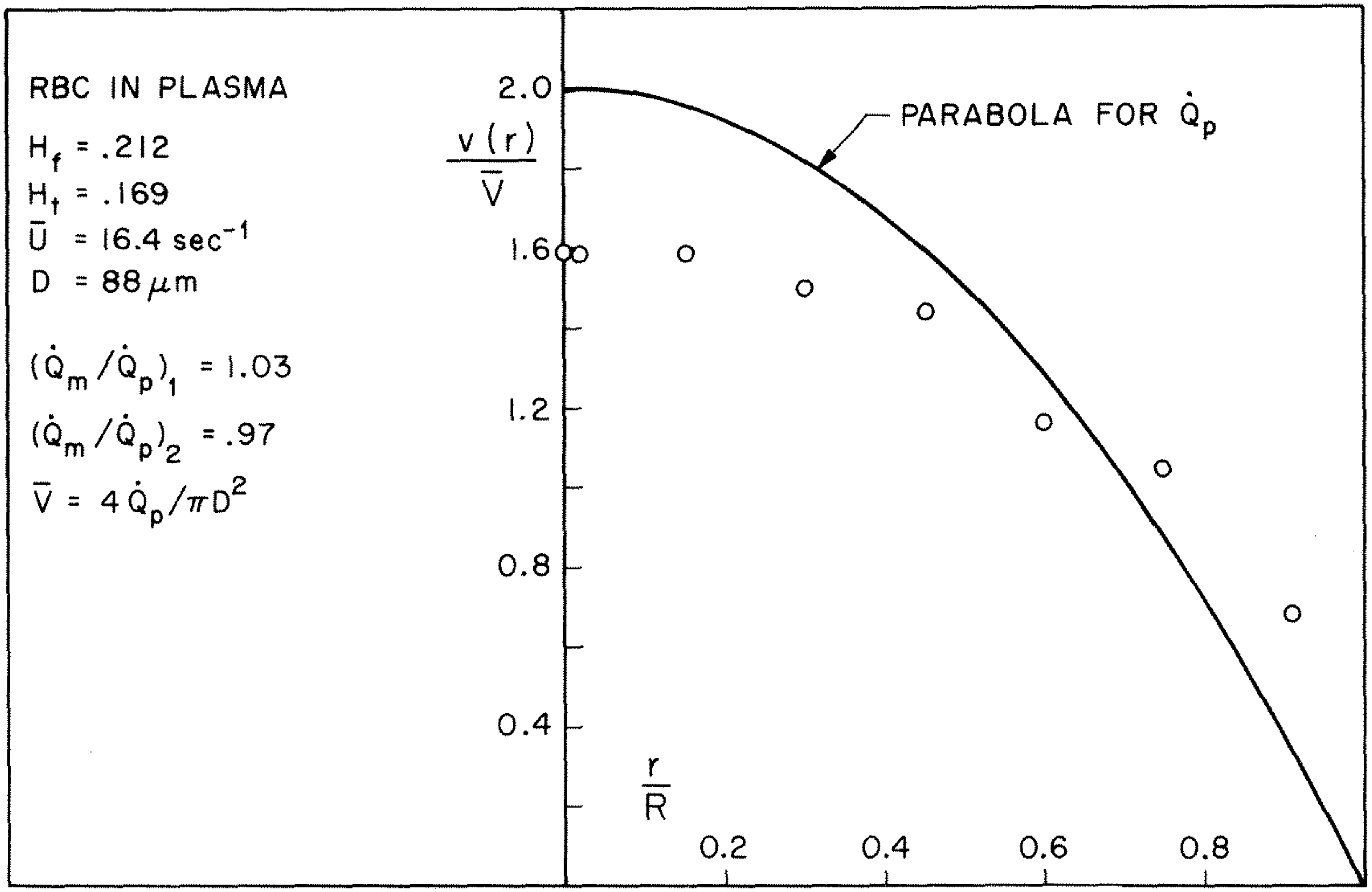

Figure 18 Double-Slit Velocity Profile.

high velocity at the wall is often discarded on the grounds of possible optical distortions here. However, discarding this point causes the integrated volume flow rate to fall even farther below pump flow rate. For profiles integrated without the wall point, $\dot{Q}_m$ is on the average 10% below $\dot{Q}_p$. This ratio, $(\dot{Q}_m/\dot{Q}_p)_2$, is included in Figures 12-18.

These profiles seemed to raise more questions than they answered. For this reason, an attempt to measure a known case was made. The one profile shape that is known is the parabolic shape for plasma which has been shown to be a Newtonian fluid. Profiles for plasma alone cannot be measured since some red cells are needed as tracers; however, a suspension as near as possible to plasma was prepared. A profile was measured for a suspension of 6% red cells in isotonic saline. This suspension has no cell aggregation, no yield stress, and a stress-strain rate relation which is a straight line. The measured profile is shown in Figure 19. The shape is essentially the same as all the other profiles and certainly not parabolic.

Because of the above results which show volume flow rate discrepancies and very blunt profile shapes which do not change in a way which is rheologically reasonable, there was considerable doubt that actual velocity profiles were being measured. The possibility of a distortion in the double-slit method was suggested and an investigation to uncover the distortion was begun.

Distortion Considerations

Depth of Field

The first possible explanation of the blunt profiles that was

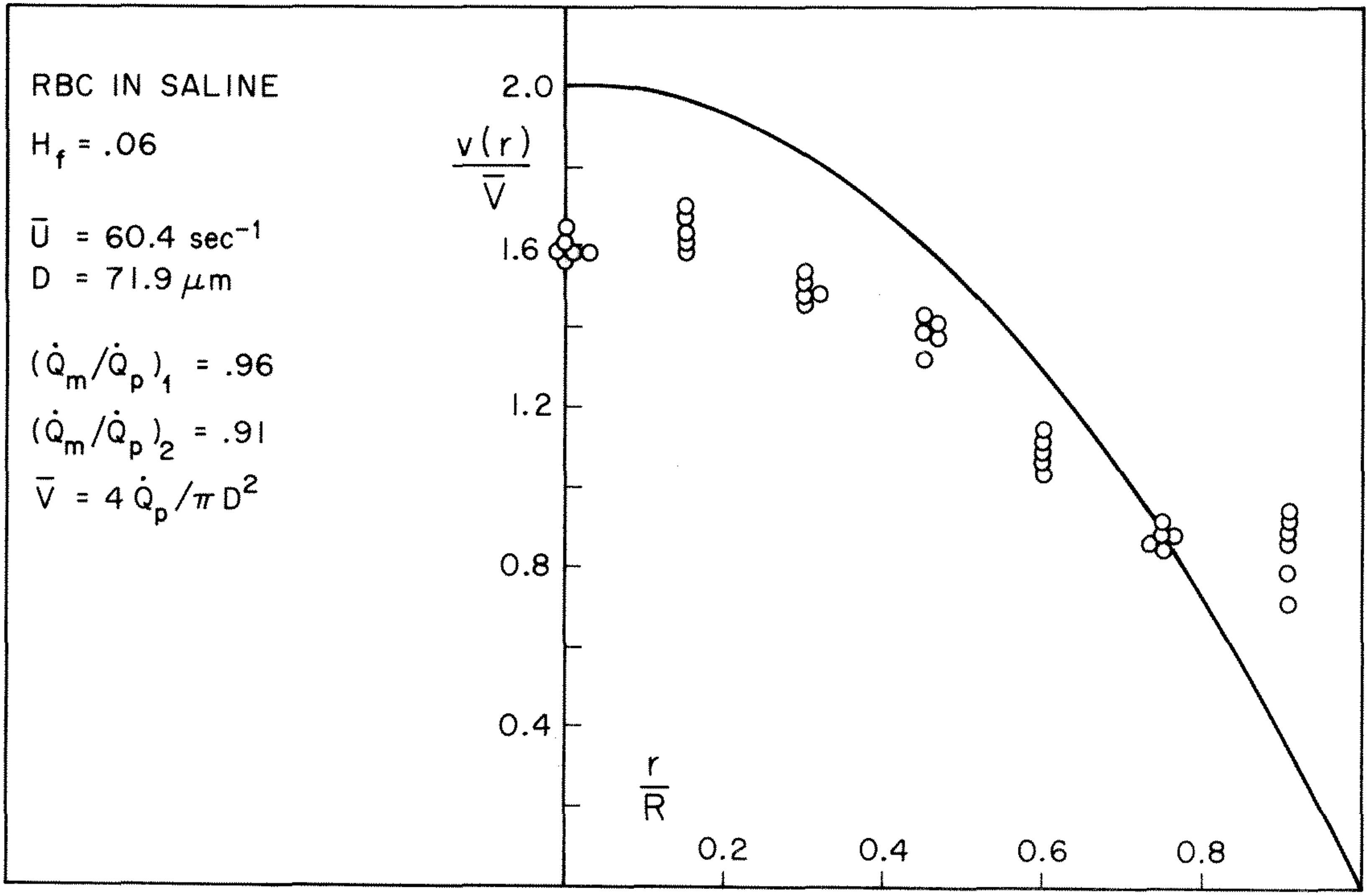

Figure 19 Double-Slit Velocity Profile.

considered was that the depth of field of the microscope objective was too large. If this depth above and below the plane of focus in which objects appear in sharp focus is not small in comparison to the tube diameter, a range of velocities will be averaged in each reading. This averaging could result in the blunt profiles. The depth of field of the 50x/.60 objective used, is about 3μm. In order to reduce this depth to the smallest available value the lens system was changed to include an oil-immersion, 100x/1.30 objective. (The horizontal mounting of the microscope made a special immersion oil necessary to prevent the oil from running away. Thixotropic immersion oil was obtained from Cargille Scientific Inc.) This new lens system, which has a depth of field of less than 1/2μm, was used to measure profiles. The results were identical to previously measured profiles leaving the distortion question still unanswered.

Since the new lens system did produce a much sharper image, it was used for the rest of the measurements.

Optical Correction Calculations

The optical correction calculations were next examined in search of a source of the errors. The radial position of the measured velocities has to be corrected before plotting because of the distortion in position caused by the two curved interfaces at the inside and outside wall of the tube. The corrections were made by geometrical optics; rays of light were followed as they were bent by refraction at each of the interfaces. An apparent image position was calculated for each object position. (Sample calculations can be found in Appendix C). For these calculations, the indices of refraction of blood and plasma were measured in a refractometer and that for the tube material was measured by comparison with index of refraction liquids from Cargille Scientific.

Material	Index of Refraction at 25°C
plasma	1.3474 ± .0002
blood with at least 5% broken cells	1.3474
glass used for thin-walled tubes	1.472 ± .004

In order to check these calculations experimentally a piece of the capillary tubing was ground to the diametral plane. A reticle was placed behind the half tube so that a reticle line was located at the diametral plane and was positioned at an angle of about 60° with the axis of the tube. The half tube was filled with the liquid for which the corresponding calculation was made. When the reticle line was viewed under the microscope through the curved glass surface, it appeared distorted; this distortion was photographed through the microscope. On a separate sheet of paper, a line was drawn at the same angle as the reticle line with the tube axis; the distortions of this line, that were predicted by the optical distortion calculations, were then plotted. The photographed line was projected from the film onto this plot (Plot is shown in Figure 20). The calculated and observed distorted line coincided exactly, confirming experimentally the optical corrections used.

Figure 21 shows the distortion of position of objects within the tube. The dotted line represents the object points for image points along the diametral plane; when the focal plane is positioned through the

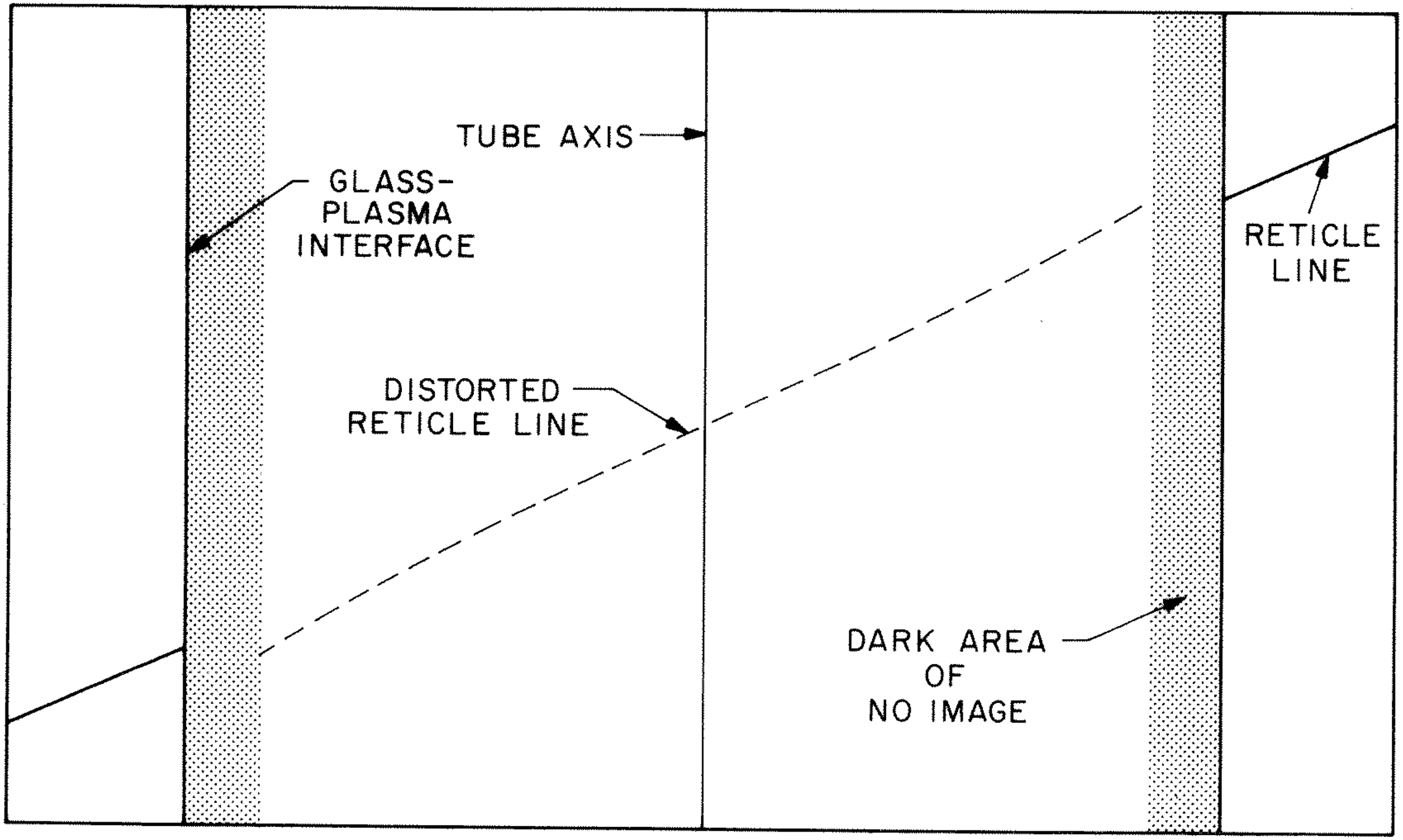

Figure 20 Plot of Distortion of Reticle Line Caused by Curved Interface Between Glass and Plasma.

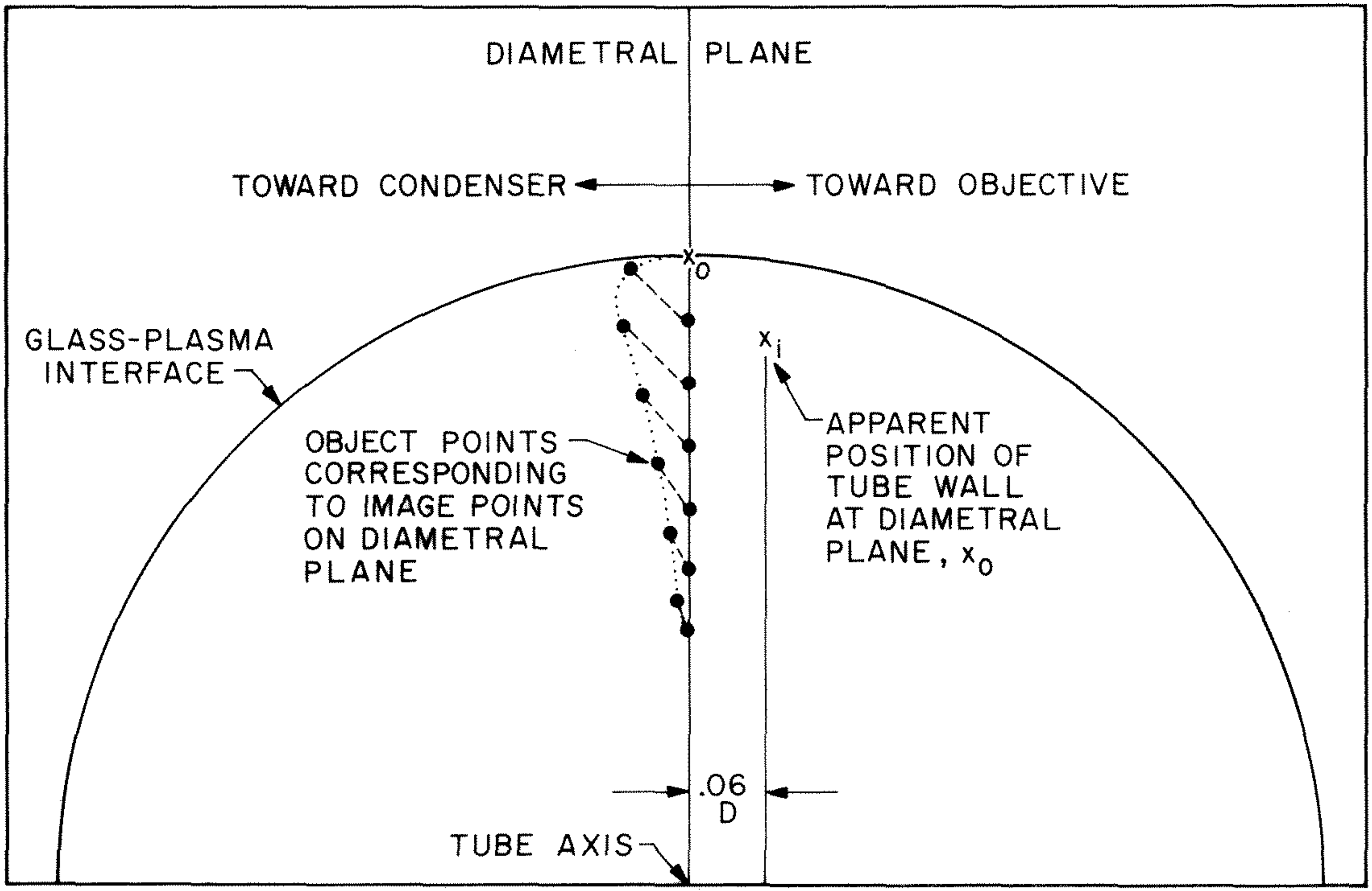

Figure 21 Distortion of Positions of Objects Within the Tube.

diameter, the actual points from which velocities are measured are along the dotted line. Also shown is the location of the image point which corresponds to an object point on the diametral plane at the tube wall; when the focal plane is positioned through the point marked x_i, the tube wall at the diametral plane, point x_0, is in focus.

Position of Focus

This investigation of optical distortions brought out another possible explanation of the velocity profile discrepancies. If the focal position is off the diameter, low profiles would be measured. This error in focusing could easily have occurred because the optical distortions make the location of the diametral plane difficult. As the plane of focus is moved, the image which is observed changes in width. The widest image is often mistaken as the image at the diametral plane. However, the widest image actually occurs approximately 1/2 tube radius in front of this plane. Figure 22 shows a plot of the width ω_n of the image for a focal plane position a distance of ℓ_n in front of or behind the diametral plane. The dotted line represents apparent positions of the tube wall for different planes of focus. The area between the apparent wall position and the actual wall position is a region of no image. For this reason a wide dark line is observed at each side of the image of flowing blood.

For the purpose of establishing some guidelines for the location of the correct position of focus, the tube image was observed at different focal positions. A microscope with a calibrated focus mechanism

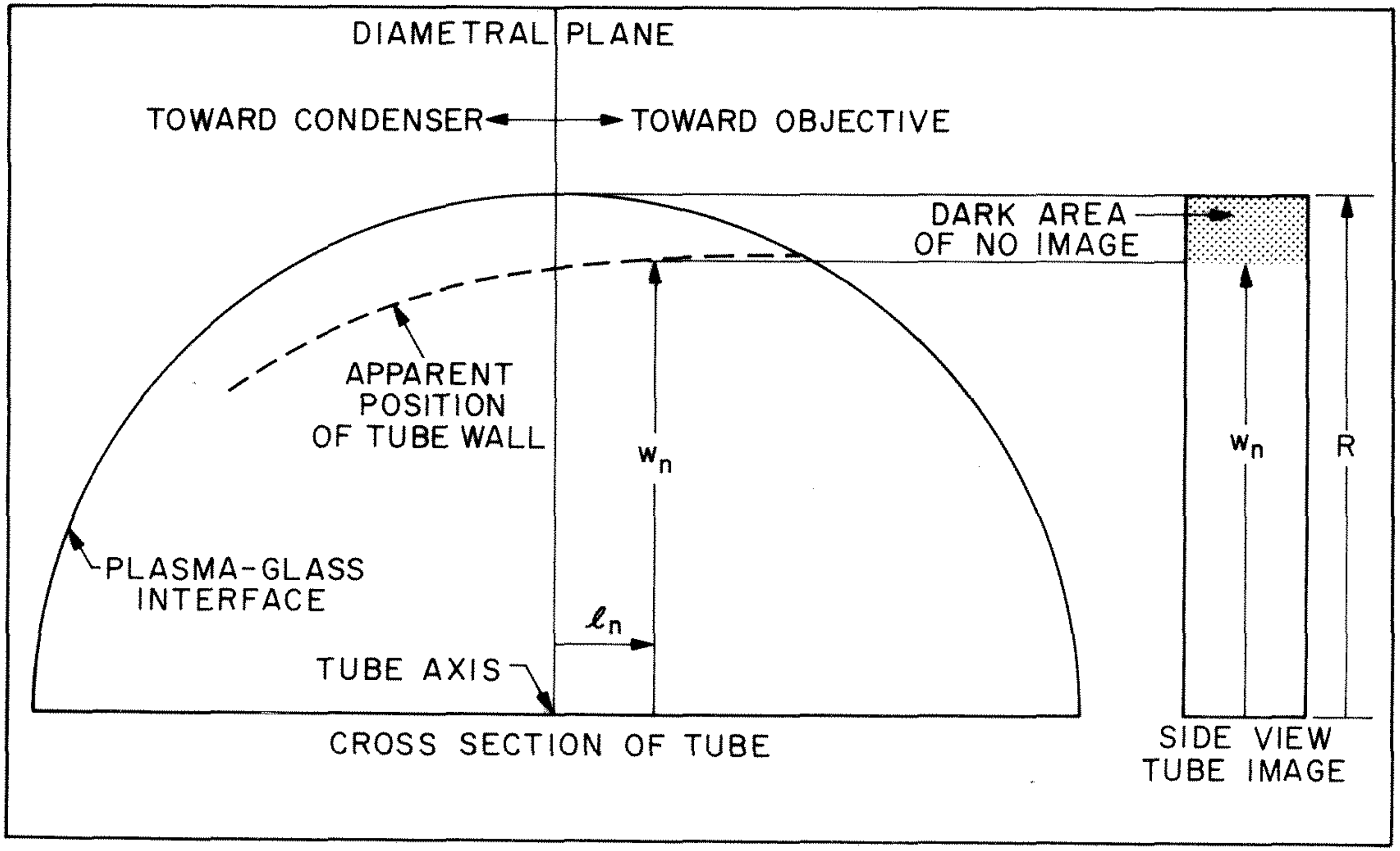

Figure 22 Width, w_n, of the Image for Focal Plane Position a Distance ℓ_n from Diametral Plane.

accurate to less than 1 μm was used to keep track of the distances between the focal positions observed. These different images were then compared with the patterns predicted for different planes of focus by the optical distortion calculations. Through this comparison one particular observed image pattern was identified and located. This pattern is a distinct bright line appearing just inside the black region along each side of the image of blood. The light reflected from the interface between the blood and the tube wall provides an explanation of this bright line. The light from the interface will be by far the brightest at the diametral plane; it is at this plane that the largest part of the cone of light delivered by the condenser is reflected at an angle which will allow it to enter the microscope objective. (This can be seen from Figure 23 where cones of light are drawn at different points along the interface. The unshaded area of each cone shows the portion of the light which is delivered by the condenser and which will be reflected at an angle such that it will enter the objective. The unshaded area is a maximum at the diametral plane.) Therefore, the location of the object points producing the observed bright line is the intersection of the diametral plane with the tube wall. The optical distortion calculations show the apparent image position of these object points to be in front of the diametral plane by about (.06) x (tube diameter). This image point is marked x_i in Figures 21 and 23. The focus can be accurately positioned at the diametral plane by focusing on the bright line and then moving .06D toward the back wall of the tube. The bright line makes a good reference location because it is an easy object on which to focus.

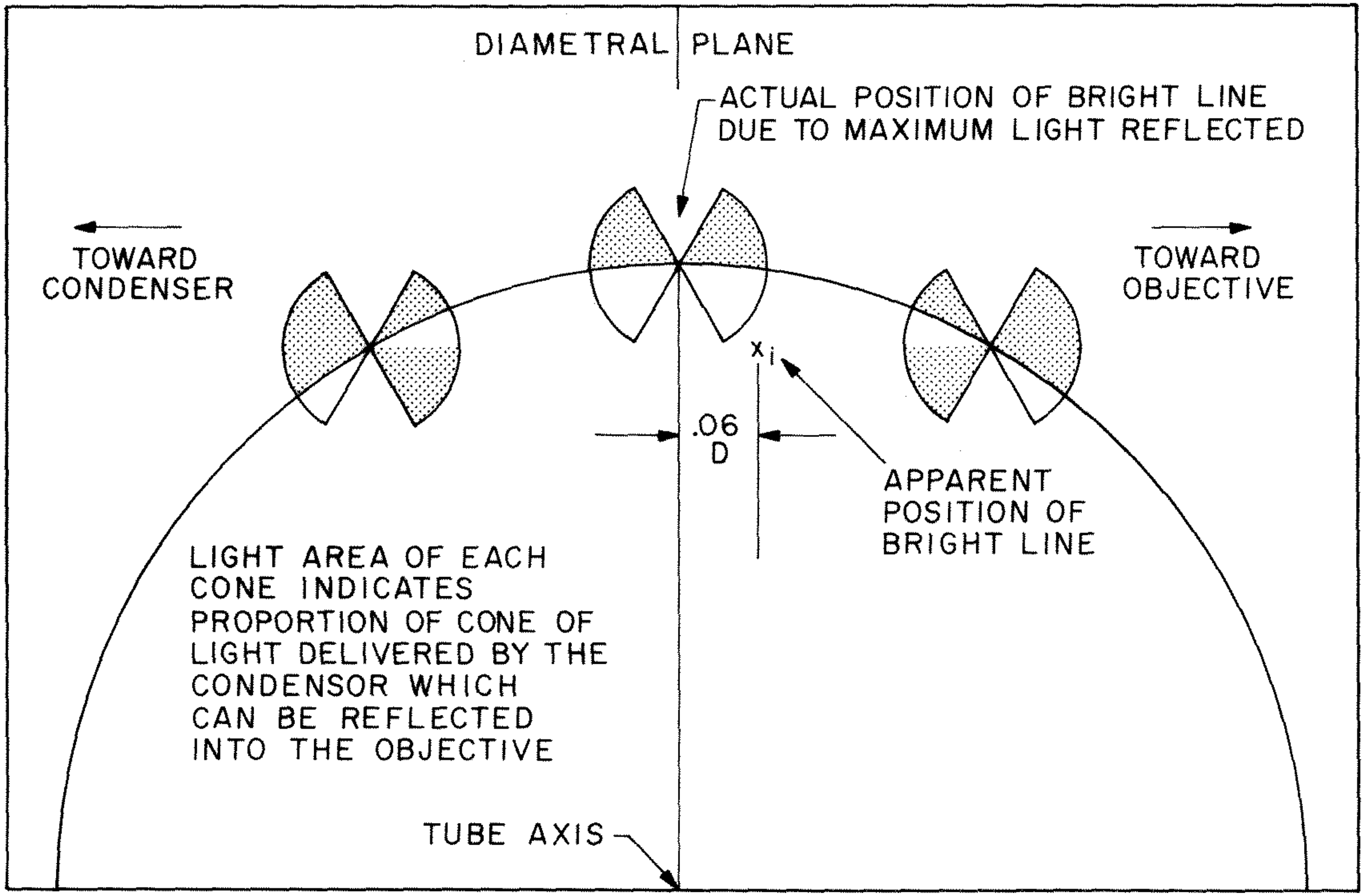

Figure 23 Explanation and Locations of Bright Line Appearing at Each Side of Tube Image.

There are other possible but less distinct reference positions such as the front and back tube walls (wall closest and farthest from microscope objective respectively). Locating these positions using the bright line as a reference provided a check of the bright line focus method.

Profiles were measured with this new confidence in focal position. There were no differences between these results and previous profiles.

Chromatic Distortions

A further optical distortion considered was that due to the different wave lengths of light present in the light source. The lenses used were made to focus, without chromatic aberrations, only those wave lengths of light in the visible range. The mercury arc lamp produces some light in the infrared region; also, the phototransistors have high sensitivity in this region. If light beyond the visible were focused at a different position than the visible light, signals from different layers of blood would be averaged with unknown weighting. With the use of $CuSO_4$ solution as an infrared filter and an additional standard gelatin filter (57A), monochromatic light in the visible range was obtained. Velocities measured with and without these filters were identical.

Analysis of Photometric Signals

Since the optical image seemed to be well understood the analysis of the photometric signals was next re-examined.

There are two slightly different principles on which methods of analyzing the double-slit signals are based. One is the determination of the time shift which gives the maximum crosscorrelation of the signals. This maximization of correlation has been carried out through the use of a digital computer after A/D conversion and by commercial correlators which handle analog data. The second principle is the measurement of time between prominent events appearing in each of the two signals. This is the basis for hand analysis of signals spread out on paper and the Elmore analog analyzer. The difference in the two principles is that one uses only the prominent events and the other uses the whole signal. This difference could mean different information is being extracted from the signals.

A preliminary check had already shown that the Elmore analyzer gave results consistent with those from hand analysis and digital computer crosscorrelation. As an additional check, tapes were made of signals for profiles for a range of $\overline{U}$ and hematocrit. The same data were then analyzed through the Elmore analyzer and a Hewlett Packard crosscorrelator. The resulting profiles were the same. In Figure 24 one of the profiles is shown with results from both methods plotted together. Later a Saicor correlator became available and the same data were checked again. Even though this machine works in a somewhat different way than the Hewlett Packard correlator, the profiles it produced were again the same.

There seems to be no measurable difference in results between the two different principles of analysis of the double-slit signals. From

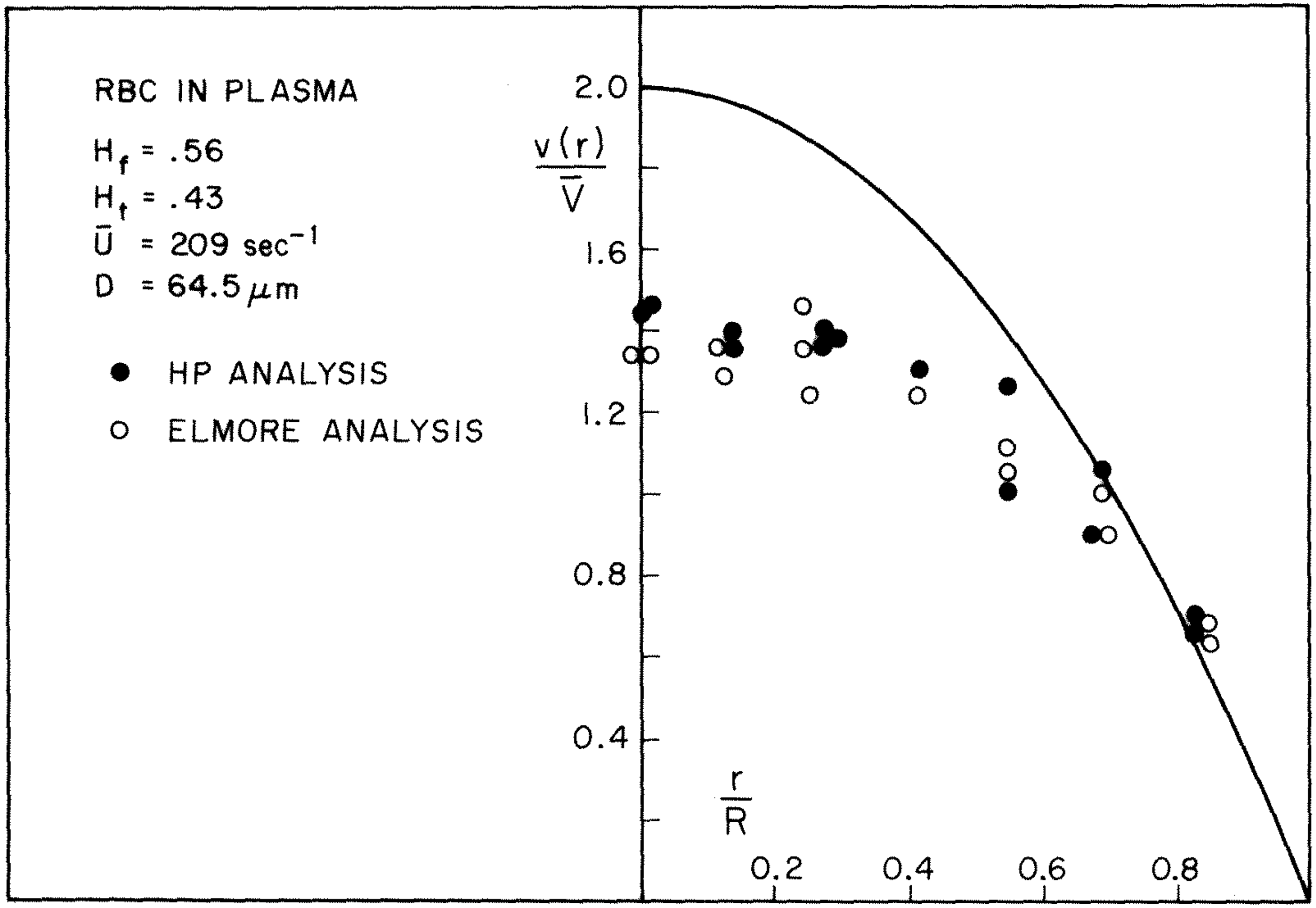

Figure 24 Comparison of Results from Two Different Principles of Analysis.

all indications, the Elmore analyzer extracts the same information as crosscorrelation of the signals.

Motion Picture Profiles

Since no distortion in the double-slit method was uncovered, motion picture apparatus was set up to check the double-slit profiles. Because of its limited range of $\overline{U}$, hematocrit, and tube size, and because of the tedious analysis involved, the motion picture technique could not be used to replace the double-slit method. However, for dilute suspensions it serves as a good check on the double-slit results. A Milliken pin-registered motion picture camera was mounted in place of the phototransistor screen and a Chadwick-Helmuth Strobex xenon flashlamp, synchronized with the camera, was used in place of the mercury arc lamp. Motion pictures of the flow of dilute red cell suspensions were taken; velocity profiles were constructed by measuring motion of red cells from frame to frame using a Traid Viewer. The importance of the position of focus and of the shallow depth of field were evident in these films. For the 100x/1.30 objective, the depth of field was clearly less than a red cell thickness.

A profile is shown in Figure 25 for 6% red cells in saline. For the first time the parabola that was expected for this dilute suspension was measured. The velocities from the films fall quite close to the parabola of the pump volume flow rate. These films indicate that the double-slit method must distort results.

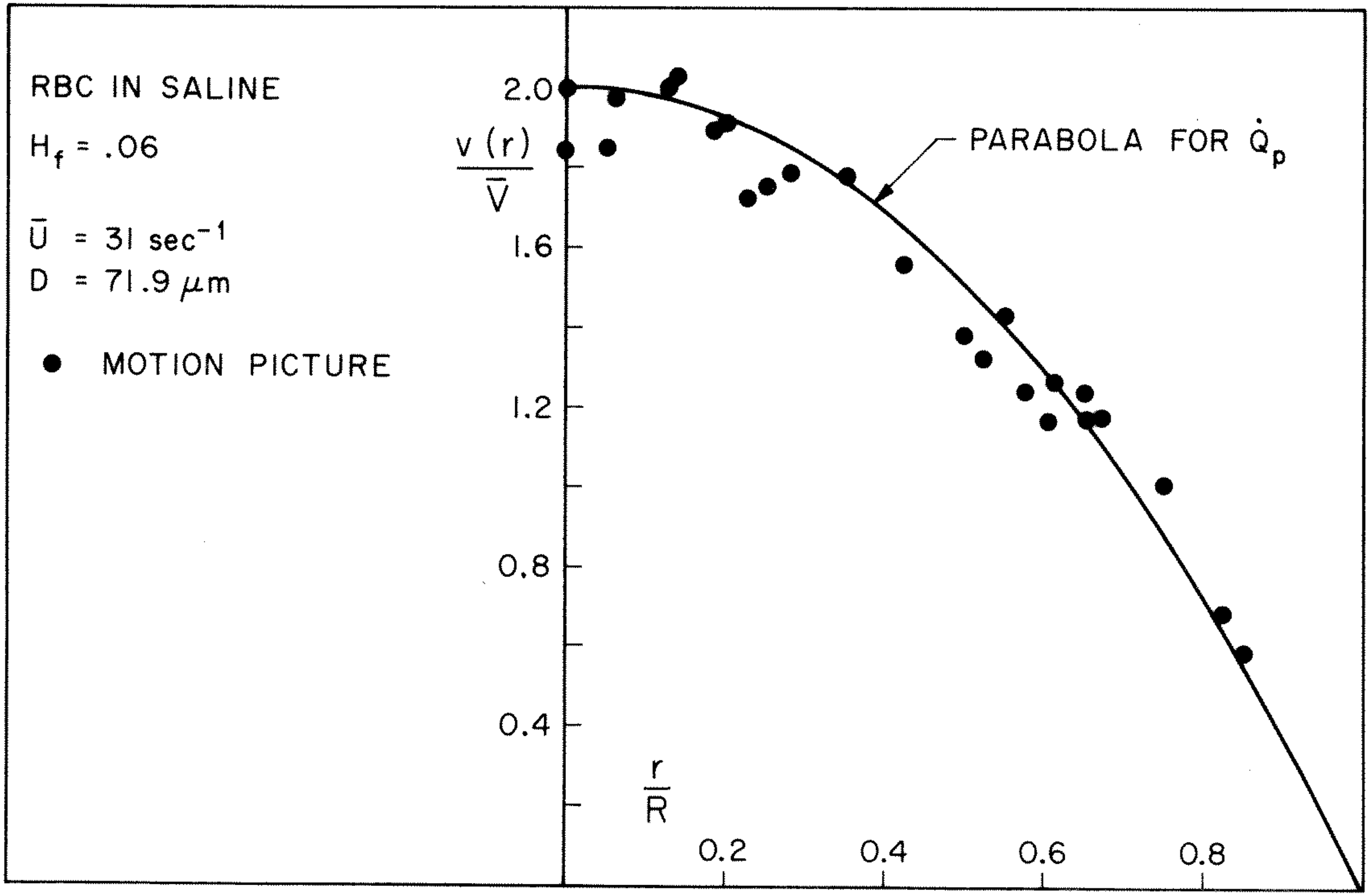

Figure 25 Motion Picture Profile.

Focus-through Profiles

Can the distortion of the double-slit technique be demonstrated more decisively? The basic assumption on which the method was extended from capillaries to the measurement of velocity profiles was that data could be taken from a shallow region roughly equal in depth to the depth of field of the microscope. If this is true, a profile can be taken not only by moving across the image of the tube perpendicular to the optic axis but also by moving the plane of focus from the front wall of the tube (closest to the microscope objective) to the back wall (closest to the condenser). Profiles taken in these two ways should be identical if the assumption is valid.

For a full range of hematocrits, profiles were measured across and through the tube and plotted together. Figures 26 and 27 show that the profiles measured in these two ways certainly are not identical. The focus-through profiles are straight lines; the same velocity reading results from any focal position.

These results indicate that the phototransistor signals contain modulations for cell motion throughout the tube and not just from the plane of focus. Crosscorrelation of the signals must average all events in some way. Several alternative analysis techniques were tried in an effort to pick out from the signals those events which occurred in the plane of focus. First the signals were hand analyzed by choosing only the very sharpest modulations in the signals. This procedure produced the same profile shapes as before. Then attempts were made to electrically select the sharpest events in the signals or the highest velocities

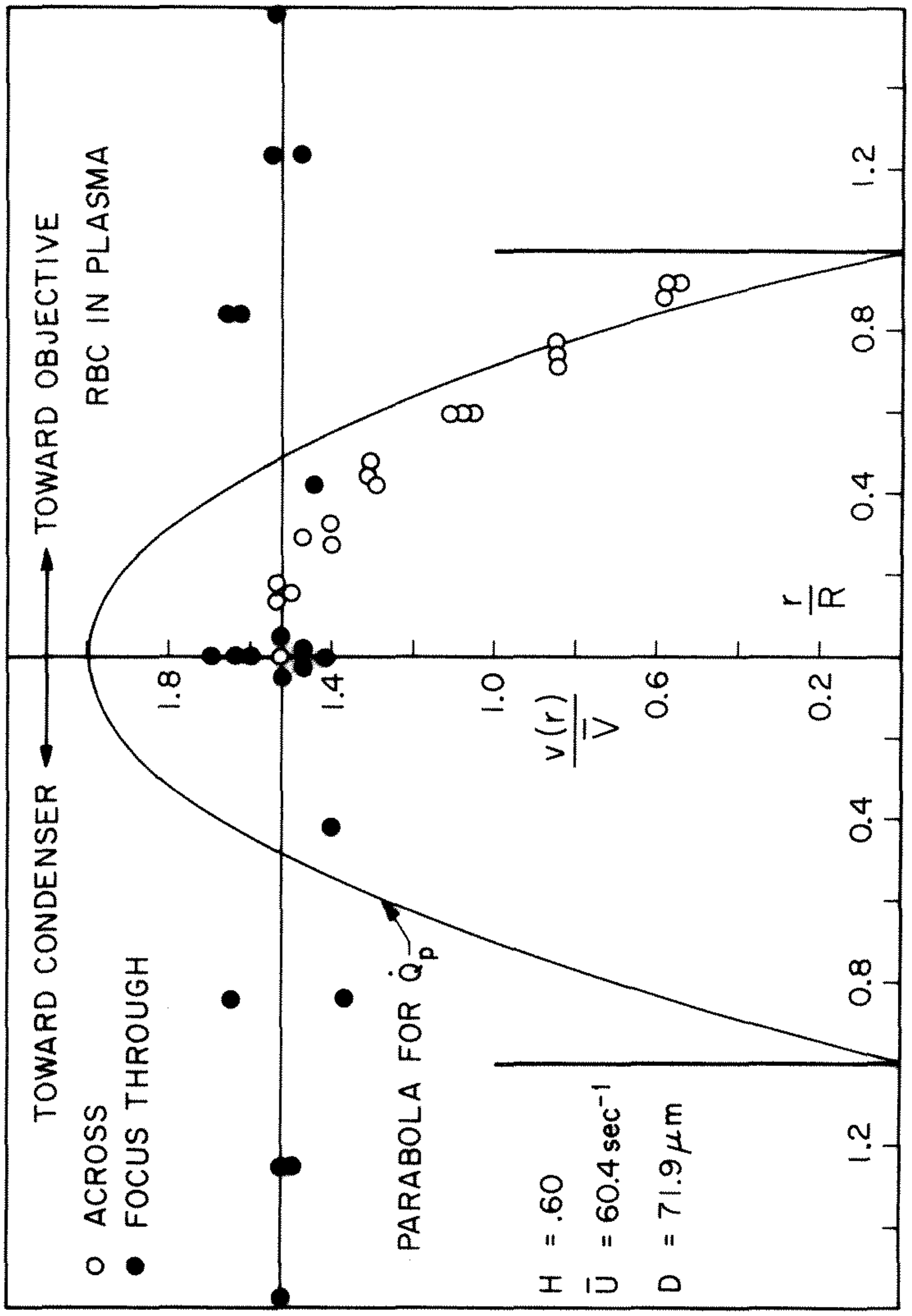

Figure 26 Profiles Measured Across and Through at High Hematocrit.

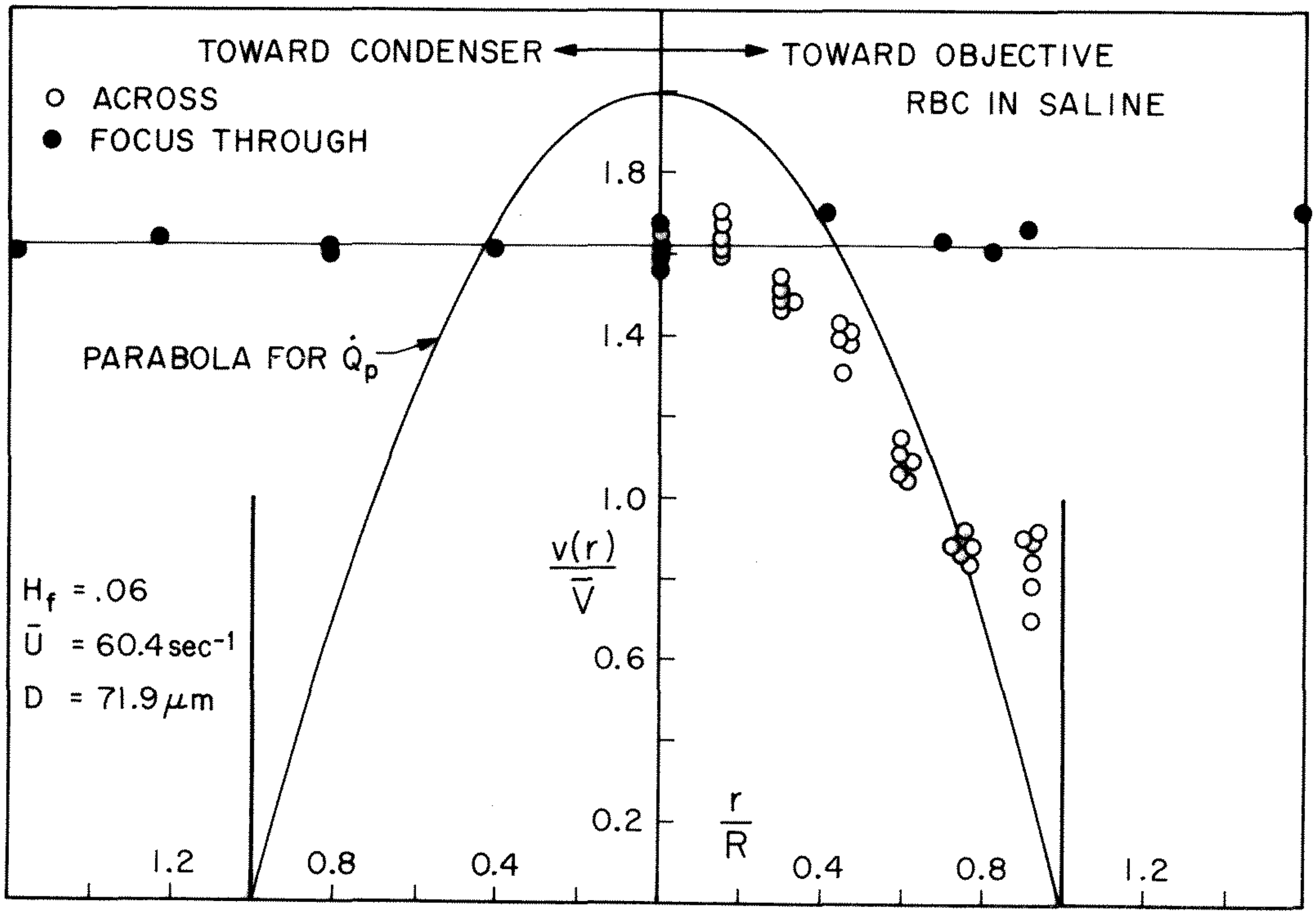

Figure 27 Profiles Measured Across and Through at Low Hematocrit.

or the shortest delays. Still the same profile shapes resulted. Some of these techniques raised the level of the whole profile but none of them produced any shape changes.

Comparison With the Single-Slit Technique

As a further possibility of selecting the highest velocities, and therefore the velocity profile, from all the modulations present in the photometric signals, the single-slit technique of Wiederhielm(58) was investigated. Wiederhielm showed that the upper limit of the frequency spectrum of the modulations in a single photosensor signal is linearly related to the velocity of cells causing the modulations. This is the basis for his method which will be referred to here as the single-slit technique. Since this technique is designed to select the highest frequency, there was a possibility that it could sort out the highest velocities.

For this reason, single-slit analysis equipment was built in this laboratory. Comparison of the results from taped data analyzed by both double-slit and single-slit methods indicate the same shape profiles. The calibration of the single-slit changed for different magnifications, hematocrits, and focus positions. Therefore only a qualitative comparison between the methods was made. However, the fact that the phototransistor signals contain modulation from cell motion throughout the tube seems to distort the velocity profiles measured by the single-slit technique also.

Conclusions on Measured Profiles

The very blunt profiles reported from double-slit measurements (27, 28, 29) have been shown to be an artifact of the measuring instrument. The actual profile shapes are still not known. Not even the relationship between centerline velocity and volume flow rate is known for every tube size. Because flow rate is the most important single parameter in the physiological measurements and because the double-slit technique is already in use by physiologists, the double-slit investigation was continued. The goals of this continuation were to determine what function of tube velocities the double-slit technique actually does measure and what can be inferred from these measurements about the actual profile shapes.

VI. AVERAGING MODEL

Reasons for Model

If the relationship between the actual velocities and the double-slit results can be well represented by a simple mathematical model, the true profiles can perhaps still be determined from double-slit measurements. Constructing this model would be an unreasonable task if the focus-through profiles showed only a shape which disagreed with the profiles taken across the tube image. However, the fact that focusing through the tube gives a constant velocity reading provides some basis for a model. The simplest explanation of this totally flat profile is that the measuring system picks up all events occurring in the tube (along a line through the sensor and parallel to the optic axis) without preference to those events in focus. If this explanation is assumed true, and, in addition, the particle concentration is assumed to be nearly uniform, an averaging model can be constructed.

Construction of Model

Consider the tube of flowing blood as a series of concentric cylinders of thickness Δr located at a distance r from the tube axis and moving along the tube axis with a velocity v(r). A phototransistor capable of sensing all events along a line parallel to the optic axis will then see a series of laminae of moving cells. Each lamina will contribute modulations in the light intensity corresponding to the velocity at which it is moving. As long as the concentration in each lamina is approximately the same, the frequency with which each lamina contributes signals will be proportional to the velocity of the lamina. When the phototransistor signals are analyzed by crosscorrelation or equivalent means, all these contributions of velocities are averaged. The resulting reading, $v_{ave}(x)$, for a pair of phototransistors located at a distance x on the tube image from the tube axis, can be represented by the following expression.

$$v_{ave}(x) = \frac{\int_0^{\sqrt{R^2 - x^2}} v^2(r)\, dy}{\int_0^{\sqrt{R^2 - x^2}} v(r)\, dy} \qquad (10)$$

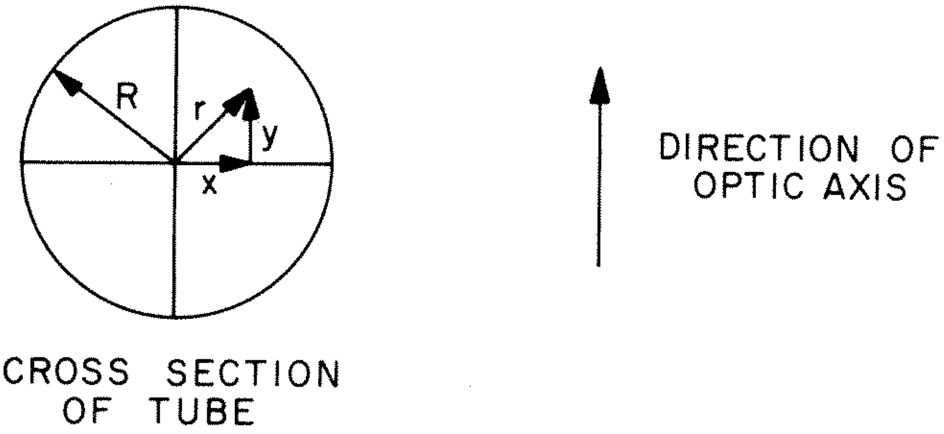

Thus the velocity of each lamina is weighted with itself in the average because of the relative frequency at which it contributes signals.

If wall exclusion of cells is to be taken into account, the upper limit of integration in equation (10) should be changed to $\sqrt{(R-\delta)^2 - x^2}$

where δ is the thickness of the cell-free layer at the wall. Reasonable values for δ are 2-4 micra. For values in this range and tube sizes used in this study, the exact value of δ is not very important in the determination of v_{ave} because $v(r)$ is very small near the tube wall.

An additional consideration in the averaging of equation (10) is that the actual path along which velocities are averaged is not parallel to the optic axis because of optical distortions. The line of image points parallel to the optic axis corresponds to a line of object points inclined to the optic axis. However, when this distortion was calculated, the velocities along the image line were very nearly the same as the velocities along the object line. Therefore, equation (10) was not changed because of this distortion.

This model explains the low value of centerline velocity that occurs in all the measured profiles. If a parabolic velocity distribution, $v(r) = V_{max}(1-(r/R)^2)$ is averaged using equation (10), the result is another parabolic distribution with centerline velocity equal to $.8V_{max}$. For almost all the profiles measured the centerline velocity is just .8 times the value expected for a parabola of correct volume flow rate.

Averaging by equation (10) does not however explain the whole profile shape. It does not predict the high velocity measured near the wall. In order to explain the whole profile it is necessary to put into the model the effect of the finite size of red cells and sensors. It can be seen from Figure 28 that cells centered some distance from a photosensor will cause modulations in that sensor's output. These modulations will occur at a relative frequency proportional to the cell

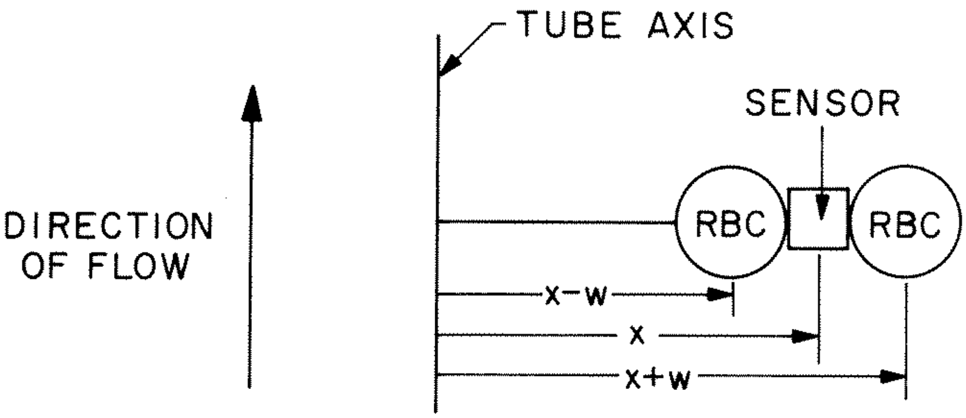

Figure 28

velocity. Thus there is also weighted averaging of velocities across a phototransistor perpendicular to the optic axis. This consideration changes the expression for $v_{ave}(x)$ to the following:

$$v_{ave}(x) = \frac{\int_{x-w}^{x+w} \int_{0}^{\sqrt{(R-\delta)^2 - x'^2}} v^2(r)\, dy\, dx'}{\int_{x-w}^{x+w} \int_{0}^{\sqrt{(R-\delta)^2 - x'^2}} v(r)\, dy\, dx'} \; . \qquad (11)$$

The width w over which velocities are averaged should be approximately one red cell radius plus 1/2 the width of the active area of a phototransistor. The red cell radius will always be 1-4μm depending on cell orientation, but the effective width of the phototransistor will vary for different magnifications. The expression for w that was used was

$$w = 4\mu m + \frac{1.25 \times 10^3}{\text{magnification}} \mu m \, .$$

Unless another magnification is indicated, profiles presented here were measured with the array just spanning the tube radius; therefore, the effective sensor width is proportional to tube radius and an approximate expression for the w used is

$$w \approx 4\mu m + \frac{R}{14} .$$

Comparison of Model with Experiment

In order to compare the model with experimental results, equation (11) was used to average parabolic velocity distributions. The resulting averaged profiles were compared with measured results from flow situations in which the velocity profile could be expected to be a parabola. The data presented in Figure 19 were from the same flow situation for which the motion picture analysis produced a parabolic distribution. This profile is shown again in Figure 29 where the dotted line represents a parabolic v(r) averaged by equation (11) to give $v_{ave}(x)$. The averaged parabola fits the measured profile quite well.

The averaging model predicts a change in profile shape with tube size even if the actual profile remains parabolic. This prediction was used as a further check of the model. Tubes were constructed of diameters from 27 to 200μm. Profiles were measured in these tubes with very low concentration of red cells in saline at high $\overline{U}$ for which the profiles would be expected to be nearly parabolic. From equation (11), parabolic profiles were averaged and plotted with the measured profiles. Some of these plots are shown in Figures 30 to 33. For tubes above 100μm in diameter the profile shapes are constant because the

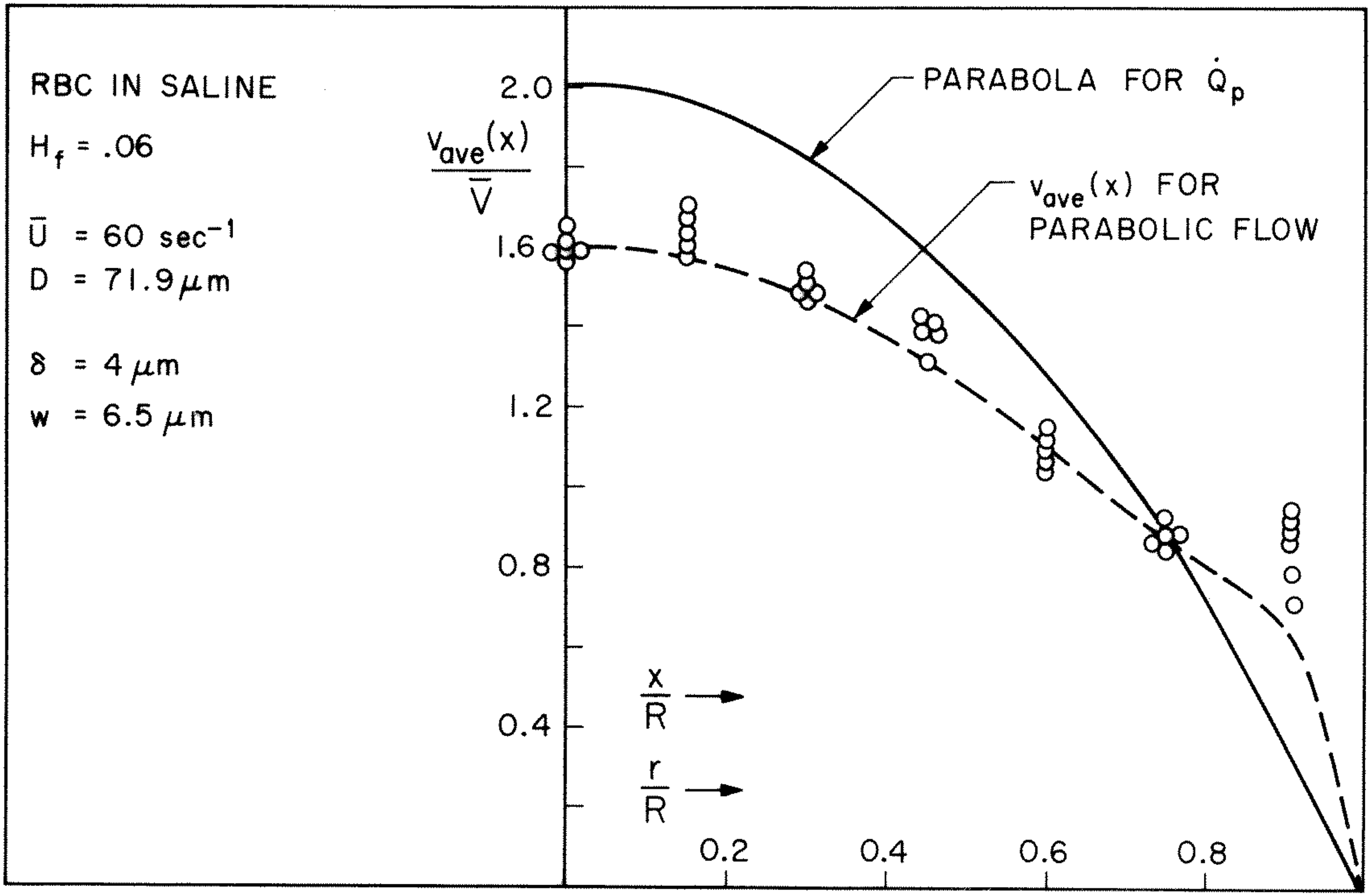

Figure 29 Averaged Parabolic Flow.

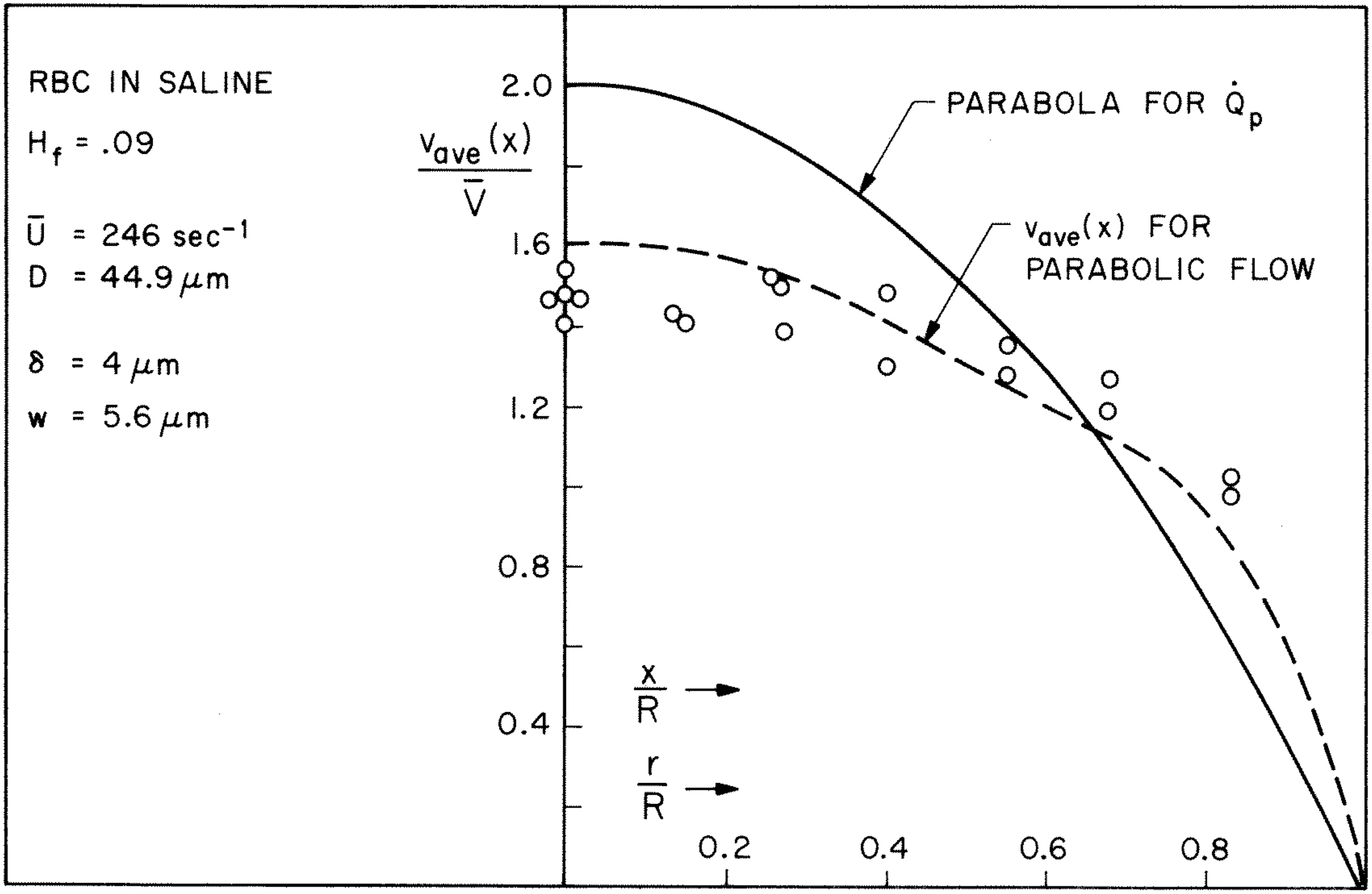

Figure 30 Averaged Parabolic Flow.

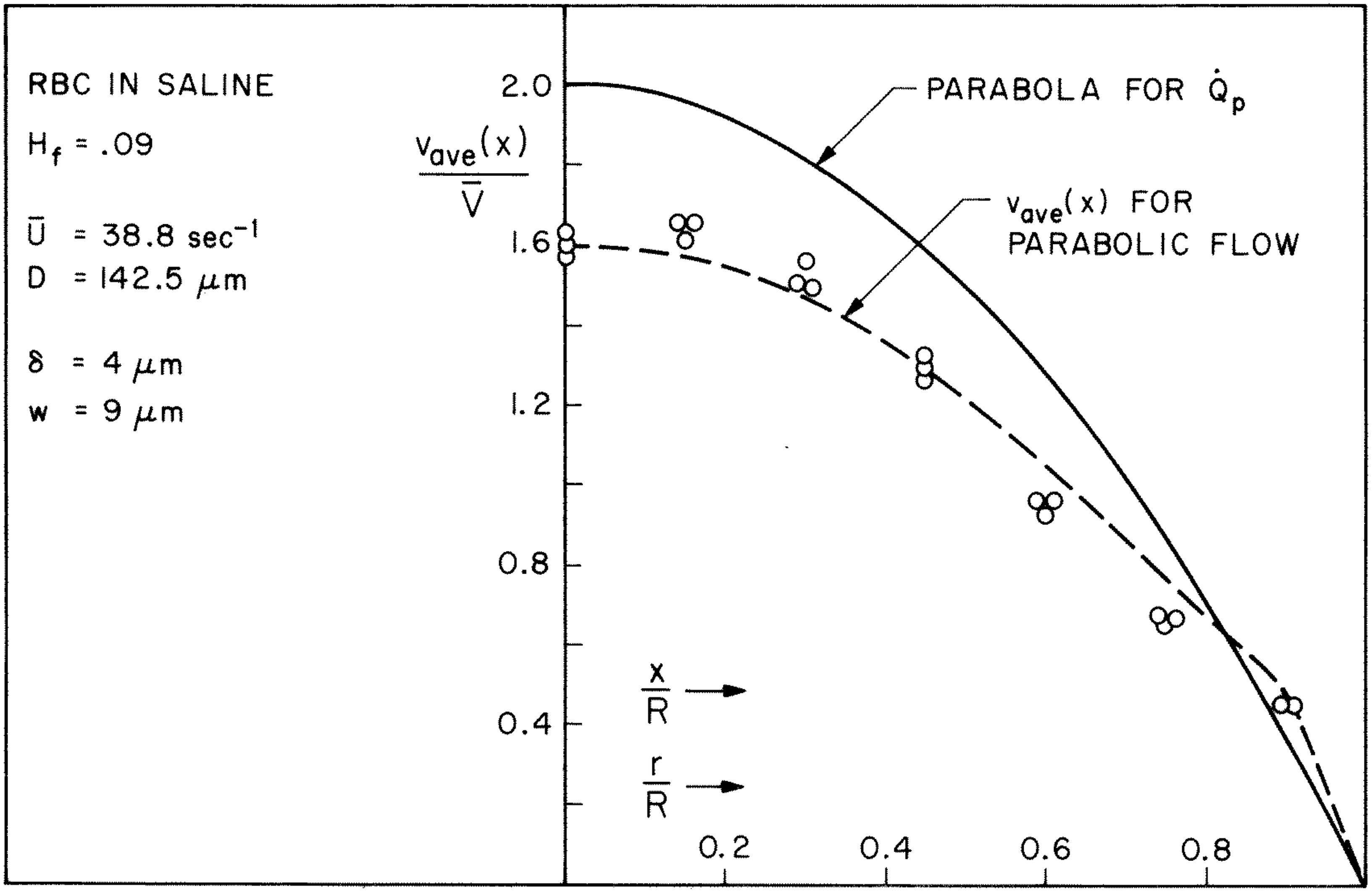

Figure 31 Averaged Parabolic Flow.

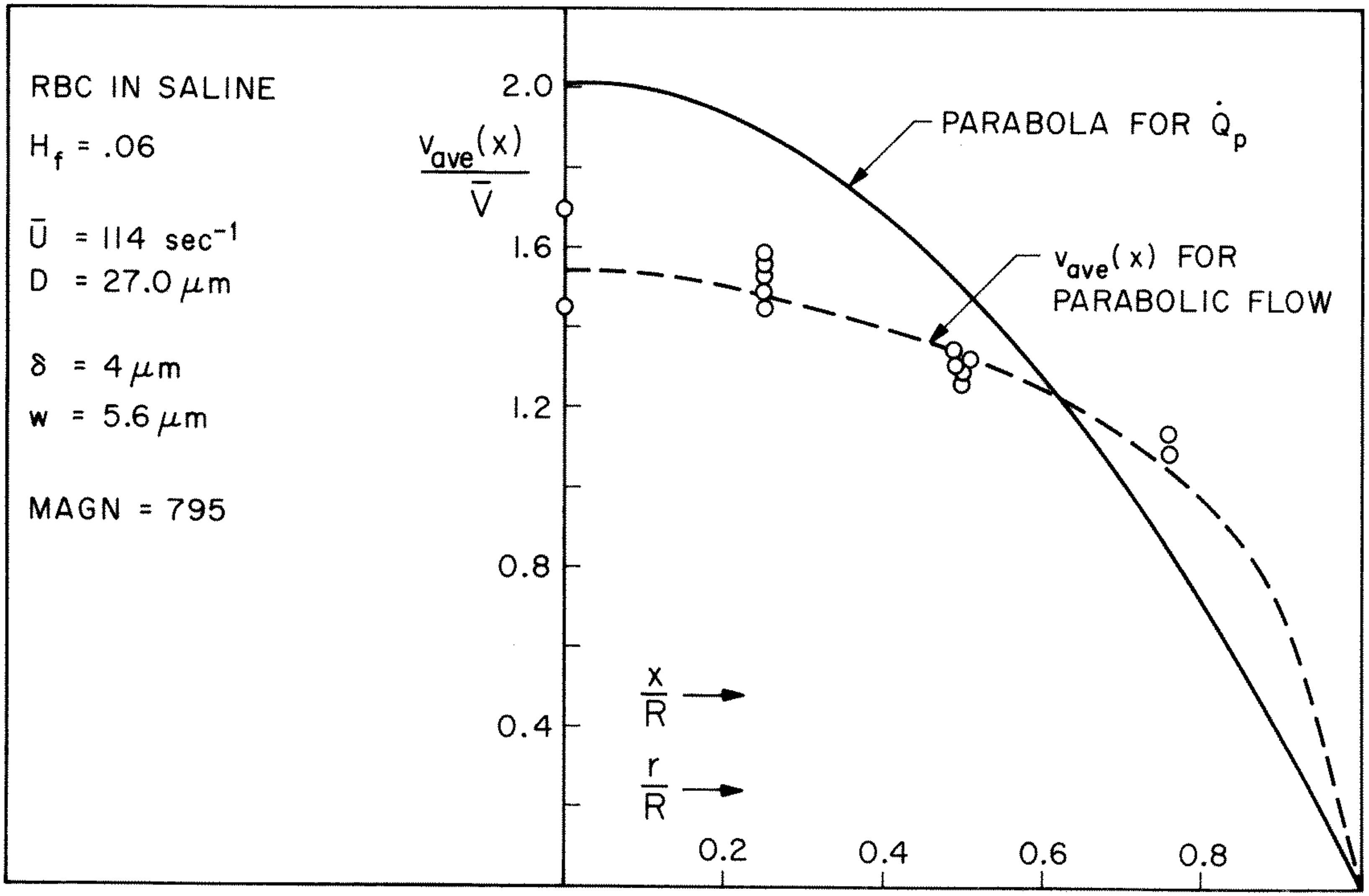

Figure 32 Averaged Parabolic Flow.

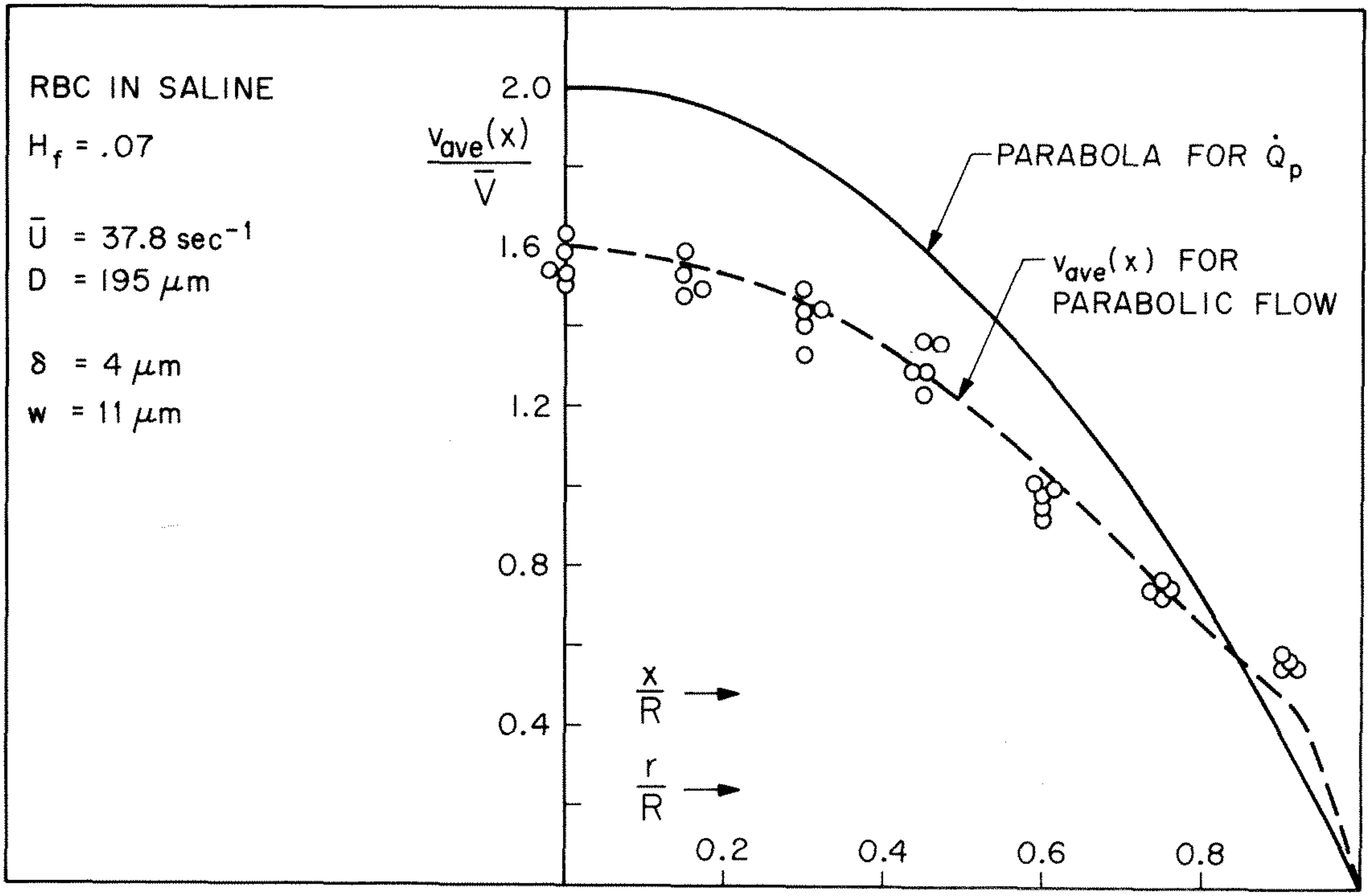

Figure 33 Averaged Parabolic Flow.

effect of red cell radius becomes negligible and the averaging width w becomes the photosensor width which is always the same proportion of the tube diameter. Below 100μm tube diameter, the red cell size is the main determinant of the averaging width and the profile shapes become quite blunt as the red cell size becomes large with respect to the tube diameter.

Measurements in these additional tube sizes provided support in another way for ideas behind the averaging model. High $\overline{U}$ data were also taken in these tubes for high hematocrits. Focus-through profiles were measured at both high and low hematocrits. For tubes under 100μm in diameter, the results were the same as previous results; that is, the focus-through profiles were flat and the high hematocrit profiles coincided with the low hematocrit profiles. In tubes above 100μm the focus-through profiles were flat only for low hematocrit. At high hematocrit in these large tubes, velocity readings changed with focus and the profiles measured across the tube were above the low concentration profiles. As the tube size was increased, the high hematocrit profiles became higher and sharper. At 140 and 200μm, a nearly parabolic profile of the correct volume flow rate was measured for high hematocrits. The only deviation from a parabola was a slightly high velocity near the wall. This behavior is demonstrated in Figures 34 and 35. Apparently at these large tube sizes and concentrations, the whole tube is not visible to the phototransistor and the layer of cells which contributes velocities becomes small compared to tube diameter. The only averaging present here is that across a sensor, perpendicular to the optic axis.

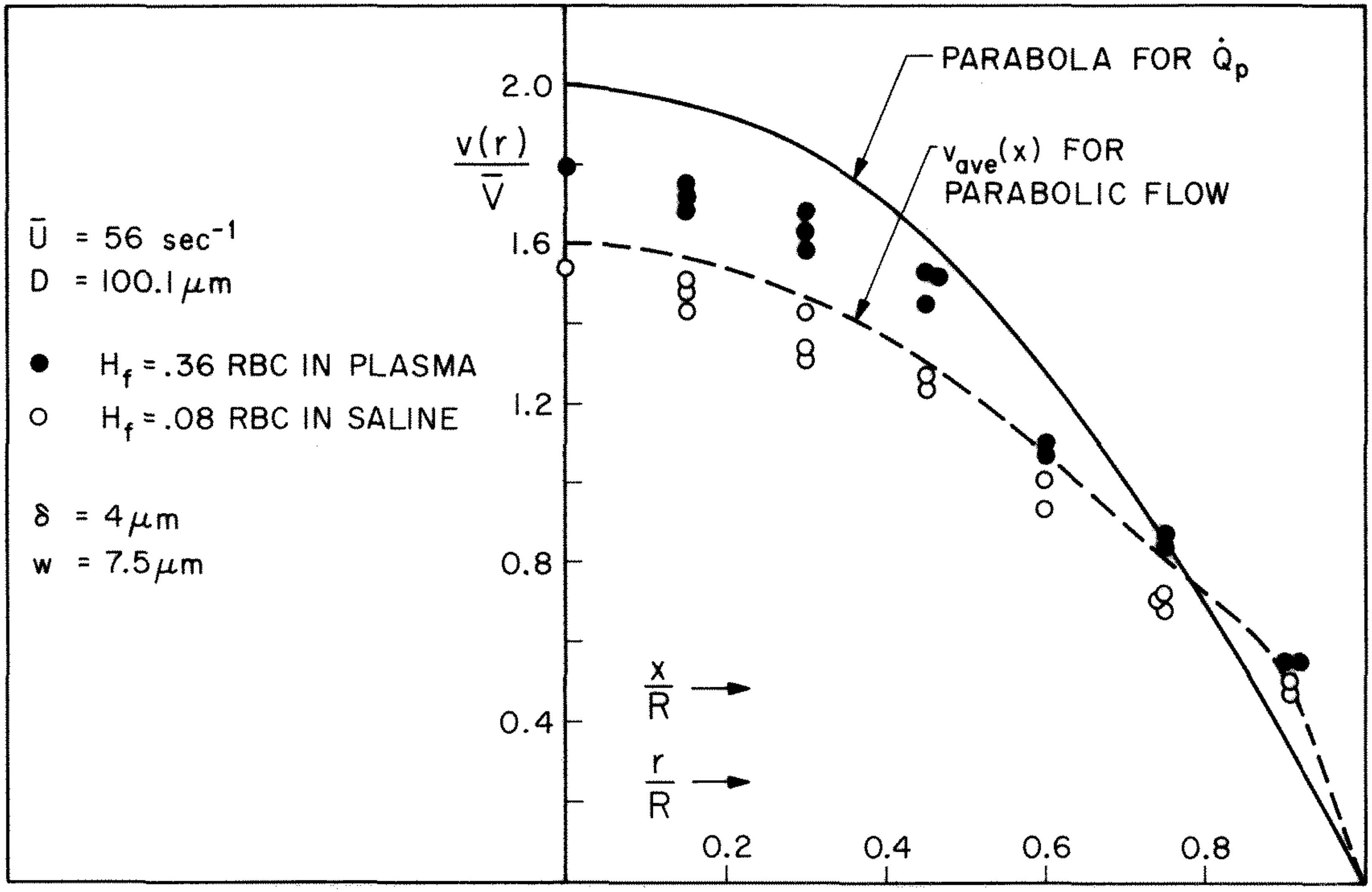

Figure 34 Large Tube Double-Slit Profiles.

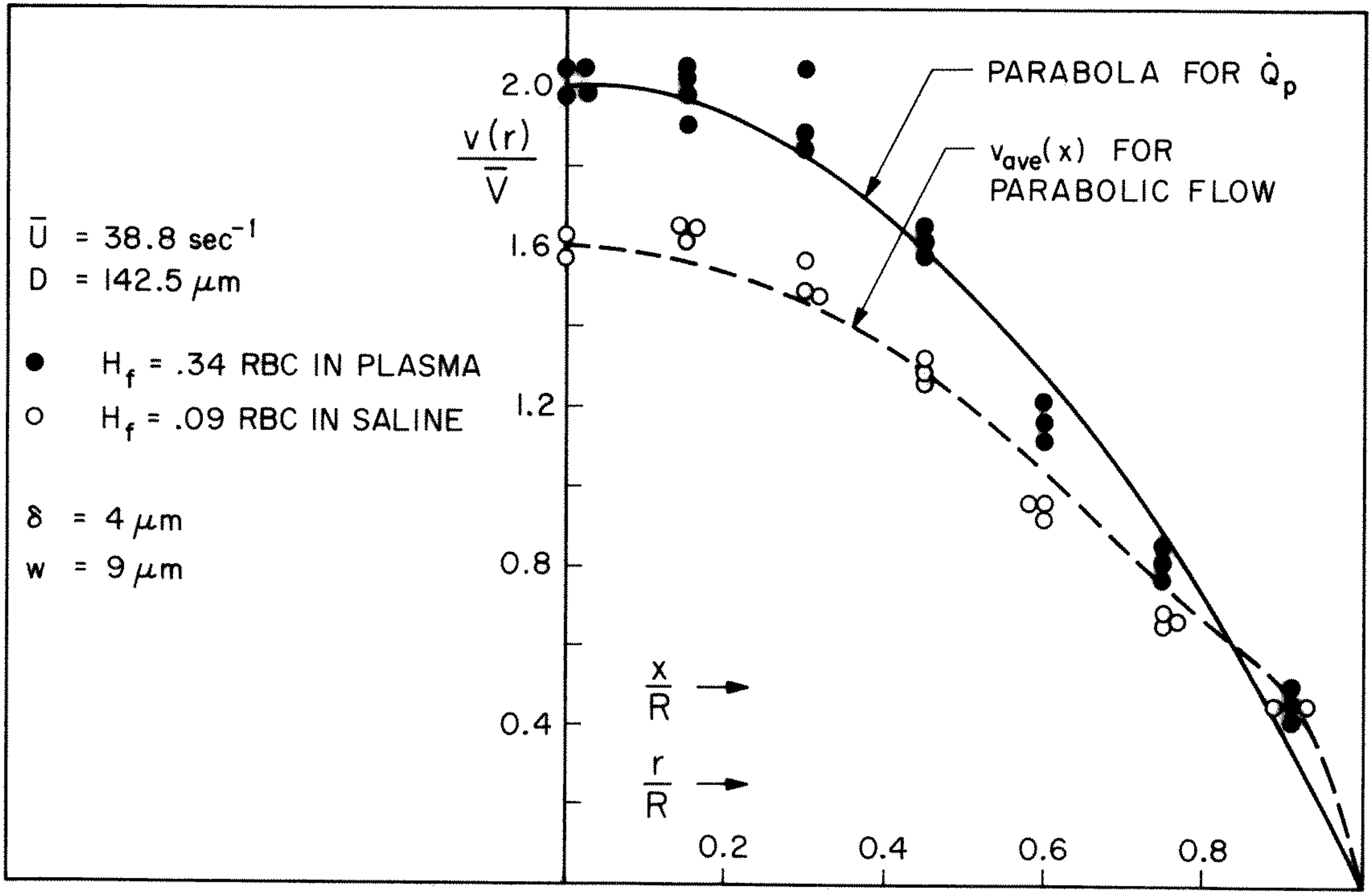

Figure 35 Large Tube Double-Slit Profiles.

The averaging model provides an explanation of the experimental results. The experiments used to check the model are not decisive enough to prove that equation (11) describes what happens in double-slit measurements; however, the consistency of the model predictions and the experimental results provide some confidence that equation (11) at least approximates the actual process.

Use of the Averaging Model in Determining Actual Profiles

Several procedures could be employed to make inferences about actual profiles from the double-slit average measurements.

In principle, equation (11) can be used to solve for an unknown velocity profile, $v(r)$, if an expression for $v(r)$ is constructed with any number of unknown parameters and $v_{ave}(x)$ is measured at the same number of values of x. However, because of uncertainties in the data and the model, this procedure was not considered feasible.

Another approach is to calculate what profiles are expected from rheological measurements, average these profiles using equation (11) and compare the results with measurements. A strong point of this procedure is that dependence can be placed on the centerline velocity measurement. At this point the actual velocity profile is flat enough to make averaging across a phototransistor negligible. This was checked by comparing the centerline value of v_{ave} for a parabolic distribution averaged by equation (10) with that averaged by equation (11). For tube sizes down to 30 μm the difference is less than 1%. Therefore, using the centerline velocity removes the uncertainty in the value of averaging width w. If theoretical profiles are constructed with the correct volume flow rate, the centerline velocity will be a strong indication of the degree of blunting and a measurement at this point provides a check on the theory.

A weak point of any use of the results from double-slit measurements is that the averaging makes the method less sensitive to change. However, large changes in profile shape will be detectable. Therefore, in preparation to carry out the second procedure described above, calculations were made to determine what profiles are expected from rheological data.

VII. EXPECTED PROFILES

Calculation of Profiles from Rheological Measurements

The main relationships needed in order to calculate the distributions of velocity from rheological data are the dependence of shear stress, τ, on shear rate of strain, $\dot{\gamma} = -\frac{dv}{dr}$, for any hematocrit and the distribution of hematocrit across the tube.

Results from careful measurements of τ versus $\dot{\gamma}$ are available. At low shear rates at which the Casson equation describes the flow behavior, this equation was used with constants τ_y and s evaluated from data of Cokelet(16, 20). At higher shear rates the measurements made by Barbee(1) in a capillary viscometer are applicable. These data are presented as τ_w versus $\overline{U}$; however, a relationship between τ and $\dot{\gamma}$ can be derived from his measurements made in an 811 μm tube. For a tube this large, the hematocrit can be assumed to be uniformly distributed because the measured value of the tube hematocrit equals the feed hematocrit. With this assumption of uniformity, the derivation of equation (7) becomes valid. Substitution of $\overline{U} 2\pi R^3 = \dot{Q}$ into this equation produces the following expression for $\dot{\gamma}_w$.

$$\dot{\gamma}_w = 2\overline{U}\left[\frac{\tau_w}{\overline{U}}\frac{\partial \overline{U}}{\partial \tau_w} + 3\right] \tag{13}$$

τ_w can be eliminated by using equation (9) which was developed by Barbee to represent his data for the 811 μm tube. The result is an expression for $\dot{\gamma}_w$ in terms of H and $\overline{U}$.

$$\dot{\gamma}_w = \left[6 + \left(\frac{2}{1 - \frac{4.2cH}{\overline{U}^c}}\right)\right]\overline{U} \qquad (14)$$

(In the limiting cases when H is zero or $\overline{U}$ is very large, blood is expected to act as a Newtonian fluid. For these limits, equation (14) approaches the expression $\dot{\gamma}_w = 8\overline{U}$ which is the correct result for a Newtonian fluid.) Equations (9) and (14) together provide the needed functional relationship between τ, $\dot{\gamma}$, H. For any given hematocrit, the substitution of values of $\overline{U}$ into equations (9) and (14) provide corresponding values of τ and $\dot{\gamma}$. The range of validity of these expressions derived from data of Barbee overlaps the range of validity of the Casson equation and extends to a $\overline{U}$ of 100 sec^{-1}.

In order to compare this derivation of τ versus $\dot{\gamma}$ relationships with results of measurements in a Couette viscometer, a plot was made of $\tau^{1/2}$ versus $\dot{\gamma}^{1/2}$ from equations (9) and (14). On this same plot, shown in Figure 36, lines were drawn to represent the data of Brooks, Goodwin and Seaman presented previously in Figure 6. For hematocrits up to .476 the agreement of the Couette measurements and the derivation from capillary measurements is very good. This agreement provides confidence in the above derivation and eliminates the need of a choice between data from capillary viscometer and data from a Couette viscometer.

In order to proceed with the profile calculation the distribution of hematocrit, H(r), is also needed. Since quantitative measurements of this are not available, a general form with free parameters was used.

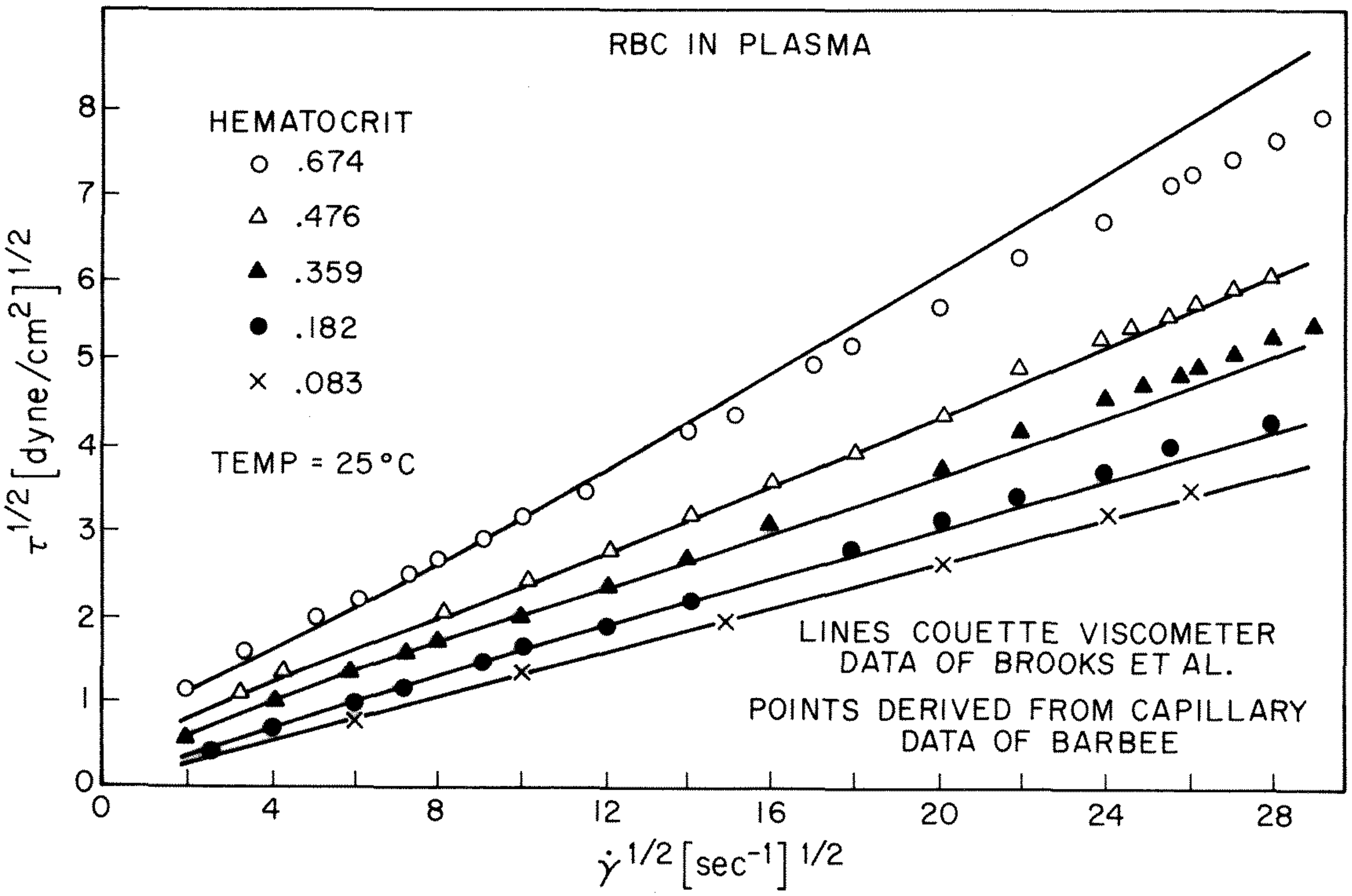

Figure 36 Comparison of Couette and Capillary Data.

The choice of general form was guided by qualitative observation of H(r). The tube hematocrit relative to feed hematocrit data indicates a non-uniform distribution for tubes less than 220μm in diameter. Barbee(1) showed that these data can be accounted for by mechanical wall-exclusion of cells alone. Measurements of Palmer(43) for flow between two plates of separation from 12 to 112μm indicate an almost linear decrease in hematocrit from the channel center to the wall. This linear decrease has a slope which is greatest in the smallest channels and almost disappears leaving nearly uniform hematocrit for the 112μm channel. The only non-uniformity in distribution that is observed from pictures of blood flowing in a tube is a paucity but not absence of cells very near the tube wall. In general, the observations indicate a maximum concentration of red cells in the tube center with some decrease to zero at the wall where cells are excluded. From these considerations the following form was chosen for H(r):

$$H(r) = H^*(1-(r/R)^E). \tag{15}$$

The values of H^* and E were allowed to vary in order to satisfy two constraints. The first was

$$H_t = \frac{2}{R^2}\int_0^R H(r)\, r\, dr \tag{16}$$

which leads to the following relation between H^* and E.

$$H^* = \left(\frac{E+2}{E}\right)H_t. \tag{17}$$

The second constraint used was that the final profile must result in the correct volume flow rate when integrated.

$$\overline{U} 2\pi R^3 = 2\pi \int_0^R v(r)\, r\, dr. \qquad (18)$$

Calculations of profiles were carried out numerically for a range of values of $\overline{U}$, H_f, R. From R and H_f, a value for H_t was obtained using the empirical equations constructed by Barbee$^{(1)}$ to represent his data shown in Figure 8. Using this H_t in equation (9) provided a value for τ_w and thereby the shear stress, $\tau(r)$, at any point in the tube. Next a starting value for E was chosen and the corresponding value for H^* was calculated from equation (17). The integration of $\dot{\gamma} = -\frac{dv}{dr}$ was then started by setting $v(R) = 0$ and moving in steps from $r = R$ to $r = 0$. At each value of r, H(r) was evaluated, and the $\dot{\gamma}$ which corresponds to each $\tau(r)$ was calculated from trial and error solution of equations (9) and (14). Each value of $\dot{\gamma}$ obtained was tested to be sure it was high enough to allow use of the Barbee data. For values of $\dot{\gamma}$ that were below the range of Barbee's measurements, the Casson equation was used. In this way a trial profile was generated for the guessed value of E. This profile was integrated in order to find the corresponding value of volume flow rate. This calculated $\dot{Q}$ was then compared with $\dot{Q}$ corresponding to the $\overline{U}$ at which the calculation was started. If the agreement was not within 1%, the value of E was adjusted and a new profile was generated. This process was continued until the volume flow rate constraint was satisfied. Many different starting guesses of E were tried for each combination of $\overline{U}$, H_f and R in a large range of each variable. The calculation scheme always converged and always to the same value of E for a given $\overline{U}$, H_f, R combination. The resultant value of E was greater than 15 and usually 40-50 for all profiles except very low hematocrits.

The profiles predicted from these calculations are surprisingly close to parabolic for almost all values of $\overline{U}$ and hematocrit. Figure 37 shows the change with $\overline{U}$ of profile shape at normal hematocrit. For a tenfold $\overline{U}$ decrease from 60 to 6 $\sec^{-1}$, the predicted profile shape does not change substantially from a parabola. The only blunting predicted is that for $\overline{U} < 2 \sec^{-1}$ where yield stress is no longer negligible in comparison to wall shear stress. The main determinant of predicted profile shape for $\overline{U} < 2 \sec^{-1}$ is the particular value of yield stress used in the calculation. The range of profiles shown in Figure 37 for $\overline{U} = .6$ represents the range of yield stress values found in different normal blood samples. Figure 38 shows the same change with $\overline{U}$ of profile shape for profiles averaged by equation (11). The difference between Figures 37 and 38 demonstrates the loss of sensitivity caused by the double-slit averaging. The predicted changes in profile shapes with hematocrit changes are also small. The velocity along the centerline falls below the parabolic centerline velocity by less than 5% for all feed hematocrits from .15 to .60 and $\overline{U}$ values above 2 $\sec^{-1}$. The only exceptions to this are the profiles for very high hematocrits ($H \geq .50$) in the $\overline{U}$ range 2-20 $\sec^{-1}$ for which centerline velocities may fall as much as 10% below the parabolic value.

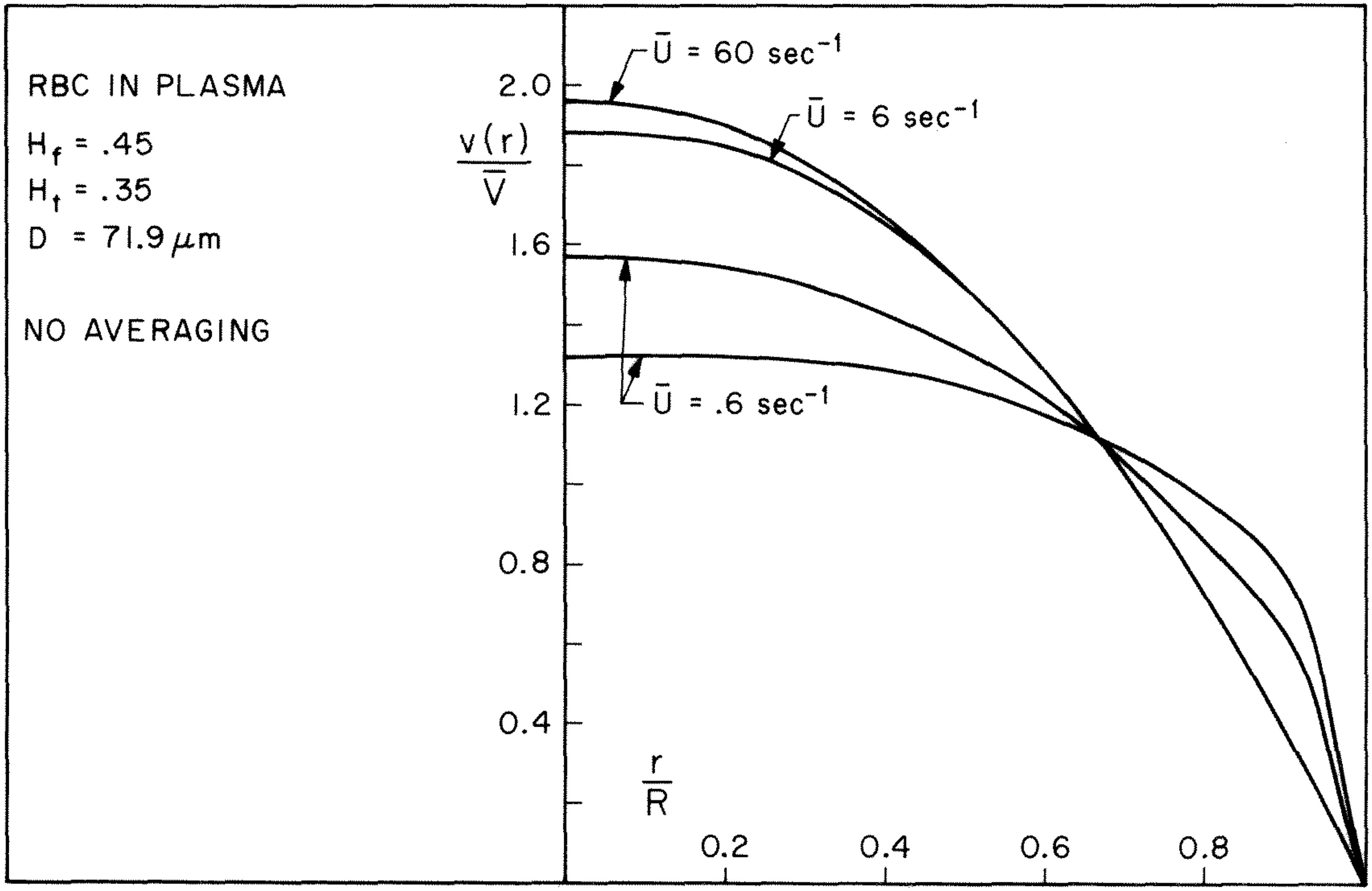

Figure 37 Variation with $\overline{U}$ in Shape of Predicted Profiles.

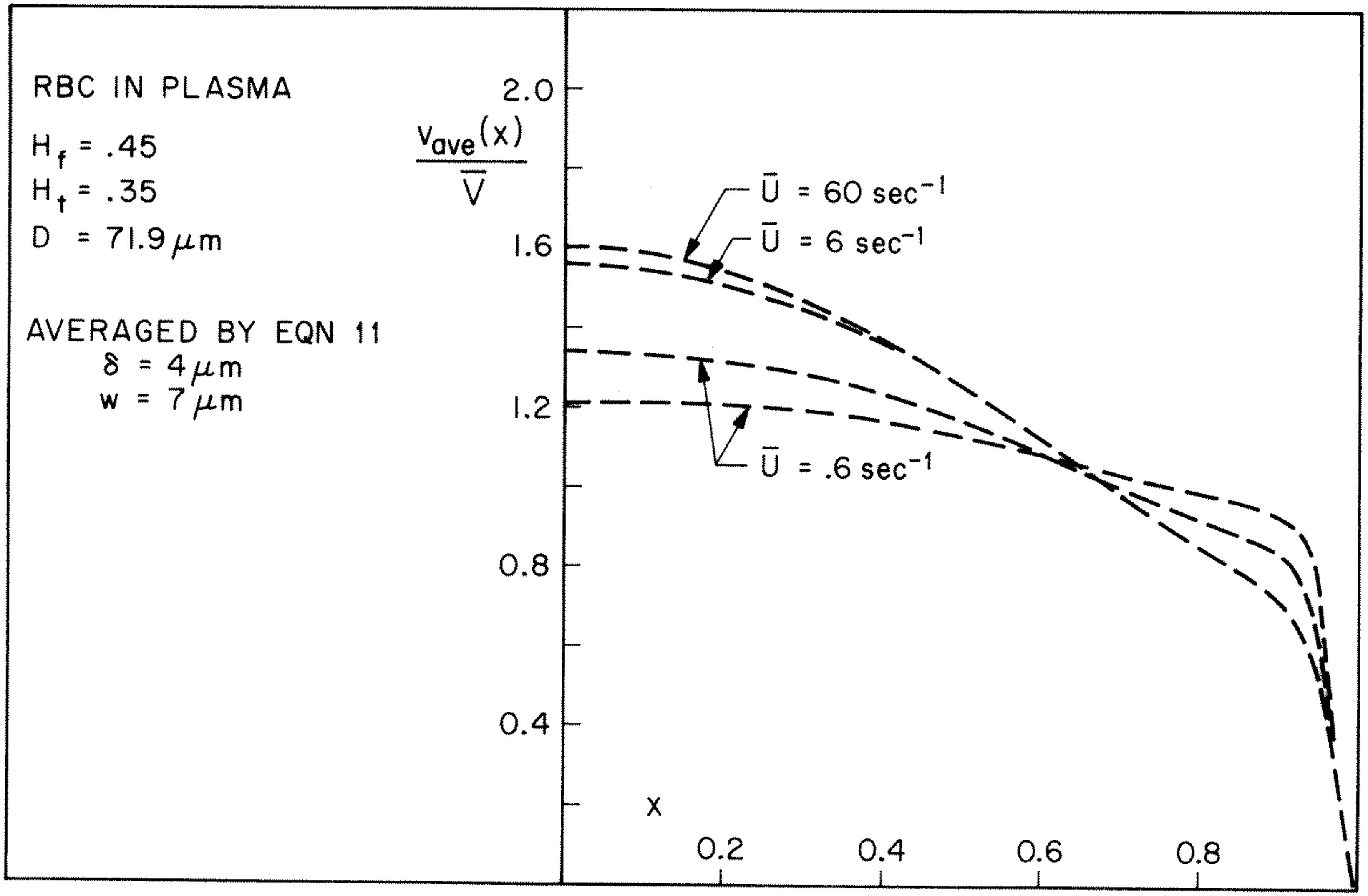

Figure 38 Variation with $\overline{U}$ in Shape of Predicted Averaged Profiles.

This prediction of velocity profiles from bulk rheological data implies the validity of a continuum model. The limit of usefulness of continuum methods has not been established for blood flow in terms of minimum tube diameter. The tubes used for the double-slit methods are too small for the red cell diameter to be considered negligible in comparison. Certainly a large change in shear rate occurs across a single particle for these tubes. However, the Barbee and Cokelet(3) work showed that bulk rheological data could be useful for predicting τ_w versus $\overline{U}$ behavior down to tube diameters of 29µm. Therefore, the profile predictions seemed worth considering as trial profiles for comparison with profile measurements.

Comparison of Predicted and Measured Profiles

Measured profiles available for comparison with calculated profiles are those of Bugliarello and coworkers(10, 11, 13) from motion picture analysis, those of Gaehtgens(29) and those of this thesis. Profiles were calculated to correspond in $\overline{U}$, H_f, and R with these measurements. Equation (11) was used to average those predicted profiles if the corresponding measurements were by the double-slit technique at hematocrits and tube sizes for which the averaging model is applicable. For those large tubes and high hematocrits for which averaging in the direction of the optic axis was shown in Chapter VI to be negligible, only averaging across the phototransistor was applied to the calculated profiles.

Comparisons between measured and predicted profiles for a range of values of R, $\overline{U}$ and H_f are shown in Figures 39-46. The dotted line in each figure represents the profile predicted from rheological measurements and averaging considerations. When averaging was applied, a solid line was also drawn to represent the unaveraged predicted profiles. In agreement with the profile calculations, very little blunting was measured other than that due to the averaging distortion. Comparison of Figures 39 and 40 shows that the fivefold change in $\overline{U}$ at the high hematocrit of .58 caused only a very small change in both the predicted and measured profiles. Another profile very similar to these was measured and calculated for the low hematocrit and very high $\overline{U}$ of Figure 41. In Figure 42, a slightly blunter profile measurement is shown in accordance with the shape change expected from averaging in this smaller diameter tube. The only true blunting measured was for the $\overline{U}$ of 1.94 $\sec^{-1}$ shown in Figure 43. The blunting becomes evident when this figure is compared with Figure 44 which shows a high $\overline{U}$ profile measured in the same tube. (The profiles of Figures 43 and 44 are affected very little by averaging because of the large tube diameter and high hematocrit. The only change due to averaging is a slight raising of the velocity nearest the wall shown by the difference between the dotted and solid line there.) One of the motion picture profiles of Bugliarello et al., is shown in Figure 45. All profiles published by this group are at high enough τ_w to make τ_y negligible in comparison. The extreme blunting found by Gaehtgens is shown in Figure 46. The predicted profile for this situation is nearly parabolic. The averaging for the low magnification that he used totally accounts for the blunting measured. The above comparison shows that the

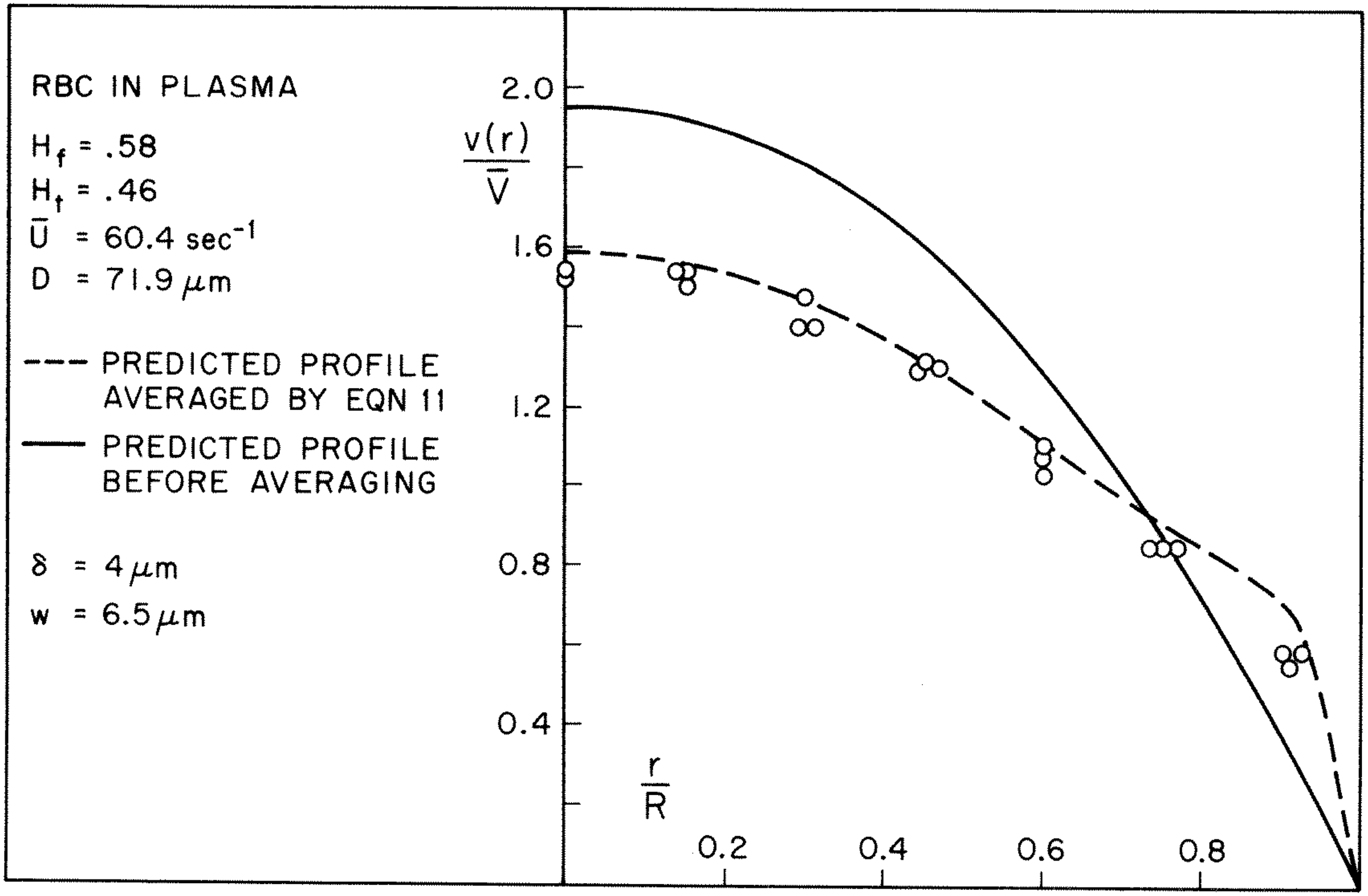

Figure 39 Comparison of Measured and Predicted Profiles.

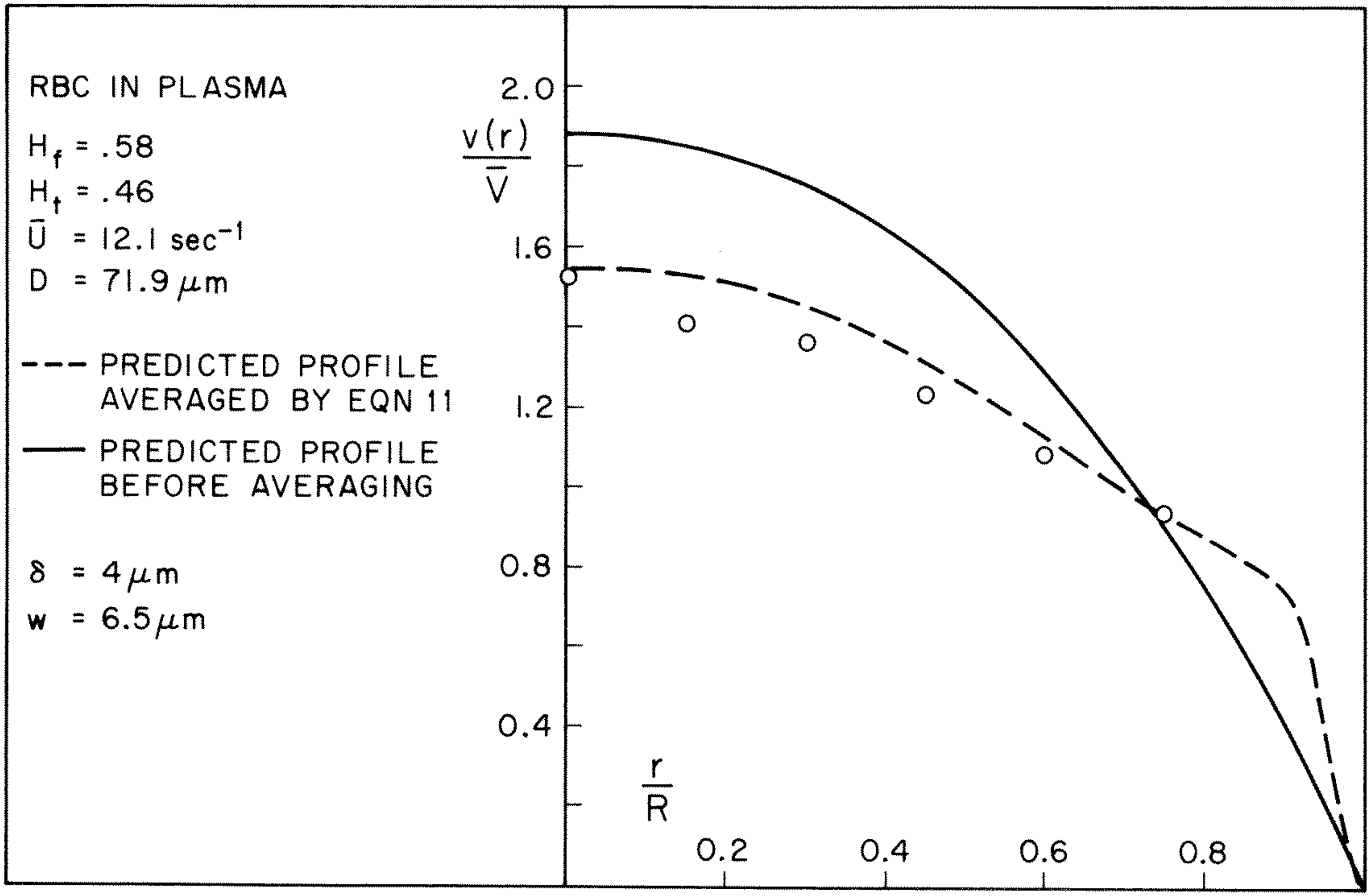

Figure 40 Comparison of Measured and Predicted Profiles.

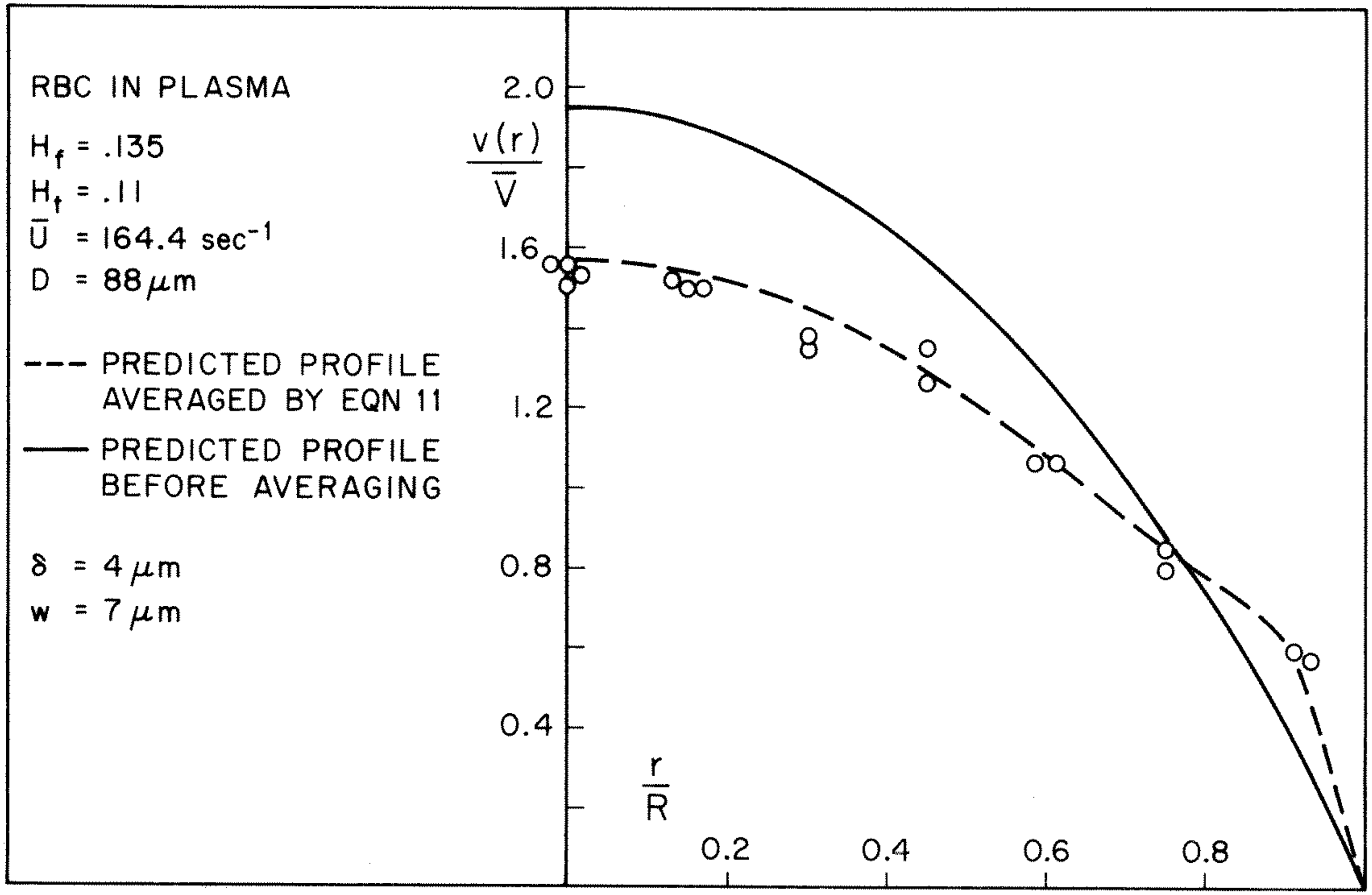

Figure 41 Comparison of Measured and Predicted Profiles.

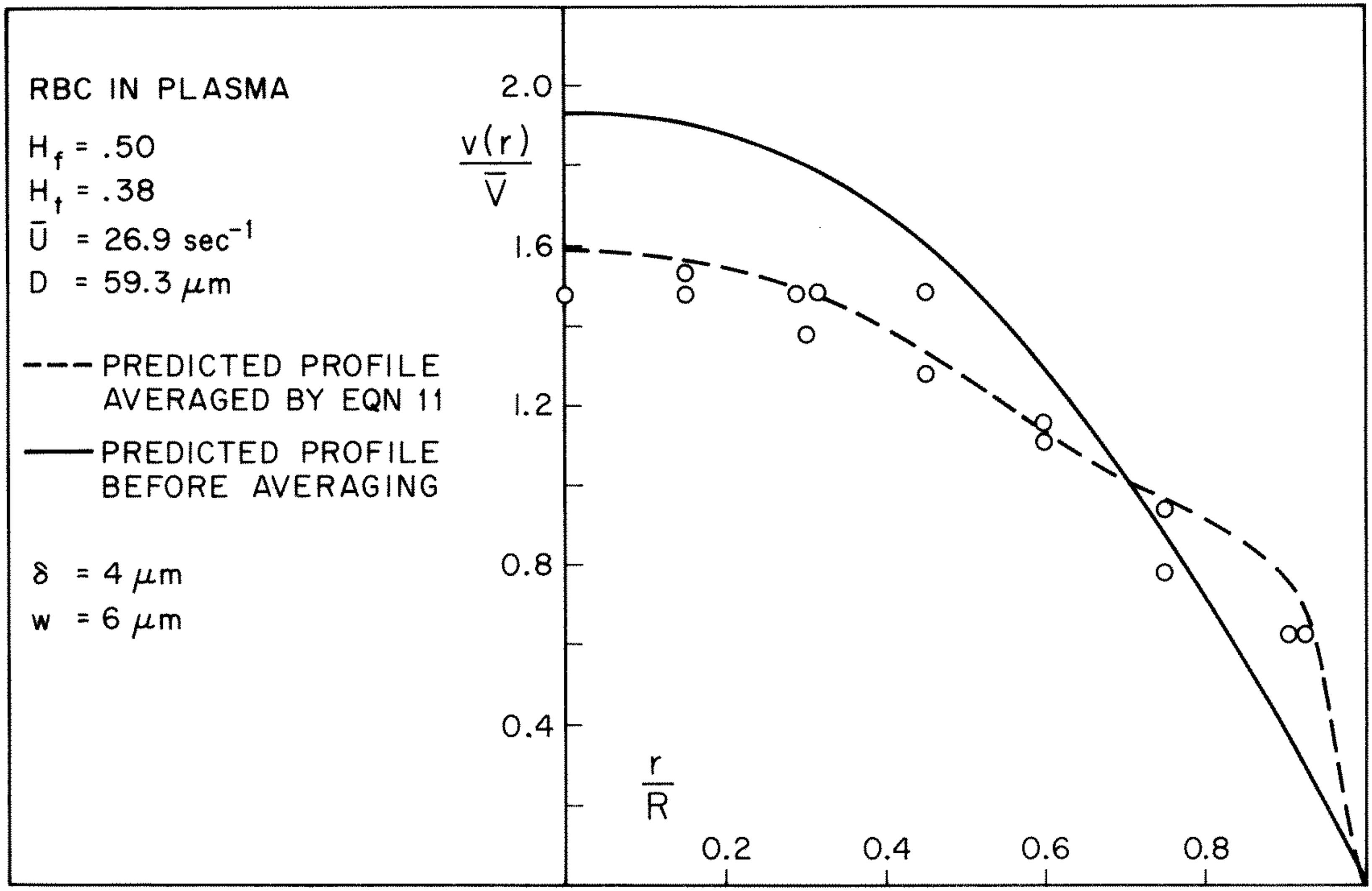

Figure 42 Comparison of Measured and Predicted Profiles.

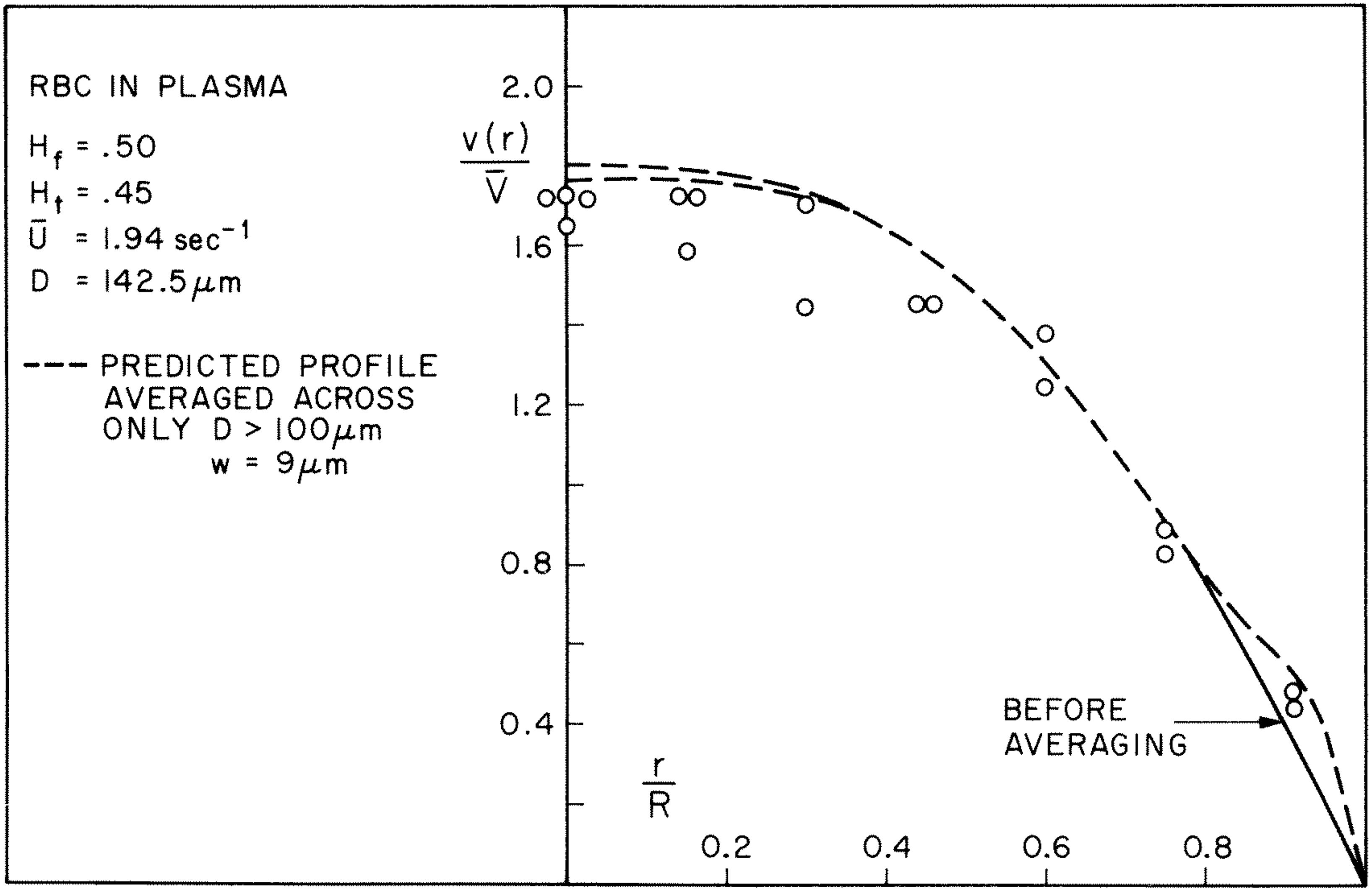

Figure 43 Comparison of Measured and Predicted Profiles. (Double Line Represents Variability of Yield Stress.)

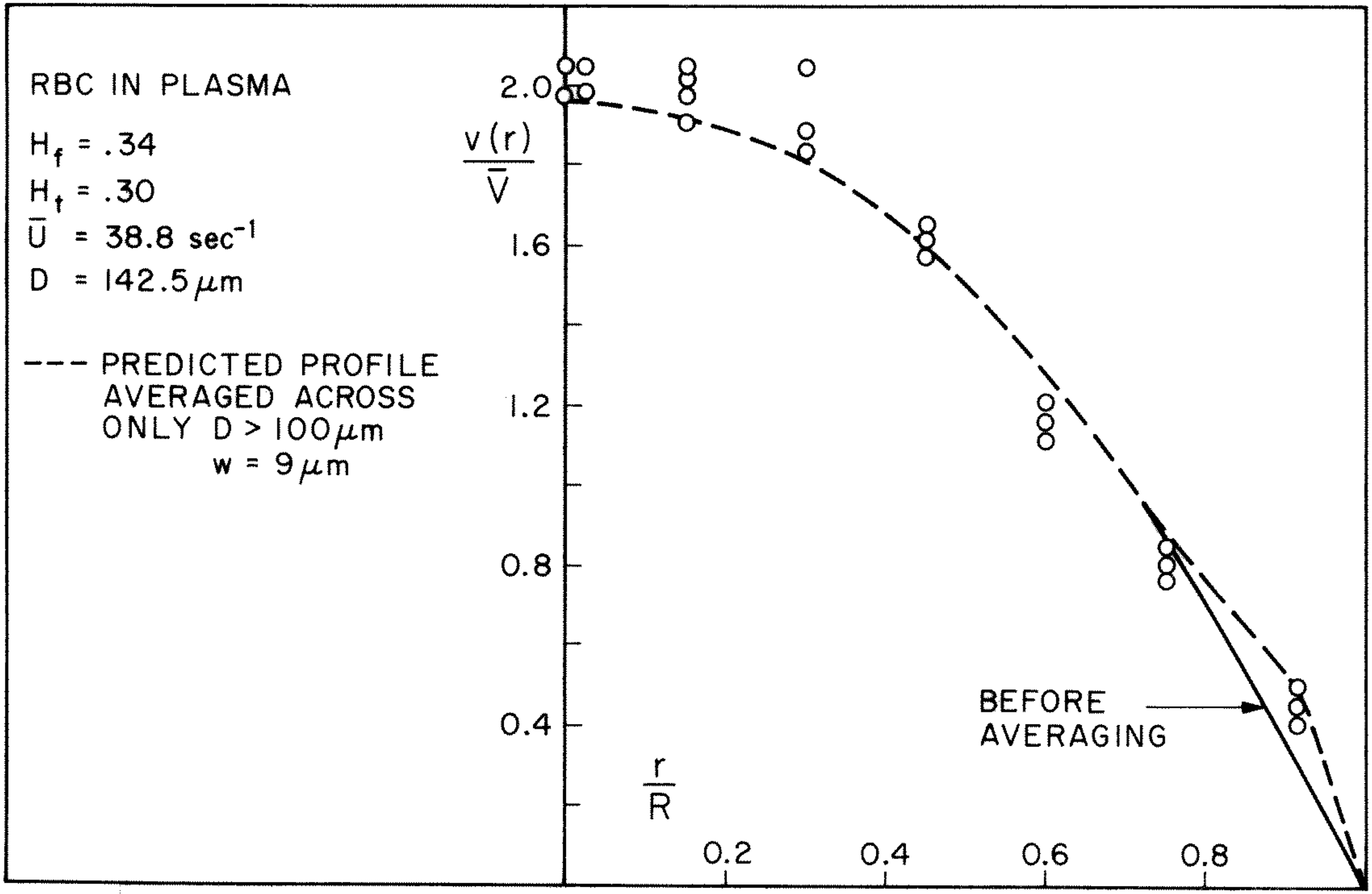

Figure 44 Comparison of Measured and Predicted Profiles.

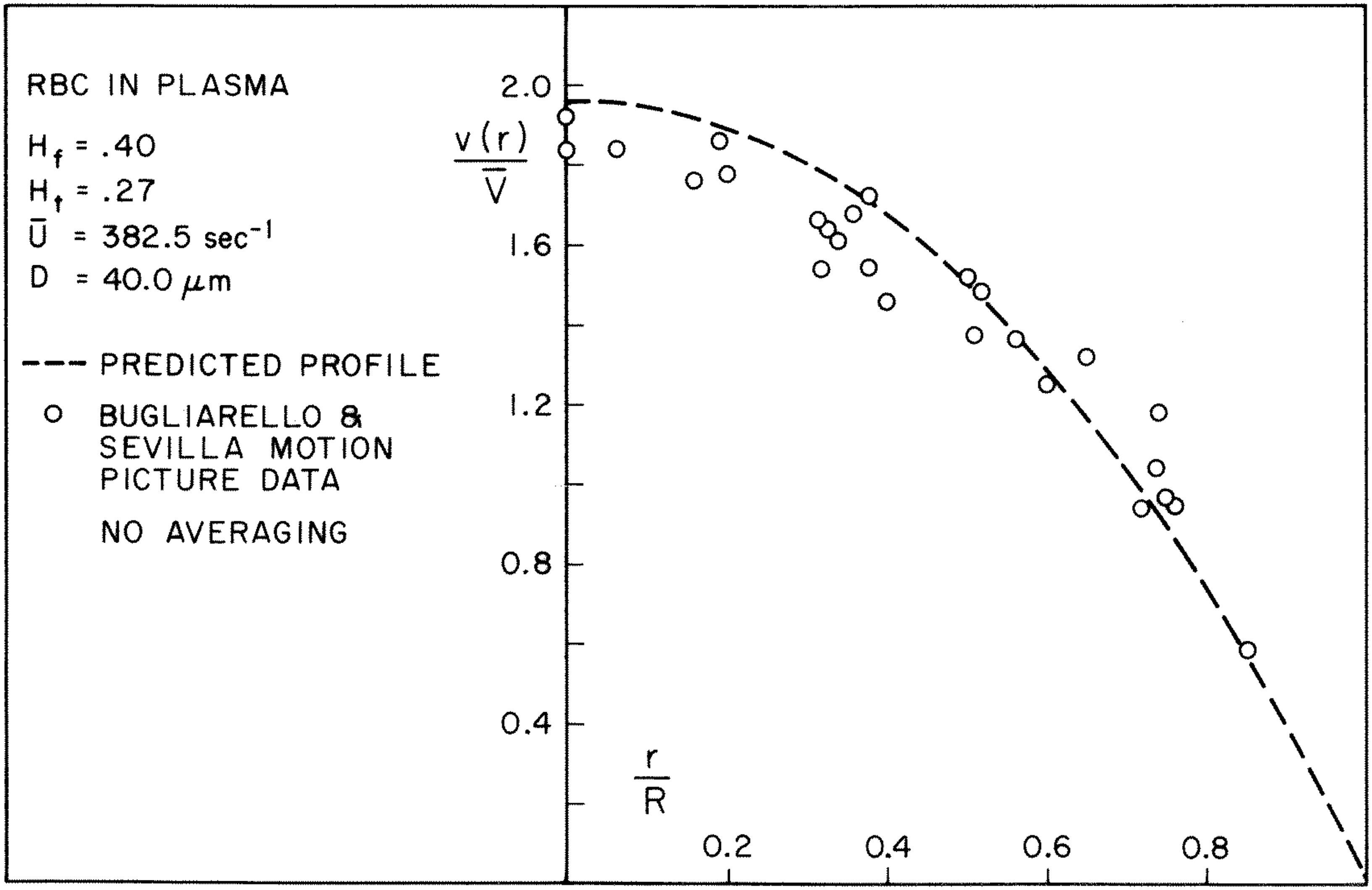

Figure 45 Comparison of Measured and Predicted Profiles.

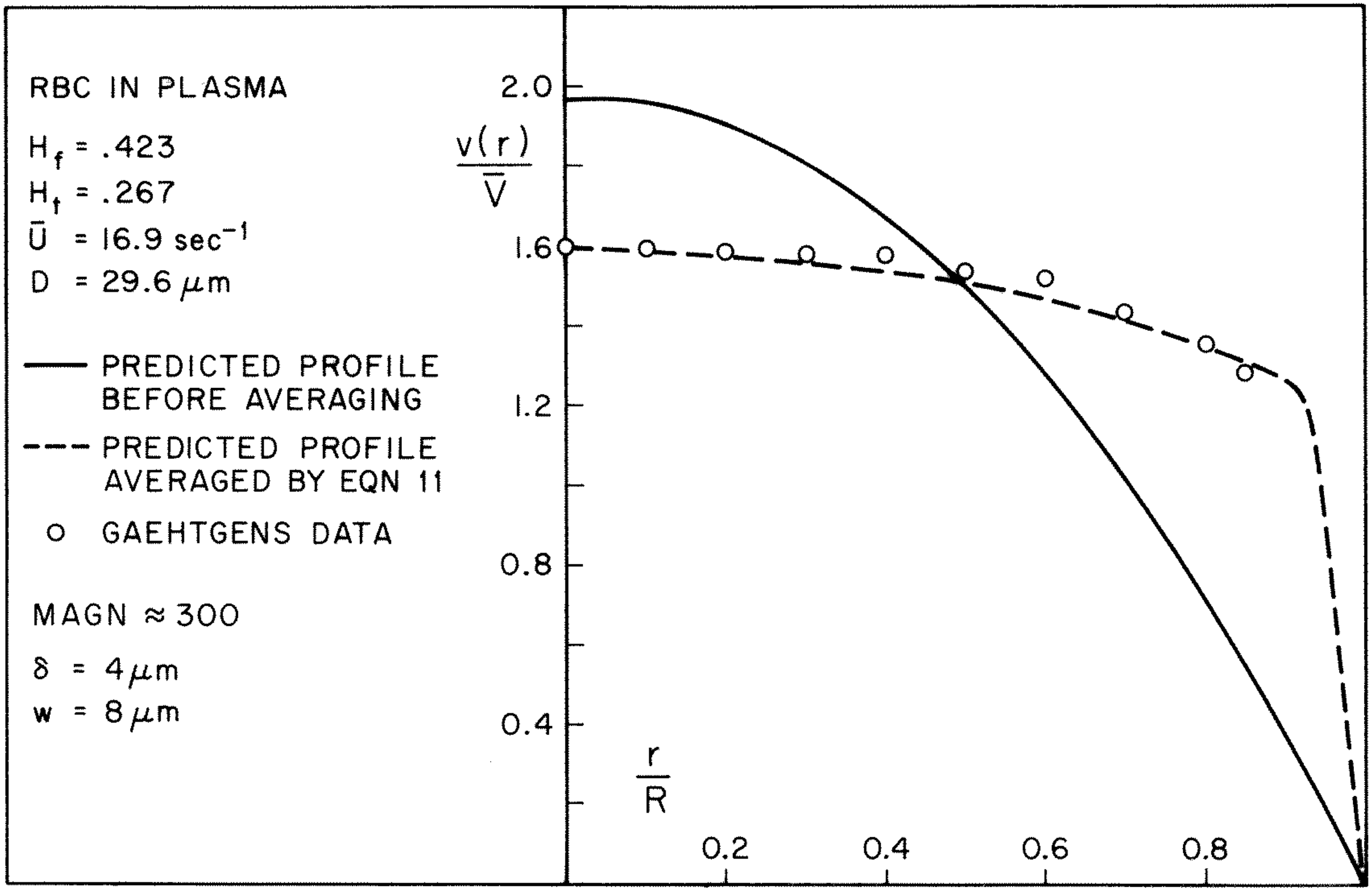

Figure 46 Comparison of Measured and Predicted Profiles.

measured and calculated profiles are consistent within the accuracy of the measurements.

In addition to the profiles shown many more comparisons with the data of Gaehtgens and Bugliarello were plotted. All the profile shapes of Gaehtgens agreed with the corresponding predictions; when profiles were calculated for the Bugliarello data, the agreement was not as complete. Most of the profile measurements presented by the Bugliarello group checked with calculated profiles but several did not. The discrepancies were not at all systematic; that is, they did not occur in the same range of H or $\overline{U}$ or R. The disagreement appears to be more of a discrepancy between different profiles measured by this group rather than a strong indication that the calculated profiles are wrong.

One factor which weakens these comparisons of calculations with profiles measured by other investigators, is the lack of availability of an independently measured volume flow rate. This value had to be obtained from the profile itself. Obtaining $\dot{Q}$ in this way makes it much easier to obtain agreement between measured and calculated profiles. However, the comparison in profile shapes alone is still meaningful.

The lowest $\overline{U}$ value at which quantitative comparison between predicted and measured profiles was made is 2 $\sec^{-1}$. There are several reasons for this limit. 1) At flow rates below $\overline{U}=2\sec^{-1}$, steady flow was very difficult to maintain because of limitations in the syringe pump and in the temperature control. The fluctuations in flow rate which occurred at these $\overline{U}$ values caused enough scatter in the velocity measurements to make the profile shape determination difficult. 2) The Barbee data, on which the prediction of τ_w from $\overline{U}$ was based, were not extended to $\overline{U}$ values below 2 $\sec^{-1}$ for tubes smaller than 811 μm in diameter. 3) No independent measure of yield stress was available; therefore, any calculation scheme could only predict profiles within a range due to variability of yield stress.

A qualitative check of the profile prediction that blunting due to yield stress should become substantial for $\overline{U} < 2 \sec^{-1}$ was made. The flow behavior was observed directly by watching the cells in the image of flowing blood. For $\overline{U} < 2 \sec^{-1}$, the red cells move so slowly that, even after a magnification of several hundred, the motion is not fast enough to make the cells appear blurred. Individual cells can be distinguished and followed. A flow rate corresponding to about 2 $\sec^{-1}$ was obtained and allowed to decrease slowly. The progressive importance of yield stress on the velocity distribution was evident. At first, cells at different radii moved past each other; then as flow rate decreased, many cells became aggregated and flowed together. Eventually all cells flowed in a plug with cell free layer at the wall.

Discrepancy Between Outflow and Feed Hematocrit

Although calculated profiles seem to agree quite well with measured profiles, there is a definite discrepancy between these calculations and other experimental data. The measurements of Barbee show that the hematocrit flowing out the downstream end of the tube, H_d, is equal to the feed hematocrit for tubes down to 59 μm in diameter. When H_d is calculated for the predicted profiles, the result is close to the tube hematocrit which is much less than the feed hematocrit. (Figure 8 shows the comparison between feed hematocrit and tube hematocrit for different tube sizes).

This equivalence of calculated H_d and H_t is not surprising for the predicted profiles because the result of the iteration for H(r) was a nearly uniform hematocrit distribution (E very large). A constant hematocrit across the tube is certainly one possible solution to the equation. This is true because a uniform distribution was assumed for a large tube and the measurements of Barbee, which were used, show that the τ_w versus $\overline{U}$ relationship is the same for a large tube ($D > 220\mu m$) as for a small tube ($D < 220\mu m$) once the actual tube hematocrit is taken into account. If all the experimental evidence is to be satisfied by continuum calculations, another H(r) must exist, at least for tubes small enough for H_r to be less than one.

In an effort to find another solution for H(r), changes were made in the scheme of predicting profiles. Several expressions for H(r) were tried with three undetermined parameters. The three constraints used to evaluate these parameters were expressions 16, 18 and the following

$$H_f = H_d = \frac{\int_0^R H(r)v(r)\,r\,dr}{\int_0^R v(r)\,r\,dr} \; . \qquad (19)$$

The trial forms of H(r) included 1) the "tubular pinch effect" of Segré and Silberberg(50, 51)(Appendix D) with red cell concentration highest at some nonzero value of r; 2) a uniform cell concentration across the center of the tube with a linear decrease to a lower, possibly zero, wall hematocrit, $H(R)$; and 3) paucity of cells in the center using $H(r)$ proportional to $H_f(\overline{V}/v(r))$ with some finite $H(R)$. In every case the iteration for constraint (19) tried to move the cells toward the center of the tube and the iteration for constraint (18) tried to produce a uniform distribution of cells across the tube. Changes in parameters which produced convergence on one condition caused divergence from the other condition. No expression for $H(r)$ was found which could satisfy all the conditions.

Profiles were calculated with the constraint on outflow hematocrit satisfied in order to determine how large an error would result in volume flow rate. For this calculation the two most common guesses for $H(r)$ were used. These distributions are 1) a constant hematocrit, H^*, for $r=0$ to $r=R-\delta$ with a linear decrease to zero for $r=R-\delta$ to $r=R$; and 2) a constant hematocrit, H^*, for $r=0$ to $r=R-\delta$ with a cell free layer from $r=R-\delta$ to $r=R$. The first form of $H(r)$ could not be made to satisfy the outflow hematocrit condition. Even if there is a linear decrease in hematocrit from the tube center to the wall, the value of H_d is less than feed hematocrit. Using the second $H(r)$, a profile was calculated with the correct outflow hematocrit. This profile is shown in Figure 47 along with the profile measured from motion picture analysis. The volume flow rate for the calculated profile is about 40% higher than the flow rate corresponding to the $\overline{U}$ value from which the calculation was begun. Also the profile shape does not agree with measurements even if the volume flow rate is adjusted.

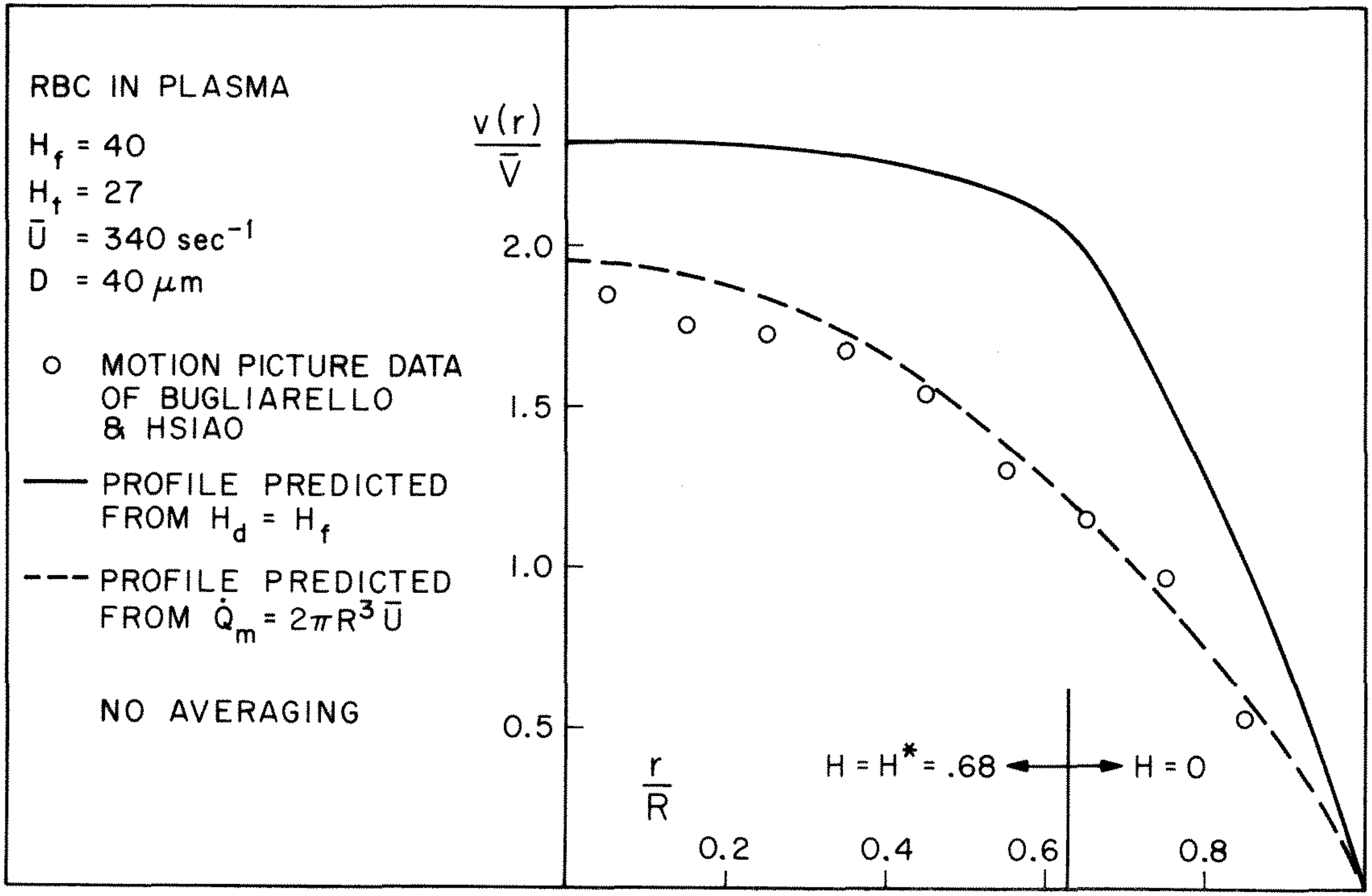

Figure 47 Profile Calculated to Satisfy $H_d = H_f$.

Continuum Model Consideration

The profile measurements clearly favor the first scheme of profile calculations where the iteration satisfies the volume flow rate constraint; however, the outflow hematocrit measurements must be satisfied also. The experimental determination of H_f, H_t and H_d give a very much more realistic indication of the actual distribution of hematocrit than H(r) obtained through the profile calculations. These discrepancies seem to represent a breakdown in the continuum model representation. Certainly the results from large tube measurements do not totally predict behavior in the small tube situation.

The actual phenomenon in the tube appears to be a nearly uniform distribution of viscosity caused by the red cell presence even though the cells themselves are not uniformly distributed. This is not physically unreasonable considering the gradient in shear rate in the tube. Near the tube wall there is a greater change in velocity across a single particle than near the tube center. This means a greater disturbance in the flow field per particle near the wall and therefore a greater energy dissipation. Another possible explanation for an increase in viscosity near the wall is interaction between the red cells and the wall. Since cells are observed to bump into the capillary wall, friction between the cells and the wall, or bending of cells at the wall may contribute enough to viscosity to partially compensate for a reduced hematocrit there. Whatever the true phenomena in the tube, the behavior cannot be predicted from the bulk measurements, and a limit in the continuum approach is defined.

Volume Flow Rates for Physiological Purposes

The true profile shapes and double-slit distortions are known well enough to calculate volume flow rates for physiological purposes within 5-10% which is within the limits of error of other physiological measurements such as vessel diameter and hematocrit.

All profiles predicted from the satisfaction of volume flow rate constraint are nearly parabolic as long as wall shear stress is well above the yield stress of blood. For vessels larger than 220 μm in diameter there are no discrepancies between experimental measurements and profile predictions. In smaller vessels, the outflow hematocrit discrepancy places doubt on the calculated profiles. There may actually be some additional profile shape changes due to tube size for very small tubes which a continuum model calculation cannot predict. However, deviations from the predicted profiles are small enough to be unnoticeable with the double-slit measurements. Since the yield stress for a given animal's blood is usually not known, the lack of a check of the profiles in the low $\overline{U}$ range is not much of a further limitation for physiological measurements.

With nearly parabolic profiles, volume flow rates can be calculated from centerline velocity measurements. The correction for double-slit averaging is quite simple at this point. The measured centerline velocity, V_{cl}, is just $.8V_{max}$ where V_{max} is the maximum velocity for parabolic flow; therefore, the volume flow rate expression is

$$\dot{Q} = \frac{5}{4} V_{cl} \frac{\pi R^2}{2} . \tag{20}$$

The validity of this expression should be checked for each optical set-up and vessel diameter by changing focus while measuring a velocity. Equation (20) is valid if the velocity remains constant with different focal positions. The upper limit in vessel diameter for which this expression is expected to hold is about 90 μm. The double-slit technique can be used for much larger vessels; however, between 90 μm and 140 μm, the relationship between V_{max} and V_{cl} is not known and will probably depend on the particular optical set-up and certainly on hematocrit. For vessels larger than 140 μm and at hematocrits greater than .30, V_{cl} is expected to equal actual velocity; that is, $V_{cl}=V_{max}$.

For measurements of blood flow in true capillaries the volume flow rate measurement is an entirely different problem. The double-slit distortions are irrelevant here because there is only one layer of cells; the actual red cell velocities will be measured directly. However, the exact relationship between red cell velocities and volume flow rates is not known. The average red cell velocity is much greater than average fluid velocity for vessels this small. A discussion of the relationship between red cell velocities and flow rates for capillaries is given by Wayland(55).

VIII. CONCLUSIONS

It has been demonstrated that the double-slit photometric method distorts velocity profiles causing them to appear very much blunter than they actually are. The nature of the distortion is the averaging of events over an area which extends from the front to back tube walls and for a distance on each side of the sensor of approximately a red cell radius. An equation developed to model this averaging predicts profiles which agree with experimental results. The extreme blunting of velocity profiles with decrease in tube size reported by Gaehtgens can easily be explained by this averaging model even if the true profiles are parabolic.

The discovery of the distortions left the actual profile shapes still unknown. The nature of the averaging model equation, the uncertainties in the averaging width, and the scatter in the measured velocities at points near the wall make direct solving of the averaging equation for the true velocity distribution unfeasible. Instead, a trial and error method was chosen to extract information about actual profiles from the double-slit averaged velocities. Trial profiles were generated using τ versus $\dot{\gamma}$ relationships obtained from Barbee's bulk rheological measurements. Since distribution of hematocrit with radius is not known, it was varied in order to satisfy the constraint that calculated profiles have the correct volume flow rate. The trial profiles were averaged with the averaging model equation and compared with double-slit measurements. The predicted and measured profiles were consistent; neither gave any evidence of substantial blunting except for $\overline{U} < 2\,\mathrm{sec}^{-1}$ where yield stress is no longer negligible in comparison to wall shear stress.

Although the continuum approach was used to predict trial profiles, limitations in the continuum model validity were evident from hematocrit considerations. Any profile calculation which satisfied the constraint that outflow hematocrit equals feed hematocrit also predicted profiles much blunter than measured profiles and volume flow rates much higher than $2\pi R^3\overline{U}$ for the $\overline{U}$ at which the calculation was started. Any profile calculation which satisfied the volume flow rate constraint produced outflow hematocrit closer to tube hematocrit than feed hematocrit. These discrepancies were interpreted as a breakdown in the continuum representation for blood flow in tubes less than 220 μm in diameter.

The double-slit method is still an extremely useful tool for physiologists. The limitations due to the distortions are minor for physiologic applications because a simple correction has been determined for the calculation of volume flow rates. The double-slit technique is much more convenient and covers a larger range of variables than any other method now available for monitoring velocities and flow rates in microvessels. If the details of calibration of the single-slit technique are improved, this method may be able to provide a simplification in the electronics needed for analysis. If many vessels must be monitored simultaneously, a great reduction in electronic equipment can be obtained by using single-slit apparatus except for one set of double-slit equipment which can be used as an in situ calibration of the single-slit analysis.

When the double-slit photometric technique is used for rheological measurements, the limitations are more severe. The uncertainties in parameters, such as width over which averaging should be carried out, greatly reduce the usefulness of the method. Since the parameters in the averaging model change with tube size, the double-slit technique is not a good tool for studying actual profile changes with tube diameter. The measurements by this method are not considered accurate enough to distinguish between rheological models by procedures which use the whole profile shape.

APPENDIX A: VELOCITY PROFILES FOR GHOST CELL SUSPENSIONS

The opacity of concentrated suspensions of red cells limits the number of techniques available for measuring velocity profiles. Some limitations are removed if red cell ghosts (red cells with hemoglobin removed) are substituted for true red cells. These suspensions cannot be assumed to show the same behavior as blood. For example, no rouleaux formation is observed. However, measurements on ghost cell suspensions do provide information on concentrated suspensions of flexible particles of the same shape as red cells.

Goldsmith(36) measured velocity profiles using a few red cells as tracer particles in the suspension of ghost cells. He found only slight blunting from parabolic flow compared to the pronounced blunting at the same concentration for rigid particles.

Kreid and Goldstein(39) used the laser-Doppler technique to obtain velocity profile measurements for ghost cell suspensions flowing between two parallel plates. Since this measurement method involves totally different principles than any of the other methods now in use, it may yield interesting results in the future. However, the profiles reported by these investigators are not meaningful in their present form. No independent measurements were made of pressure drop across the channel or volume flow rates. The profiles that were presented were drawn by fitting data with a Casson equation which contained wall shear stress as a multiple of an independently measured yield stress. The values of yield stress used were ten times too high even for blood and should have been zero for the suspensions used. The reported errors in measurements were ±25% near the channel wall. With no volume flow rate constraint, large errors in velocity near the walls, and an incorrect model used for fitting of the data, the profiles presented are not meaningful. Some of the profiles were very blunt but the shapes did not vary consistently with $\overline{U}$ or hematocrit.

One of the major limitations of laser-Doppler apparatus to measurements of velocities in blood-like suspensions is the large spatial resolution (diameter of volume from which coherent scattering can be detected) of these instruments. For the Kreid and Goldstein investigation, the spatial resolution was about 11 μm which explains their use of the relatively large channel widths of 400 to 2300 μm. It is doubtful that this method in its present form can yield results for channel widths below the range of continuum model validity.

APPENDIX B: CAPILLARY TUBE CONSTRUCTION

Two main types of capillaries were used. When the free working distance of the lens used was large enough, thick-walled tubing with outside diameter of 5-6mm was satisfactory. For the oil immersion lens, very thin-walled tubing was necessary since this lens has a free working distance of less than 150 μm.

Thick-walled tubes were constructed from precision bore glass tubing obtained from Wilmad Glass Company, Buena, New Jersey, which supplies tubing with inside diameter as low as 75 μm. Lengths of about 25cm were ground at each end to fit into the 5/20 glass std. tapers mounted in each chamber. For the purpose of eliminating distortions due to the outside curved glass wall, two parallel flat surfaces were ground on opposite sides of the tubes by an optical shop. These surfaces were then joined with optical coupling grease to glass cover slips or segments from a universal rotating stage at the point along the tube where the optic axis would be located. The tube inside diameters were then calibrated by making volume flow rate versus pressure drop measurements for water.

When thin-walled capillaries were required a frame had to be built to support these very flexible tubes. Four glass slides arranged in a square or a single glass slide made up the center of the frame where viewing took place. Two glass std. taper joints were aligned and fastened to the slides with epoxy. Then glass or plastic tubing was threaded through and sealed with epoxy into both joints with enough tubing extending beyond the ends of the joints to allow sampling of blood from the center of the chambers. Several different types of thin tubing were used. Dow Chemical Company was the source of tubing made of nylon with inside diameter 100 μm and 30 μm and of that made of cellulose triacetate with 33 μm inside diameter. Thin-walled glass capillaries were made by hand drawing pipette stock. For this purpose, modifications were made on a Brinkmann pipette puller in order to extend the length over which tubing could be heated. Using the pipette apparatus as a support and heating unit only, tubes were drawn by hand to the desired diameters. Inspection under a microscope was used to check that each tube was uniform in diameter for a length of at least 50 diameters. Since tubes of almost any desired size could be made in this manner, most profiles were measured in this type of tube. Their main disadvantage is that the ability to measure pressure drop per unit length in the test section is lost since the tube is not uniform for the total distance between chambers. The pressure gage reading is useful only for an indication of steadiness of flow when hand drawn tubes are used. Diameter calibration in this case was done under a microscope with a Vickers-A. E. I. image splitting eyepiece. For calibration each tube was placed between a glass slide and a cover slip. The region surrounding the tube was filled with oil of the same index of refraction as the tube material. This procedure made the inside tube wall visible without distortions allowing measurement of the tube diameter to an accuracy of about ±.1 μm.

APPENDIX C: OPTICAL DISTORTION CALCULATIONS

Corrections for Profiles Measured Across Tube

The corrections of radial position of events within the capillary tubes were done with geometrical optics by an extension of the calculations of Bayliss(4). He assumed all rays entering the microscope objective were within a few degrees of the direction of the optic axis. Since the 100x/1.3 lens, used for this thesis work, accepts a cone of light of 60°, this assumption is not reasonable and the method of Bayliss was extended to include light rays at large angles to the optic axis. Bayliss' calculation resulted in the location of object points on the tube diametral plane for image points along the same plane at a different radius. The extension of the calculation to larger angles produces object points off the diametral plane, along the curved line shown in Figure 21, for image points on the diametral plane.

The sample calculations given here are for a thin-walled tube with immersion oil of a different index of refraction than the tube material. Calculations for thick-walled tubes with flat outer surfaces are a simplification of these calculations obtained by allowing the outer tube radius to go to infinity in the equations presented. The definitions of angles and distances used are given in Figure C-1. The known quantities are the following:

R = inside radius of tube

R_o = outside radius of tube

μ_o = index of refraction of the immersion oil

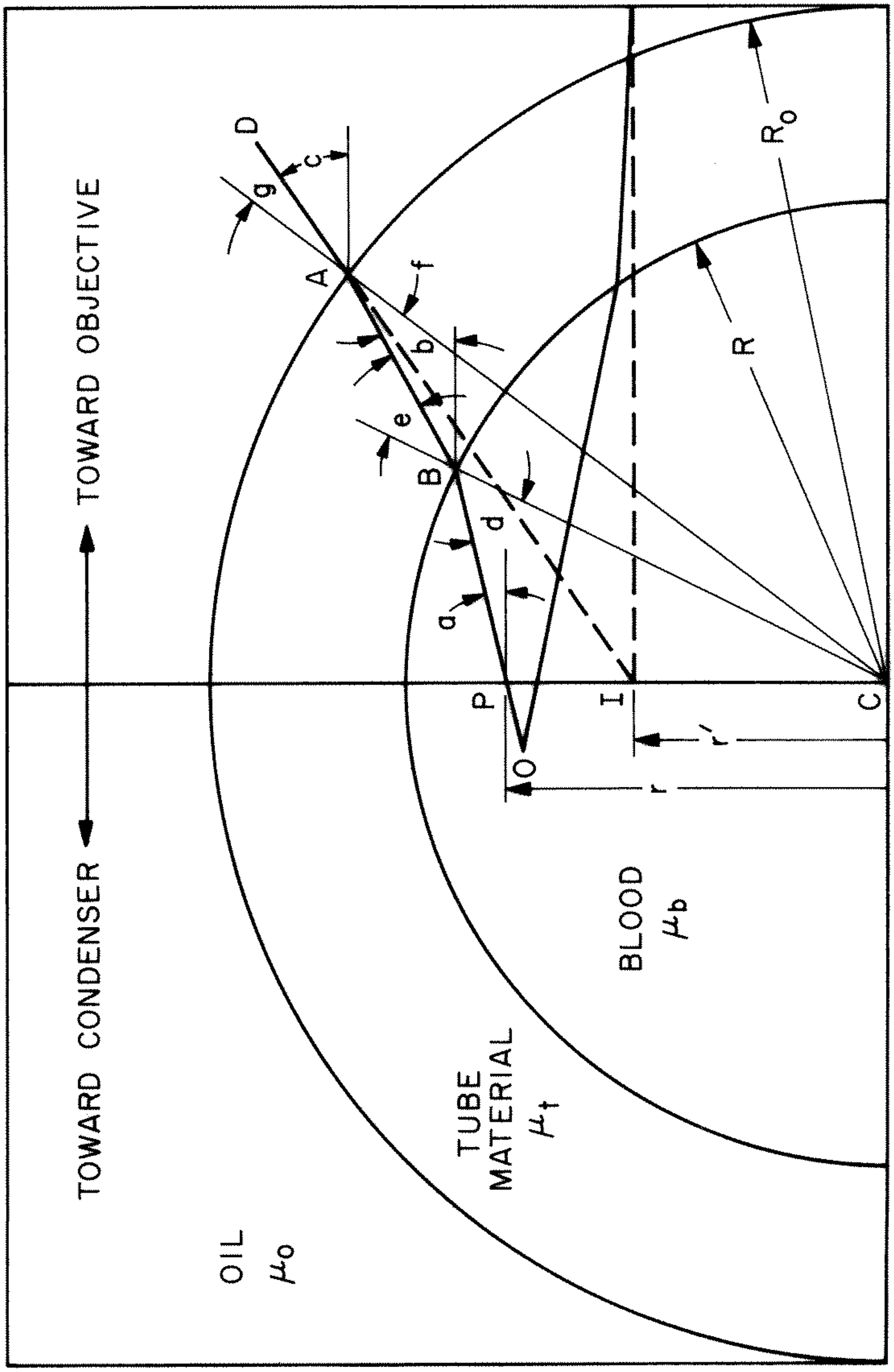
TOWARD CONDENSER
TOWARD OBJECTIVE
OIL
μ_o
TUBE MATERIAL
μ_t
BLOOD
μ_b
D
c
g
A
f
b
e
B
d
a
P
I
C
O
r
r'
R
R_o

Figure C-1

μ_t = index of refraction of the tube material

μ_b = index of refraction of the blood or plasma.

For a light ray DABO passing through the tube diametral plane at point P, a distance r from the tube axis C, the apparent path is DAI intersecting the diametral plane at a distance r' from C. The angle of incidence of the actual ray at the inner boundary of the tube wall is d and the angle of refraction e. At the outer boundary of the tube, the angle of incidence is f and the angle of refraction g. The angle of inclination of actual ray to the optic axis is a within the blood, b within the tube wall, and c within the immersion oil.

The object point 0 was located by choosing two angles c for rays appearing to pass through I. For a given radius r' and each angle c, a value of r and angle a were calculated. Each r and a combination defined an actual ray within the tube lumen. These rays were then plotted; their intersection located the object point 0. The distance of each object point from the tube axis was measured and used as the radius at which velocities, measured at the corresponding image point, were plotted for the velocity profiles. In order to calculate distance r and angle a for each r' and chosen angle c the following equations were used. From the triangle AIC,

$$R_o \sin g = r' \cos c. \tag{C-1}$$

For refraction at the interface between the tube wall and the immersion oil,

$$\mu_t \sin f = \mu_o \sin g. \tag{C-2}$$

From triangle ABC,

$$R \sin e = R_o \sin f. \qquad (C-3)$$

For refraction at the interface between the tube wall and blood,

$$\mu_b \sin d = \mu_t \sin e. \qquad (C-4)$$

From the triangel CBP,

$$r \cos a = R \sin d. \qquad (C-5)$$

From summation of angles at each interface,

$$e + b = d + a$$

$$g + c = f + b$$

therefore,

$$a = e + g + c - d - f. \qquad (C-6)$$

Corrections for Profiles Measured Through Tube

A similar calculation was done for location of object points when velocities were measured along the optic axis at different positions of focus. The only difference between the equations for this calculation and those just presented for profiles across the tube is that the intersection of rays with the optic axis instead of the diametral plane are considered. The distance from the tube axis to the object point along the optic axis is x and to the image point is x′. Equations C-2, C-3, C-4 and C-6 are unchanged for these calculations. Equations C-1 and C-5 are replaced by the following:

$$x' \sin c = R_o \sin g \qquad (C-7)$$

$$x \sin a = R \sin d. \qquad (C-8)$$

With these equations the true location x can be calculated for any velocity measured at distance x′ from the tube axis.

APPENDIX D: PARTICLE MIGRATION IN BLOOD

Speculations on the distribution of hematocrit for blood in tube flow have been made from the observations that particles in dilute suspensions tend to migrate to a particular preferred location depending on their flexibility, shape, and particle Reynolds number.

Segré and Silberberg(50) measured what they called the "tubular pinch effect" for dilute suspensions of rigid spheres. This effect is the concentration of particles at a radial position, $r \approx .6R$, with a particle depleted area at the tube center and near the wall. Goldsmith and Mason(32, 33, 35) worked with dilute suspensions of both rigid and deformable particles and found that the deformable particles always moved to the tube center. For rigid spheres, no migration was observed for particle Reynolds numbers below 10^{-3} but the tubular pinch effect was confirmed at higher Reynolds numbers. At higher concentrations, the only migrational effects observed were the movement of rigid spheres away from the wall. (Karnis, Goldsmith and Mason(38)).

Rubinow(49) suggested that these effects would have an important bearing on the behavior of blood, and Silberberg(51) proposed that the tubular pinch effect could develop in blood flow. However, Goldsmith and Mason(34) reviewed the observations of particle migration and the theoretical results concerning the origin of forces causing migration and concluded that the tubular pinch effect could not occur in blood. They felt the only migration possible would be toward the tube axis.

Considering the high concentration of particles and observations on flowing blood, it is difficult to believe that the migrational effects are very important for blood. The flow field that must exist around a particle in order for the sideward force to develop certainly must be disturbed by the crowding of other particles. For tubes small enough for a non-uniform hematocrit to be indicated by relative hematocrit measurements, the interaction between the tube wall and the red cells or simply mechanical exclusion of cells would be expected to override any migrational effects.

BIBLIOGRAPHY

1. Barbee, J. H., "The Flow of Human Blood Through Capillary Tubes with Inside Diameter between 8.7 and 221 Microns", Ph.D. Thesis, California Institute of Technology, Pasadena, California (1971).

2. Barbee, J. H. and G. R. Cokelet, "The Fåhraeus Effect", Microvascular Res., 3, 6-16 (1971).

3. Barbee, J. H. and G. R. Cokelet, "Prediction of Blood Flow in Tubes with Diameters as Small as 29μ", Microvascular Res., 3, 17-21 (1971).

4. Bayliss, L. E., "The Flow of Suspensions of Red Blood Cells in Capillary Tubes. Changes in the 'Cell-Free' Marginal Sheath with Changes in Shearing Stress", J. Physiol., 179, 1-25, Great Britain (1965).

5. Benis, A. M., "The Flow of Human Blood Through Models of the Microcirculation", Sc. D. Thesis, Massachusetts Institute of Technology, Cambridge, Massachusetts (1964).

6. Benis, A. M., E. W. Merrill et al., "The Flow of Human Blood Through Hollow Fibers", J. Appl. Physiol., 20 (1965).

7. Bennett, L., "Red Cell Slip at a Wall in Vitro", Science, 155, 1554 (1967).

8. Bishop, C., The Red Blood Cell, Academic Press, New York (1965).

9. Bränemark, P.-I. and I. Jonsson, "Determination of the Velocity of Corpuscles in Blood Capillaries. A Flying Spot Device", Biorheology, 1, 143 (1963).

10. Bugliarello, G. and J. W. Hayden, "Detailed Characteristics of the Flow of Blood in Vitro", Trans. Soc. Rheology, 7, 209-230 (1963).

11. Bugliarello, G., C. Kapur and G. Hsiao, "The Profile Viscosity and other Characteristics of Blood Flow in a Non-uniform Shear Field", Part 4 of the Proc. of the 4th Inter. Con. on Rheology, A. L. Copley, ed., 351-369 (1963).

12. Bugliarello, G., "Some Aspects of the Biomechanics of the Microcirculation Anno 1969", Developments in Mechanics, 5, Proceedings of the 11th Midwestern Conference (1969).

13. Bugliarello, G. and J. Sevilla, "Velocity Distribution and Other Characteristics of Steady and Pulsatile Blood Flow in Fine Glass Tubes", Biorheology, 7, 85-107, Pergamon Press, Great Britain (1970).

14. Casson, N., "A Flow Equation for Pigment-Oil Suspensions of the Printing Ink Type", Rheology of Disperse Systems, ed. C. C. Mill, 84-104, Pergamon Press, New York (1959).

15. Chien, S., "Blood Rheology and Its Relation to Flow Resistance and Transcapillary Exchange with Special Reference to Shock", Adv. Microcirc., 2, 89-103 (1969).

16. Cokelet, G. R., "The Rheology of Human Blood", Sc.D. Thesis, M. I. T., Cambridge, Massachusetts (1963).

17. Cokelet, G. R., "Comments on the Fåhraeus-Lindqvist Effect", Biorheology, 4, 123 (1967).

18. Cokelet, G. R., E. W. Merrill, et al., "The Rheology of Human Blood--Measurements Near and at Zero Shear Rate", Trans. Soc. Rheol., 7, 303 (1963).

19. Cokelet, G. R. and H. Meiselman, "Rheological Comparison of Hemoglobin Solutions and Erythrocyte Suspensions", Science, 162, 275 (1968).

20. Cokelet, G. R., "The Rheology of Human Blood", Biomechanics--Its Foundations and Objectives, ed., Y. C. Fung, et al., Prentice-Hall, Englewood Cliffs, New Jersey (1972).

21. Fåhraeus, R., "The Suspension Stability of Blood", Physiol. Rev., 9, 241-274 (1929).

22. Fåhraeus, R. and T. Lindqvist, "The Viscosity of Blood in Narrow Capillary Tubes:, Am. J. Physiol., 96, 562 (1931).

23. Fitz-Gerald, J. M., "Mechanics of Red Cell Motion in Very Narrow Capillaries", Proc. Roy. Soc. London, Series B, 174, 193 (1969).

24. Fitz-Gerald, J. M., "Implications of a Theory of Erythrocyte Motion in Narrow Capillaries", J. Applied Physiol., 27, 912 (1969).

25. Frasher, W., H. Wayland and J. H. Meiselman, "Viscometry of Circulating Blood in Dog. I: Heparin Injection; II: Platelet Removal", J. Appl. Physiol., 25, 751-760 (1968).

26. Frasher, W. G. and H. Wayland, "A Repeating Modular Organization of the Microcirculation of Cat Mesentery", Microvascular Res., 4, (1972).

27. Gaehtgens, P., H. J. Meiselman and H. Wayland, "Evaluation of Photometric Double-Slit Velocity Measuring Method in Tubes 25μ to 130μ in Bore", 5th Europ. Conf. Microcirculation, Gothenburg 1968, Bibl. Anat., No. 10, 571-578 Karger, Basel/N. Y. (1969).

28. Gaehtgens, P., H. Wayland and H. J. Meiselman, "Velocity Profile Measurements in Living Microvessels by a Correlation Method", Proc. of 2nd Intern. Conf. Intern. Soc. of Hemorheology, 1969, Theoretical and Clinical Hemorheology, ed. by H. H. Hartert and A. L. Copley, Springer-Verlag Berlin-Heidelberg-N. Y. (1971).

29. Gaehtgens, P., H. J. Meiselman and H. Wayland, "Velocity Profiles of Human Blood at Normal and Reduced Hematocrit in Glass Tubes up to 130μ Diameter", Microvascular Res., 2, 13-23 (1970).

30. Gaehtgens, P., H. J. Meiselman and H. Wayland, "Erythrocyte Flow Velocities in Mesenteric Microvessels of the Cat", Microvascular Res., 2, 151-162 (1970).

31. Gaehtgens, P., "Pulsatile Pressure and Flow in the Mesenteric Vascular Bed of the Cat", Pflügers Arch., 316, 140-151 (1970).

32. Goldsmith, H. L. and S. G. Mason, "Some Model Experiments in Haemodynamics", 2nd Europ. Conf. Microcirculation, Pavia 1962. Bibl. anat., 4, 462-478, Karger, Basel/N. Y. (1964).

33. Goldsmith, H. L. and S. G. Mason, "Some Model Experiments in Haemodynamics II", 3rd Europ. Conf. Microcirculation, Jerusalem 1964., Bibl. anat., 7, 353-362, Karger, Basel/N. Y. (1965).

34. Goldsmith, H. L. and S. G. Mason, "Further Comments on the Radial Migration of Spheres in Poiseuille Flow", Biorheology, 3, 33-40 (1965).

35. Goldsmith, H. L. and S. G. Mason, "The Microrheology of Dispersions", Rheology, Vol. 4, ed. by F. R. Eirich, Academic Press, New York (1967).

36. Goldsmith, H. L., "The Microrheology of Red Blood Cell Suspensions", J. of Gen. Physiol., 52, 5s-28s (1968).

37. Intaglietta, M., W. R. Tompkins and D. R. Richardson, "Velocity Measurements in the Microvasculature of the Cat Omentum by On-Line Method", Microvascular Res., 2, 462-473 (1970).

38. Karnis, A., H. L. Goldsmith and S. G. Mason, Can. J. of Chem. Eng., 44, 190 (1966).

39. Kreid, D. K. and R. J. Goldstein, "Measurement of Velocity Profiles in Simulated Blood by the Laser-Doppler Technique", presented at the Symposium on Flow-Its Measurement and Control in Science and Industry, Pittsburgh (1971).

40. Meiselman, H. J., "Some Physical and Rheological Properties of Human Blood", Sc.D. Thesis, Chem. Eng., M.I.T., Cambridge, Massachusetts (1965).

41. Meiselman, H. J. and G. R. Cokelet, "Blood Rheology Instrumentation and Techniques", presented at the First Symposium on Flow-Its Measurement and Control in Science and Industry, Pittsburgh, Pennsylvania (1971).

42. Merrill, E. W., "Rheology of Blood", Physiol. Rev., 49, 863-888 (1969).

43. Palmer, A. A., "Some Aspects of Plasma Skimming", Hemorheology, Proc. of 1st Intern. Conf., ed. by A. L. Copley, Pergamon Press (1966).

44. Monro, P. A. G., "Methods for Measuring the Velocity of Moving Particles under the Microscope", Advances in Optical and Electron Microscopy, Vol. 1, ed. by R. Barer and V. E. Cosslet, 1-40, Academic Press, New York (1966).

45. Monro, P. A. G., "Visual Streak Image Technic for Measuring Erythrocyte Velocity", Methods in Medical Research, Vol. 2, ed. by R. F. Rushmer Yearbook Medical Publishers, Chicago (1966).

46. Rabinowitsch, B., Z. physik. Chemie, A145, 1-26 (1929).

47. Repetti, R. V. and E. F. Leonard, Nature, 203, 1366 (1964).

48. Rubinow, S. I. and J. B. Keller, "Transverse Force on a Spinning Sphere Moving in a Viscous Fluid", J. Fluid Mech., 11, 477 (1961).

49. Rubinow, S. I., "Comments on the Radial Migration of Spheres in Poiseuille Flow", Biorheology, 2, 117-118 (1964).

50. Segré, G. and Silberberg, A., "The Tubular Pinch Effect in the Poiseuille Flow of a Suspension of Spheres", 2nd Europ. Conf. Microcirculation, Pavia 1962. Bibl. anat., 4, 83-93, Karger, Basel/New York (1964).

51. Silberberg, A., "The Tubular Pinch Effect in the Circulation of Blood", Biorheology, 4, 29-30 (1966).

52. Wayland, H. and P. C. Johnson, "Erythrocyte Velocity Measurement in Microvessels by a Correlation Method", 4th European Conference on Microcirculation, Cambridge, ed. by H. Harders, S. Karger-Basel/New York (1966).

53. Wayland, H. and P. C. Johnson, "Erythrocyte Velocity Measurement in Microvessels by a Two-Slit Photometric Method", J. of Appl. Physiol., 22, No. 2, February (1967).

54. Wayland, H., "Rheology and the Microcirculation", Gastroenterology, 52, 342 (1967).

55. Wayland, H., "Photosensor Methods of Flow Measurement in the Microcirculation", presented at meeting of the Amer. Heart Assn. Tucson (1971) to be published in Microvascular Res.

56. Whitmore, R. L., "A Theory of Blood Flow in Small Vessels", J. of Appl. Physiol., 22, No. 4, (1967).

57. Whitmore, R. L., Rheology of the Circulation, Pergamon Press, Oxford (1968).

58. Wiederhielm, C. A., "Photospectrum Analysis Technique", Methods in Medical Research, Vol. II, ed. by R. F. Rushmer, 212-216, Yearbook Med. Pub., Chicago (1966).